A search for supersymmetry with the ATLAS detector using kinematic shape constraints in events containing one electron or muon

Daniel R. Short

Merton College, Oxford

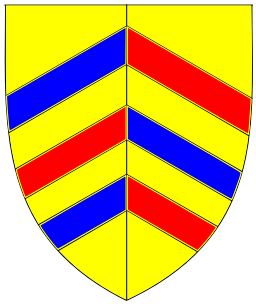

Thesis submitted in partial fulfilment
of the requirements for the degree of
Doctor of Philosophy

Trinity Term, 2012

A search for supersymmetry with the ATLAS detector using kinematic shape constraints in events containing one electron or muon

Daniel R. Short
Merton College, Oxford

Thesis submitted in partial fulfilment of the requirements
for the degree of Doctor of Philosophy

June 2012

Abstract

The ATLAS experiment is used to observe the $\sqrt{s} = 7$ TeV proton-proton collisions produced by the LHC at CERN. This gives an unprecedented opportunity to search for physics beyond the Standard Model at hitherto unexplored kinematic regimes. Supersymmetry (SUSY) provides interesting solutions to a variety of theoretical problems that may be encountered in the Standard Model at high energy scales, while providing signatures that may be observed at the LHC. However, in order to produce a search that is sensitive to SUSY it is vital to understand how the physics that has been discovered to date may produce signatures that mimic those expected from SUSY.

Statistical models are constructed using both Monte Carlo and data-driven predictions of various background processes. The expectations are compared to the observed data for selections containing one electron or muon, each in association with jets and missing transverse momentum. Kinematic variable shapes, in the form of histograms, are used to enhance the sensitivity of the search. Squark and gluino masses in a MSUGRA SUSY model are excluded up to 1200 GeV, while gluino masses up to 900 GeV are excluded in a simplified SUSY model. Model-independent limits are also set, excluding theoretical models with efficiency times cross section above 1 fb.

To my parents.

Acknowledgements

It turns out that of all the pages of thesis that I have written over the last few months one of the hardest parts is committing to a few lines that acknowledge all of the support and friendship that I have experienced over the last few years. That is most certainly not for want of subjects to include. Rather, I have met so many remarkable people throughout my life that I am sure that I will not be able to do them all justice.

For my own ease, I will start at the beginning with my parents without whose unfailing love and support this document would most definitely have never been started, let alone completed. For always providing a home to return to, and words of encouragement when I'm away, I love you both very much.

There is a wide support network of family and friends back home in Dunstable who, while I'm not going to list names, have always made it a pleasure to return home.

Next I'd like to acknowledge two very important people in my progression as a scientist, Jim Maple and Roger Seldon - who taught me throughout my time at Manshead School that science could be both exciting and fun.

I can't imagine that anyone could get through something like a DPhil without having a solid group of friends to return to from time to time. Fortunately I've been lucky enough to have such a group throughout my time at university. To Sam, Dave, Lee, Joe, Mark, Jonny, Tim and more recently Jenna and Dave (aka 'The Lads'), thank you for always giving me a group that I can visit knowing that if I try to talk about physics you'll just nod and smile and we'll move on to something else (usually geography).

Throughout my time at Oxford I have met many great people, a fact which has been enhanced by being a member of Merton College. I fear that if I list all of the people that deserve recognition in this area I am bound to forget someone, so will leave it at 'You know who you are'.

Within the Oxford Particle Physics department I managed to find many like-minded souls, who at times could offer a helping hand with technical advice and discussion and at other times could offer a beer and light hearted conversation. In particular I would like to mention Sam, Phil, Caterina, James, Ryan and my office mates Alex and Chris.

Similarly, throughout my LTA at CERN I managed to make some very good friends with whom I could ski in the winter and chill out in the parks or by the lake in the summer. Again, the full list of people that fall into this category is too extensive for this short summary but I hope that if any of you read this you know who you are.

Special thanks has to go to those that I have lived with during my DPhil. To Mike, who provided the banter throughout my first year. On my return to Oxford from Switzerland, Phil, Janet and Henry allowed me to join their group and provided a welcoming house to return to every day. In this final year, I am especially grateful to Francoise and Steven, who

have put up with various work-related moods while always providing friendly conversation.

I'd also like to thank the secretariat in Oxford - Sue, Kim, Laura and Danielle, for always keeping me organised and not complaining when I would always make the same queries when filling out the various forms that I would forget to do until the last minute.

And then I come to those who have made the content of this thesis possible. First I must thank the SCT team - particularly Tony, Dave, Per, Ingo, Bruce, Saverio and Steve, who gave valuable input throughout my service work. The bulk of this thesis covers studies performed in the one lepton supersymmetry search with ATLAS. For everyone that I worked with on both the pileup studies and the shape-based analysis, thank you! Especially I am very grateful to the team that I worked with on the shape-based analysis - David, Max, Alex, Jeanette, Moritz and Hiroshi. Being able to work in a team where everyone was willing to support each other to ensure that a good result was produced has set a very high precedent for any work that I do in the future!

To Alan, my supervisor for these past few years, thank you for letting me find my own path through this DPhil, while still giving encouragement and advice when needed. Also, thank you for the persistent reminders that this document would eventually have to be written! Your advice and helpful comments have been critical in bringing all of this together.

Finally I come to Lucy. Thank you for being a constant reminder that there are things in life that are much more important than writing a thesis.

Preface

This thesis presents work performed using data that were produced by ATLAS between 2009 and late 2011 and highlights my own personal contributions. Sources of additional information have been cited where possible, although they may not always be in the public domain.

For clarity, my work has contributed to the following areas (in reverse chronological order):

1. **Development and implementation of the use of kinematic shape constraints in the supersymmetry search with one lepton.** I worked as one of the main developers of the `HistFitter` package, which allows the required statistical model to be easily built, configured and analysed. My focus was on the configurability of the package to allow rapid generation of results and easy implementation of statistical tools.
2. **Studying the effect of additional proton-proton interactions (pileup) on the supersymmetry search with one lepton.** A large part of this work involved studying the use of the jet vertex fraction as a means by which pileup could be controlled. I also looked into different ways by which the modelling of pileup in Monte Carlo could be matched to observations in data.
3. **Monitoring the optical links of the semiconductor tracker.** I developed systems to monitor both the reception and transmission links in the semiconductor tracker. I also performed studies to investigate potential correlations between the failures in the transmission links. As well as this monitoring, I wrote a calibration test to attempt to monitor the effects of radiation on the modules installed on the detector.

This thesis will use natural units ($c = \hbar = 1$) throughout.

Contents

Part I

Preliminary information

Chapter 1

Introduction

Advances in mathematics and theoretical physics throughout the 20^{th} and early 21^{st} centuries have lead to rapid progress in our ability to understand the fundamental nature of the Universe. What is even more encouraging is that technological advances and new experimental techniques have allowed many of these theories to be put to the test. Particle physics is founded upon one of the major outcomes of this phase of advancement - a theory known as the "Standard Model" (SM) [1, 2].

Despite the great success of the SM, we know that it is incomplete. For example, it does not include gravity and so must be modified at the Planck scale[1]. However, probably the most discussed of these missing links is the fact that there is no experimental evidence for the methods by which the fundamental particles gain mass, or why the weak force is weak. The SM attempts to address both of these issues theoretically by introducing the Higgs mechanism [3–5]. This would produce an observable Higgs boson with a mass below 1 TeV, an energy scale known as the electroweak symmetry breaking (EWSB) scale[2].

Even if the Higgs boson is observed then there are still open questions within the SM, such as: Why is the Higgs boson mass around the scale of EWSB, if we have to also include new particles at the Planck scale? Can the forces of the SM be unified? What is the nature

[1] The Planck scale is equivalent to about 10^{19} GeV and is the energy at which the strength of gravitational interactions is expected to be comparable to the other known forces.

[2] Although other methods of EWSB have been postulated, such as technicolor [6].

of the cosmologically and astronomically inferred dark matter (DM) [7, 8]?

These questions can be addressed in various ways, for example by introducing extra dimensions into the theory [9, 10] or by adding extra symmetries. This thesis will focus searching for models that may address these questions via an additional symmetry, known as supersymmetry (SUSY) [11]. SUSY acts to symmetrise the matter and interactions of the Universe. This results in the spectrum of particles being doubled, as each SM particle is mirrored by a heavy SUSY partner. However, in order for SUSY to provide useful solutions to some of the issues in the SM, it too must produce new particles close to the electroweak scale.

The hunt for new particles at the electroweak scale began in the 1980s with the discovery of the W [12, 13] and Z [14, 15] bosons. Since then searches have been made for particles around the energy scale of EWSB, first by LEP and then by the Tevatron. The Tevatron managed to discover the sixth quark, the top, in 1995 [16, 17] close to the EWSB scale, but neither experiment found significant evidence of the nature by which electroweak symmetry is broken. The most recent tests of the SM are being performed at the LHC, which began observing 7 TeV proton-proton (pp) collisions in 2009 [18, 19].

Experiments observing collisions at these energy scales also allow physicists to search for SUSY. ATLAS and CMS have set limits on various realisations of SUSY [20, 21], as well as setting limits on cross sections of processes in any generic model. However, SUSY can also be searched for indirectly by measuring the rates at which rare hadron decays take place [22, 23] or by attempting to measure the cross section of the DM candidate with a detector volume [24].

1.1 Overview of this thesis

This thesis presents a search for SUSY performed using data collected by the ATLAS detector at the LHC throughout 2011. My work within this search focused on improving the statistical model that describes the theoretical predictions of both scenarios where SUSY is assumed to

exist and where no SUSY is present in nature. The improvement is produced by including information about the shape of kinematic distributions in the statistical model in the form of histograms. A large part of my contribution to this method was the development of a tool called `HistFitter` that allows the statistical model to be easily configured to suit the needs of the analysis. This also allows the necessary histograms to be produced rapidly from the ATLAS datasets and facilitates collaborative work within analysis teams via simple Python configuration files.

The SM and SUSY are discussed in more detail in Chapter 2, while ATLAS is introduced in Chapter 3. Both the observed data and Monte Carlo (MC) theoretical predictions are introduced in Chapter 4, along with selections that are applied to clean the data and produce physics objects that are suitable for analysis.

The analysis that will be presented uses events in both observed and MC datasets that contain one electron or muon, a number of jets and significant missing transverse momentum, and is summarised in Chapter 5. Kinematic selections are applied to produce datasets that are enriched in a particular process (known as control regions) or depleted in SM processes (known as signal regions). The methods for estimating the SM background contributions in the signal regions are discussed in Chapter 6. Histograms are then constructed for each of these selections and are used to build a statistical model, which is analysed by comparing theoretical predictions to the observed data as described in Chapter 7. The results of this analysis are presented as limits on two particular examples of SUSY scenarios as well as a model-independent limit on the cross section of any theoretical model in Chapter 8.

In addition to the SUSY search that takes up the bulk of this thesis, I have included two suplementary studies:

- The high luminosity of the LHC means that every selected collision will have a background of overlapping collisions that are not of interest to the analysis, known as pileup. Studies on the modelling of pileup in MC simulations in mid-2011, its effect on a particular analysis and methods by which it can be controlled are given in Chapter 9. My contribution in this area was two-fold. In the first case I performed studies to

show that the modelling of pileup in MC simulations can result in increased statistical uncertainties, and suggested that this effect may be reduced by altering the method by which the simulation is compared to data. The second contribution was a study of the effect that associating tracks with different vertices may have on differentiating between jets from pileup and those produced by the high p_{T} interaction of interest. I showed that by selecting jets in which the jet p_{T} is dominated by tracks from the high-p_{T} primary vertex, the dependence of event selections on the number of interactions in an event can be greatly reduced.

- An additional study of the performance of the optical system that is used to control the semiconductor tracker is shown in Chapter 10. A working detector is vital to the production of good results and so it is necessary to ensure that any failures in the system can be monitored. An attempt is also made to understand the nature of these failures. In this study I produced a framework that monitors the amount of light transmitted through this system. Using this I monitored the failure rate of the links that make up the optical system and searched for correlations between these failures and possible environmental factors.

Chapter 2

Theoretical motivation

2.1 The Standard Model

Great progress has been made over the last century in our understanding of the fundamental nature of the Universe. A major result of this was the SM, which provides a description of how all of the known particles and forces interact (with the exception of gravity).

The SM is a quantum field theory - constructed from a finite set of fields that permeate all space. Particles are produced when a field is excited and can propagate according to constraints set by special relativity.

If a field is anti-symmetric under the exchange of particle indices it is 'fermionic'. Excitations of a fermionic field are called fermions and have half-integer spin. A fermion field is generally referred to as having a particular handedness or chirality, which describes the projection of the field onto left-handed or right-handed states.

If, on the other hand, a field is symmetric under the exchange of particle labels it is 'bosonic'. Excitations of a bosonic field are called bosons and have integer spin.

2.1.1 Gauge interactions and symmetries

There are twelve unit spin gauge bosons in the SM, which result from the structure of the underlying $\mathrm{SU}(3)_C \otimes \mathrm{SU}(2)_L \otimes \mathrm{U}(1)_Y$ gauge symmetry. This symmetry describes how the fields are allowed to interact with each other according to the resulting conservation laws [25].

- The $\mathrm{SU}(3)_C$ symmetry corresponds to the conservation of colour charge (C) which can take three values commonly labelled as r, g and b. This symmetry corresponds to the strong force that is mediated by eight gluons (g).
- The $\mathrm{SU}(2)_L$ symmetry corresponds to the conservation of weak isospin (I_3) that groups left-handed fields into doublets. The subscript L indicates that the symmetry only acts on left handed particles. Interactions according to $\mathrm{SU}(2)_L$ are mediated by three weak bosons ($W^{\{1,2,3\}}$).
- The $\mathrm{U}(1)_Y$ symmetry corresponds to the conservation of weak hypercharge (Y). This symmetry is mediated by a single boson (B).

The bosons corresponding to the $\mathrm{SU}(2)_L$ and $\mathrm{U}(1)_Y$ symmetries are all massless. This is problematic for the SM, as the bosons that mediate the weak force are known to be massive. However, the SM solves this problem by considering that some of the physical bosons that we observe in experiments are not exactly the bosons that correspond to the gauge groups. The symmetries are said to be 'broken'.

2.1.2 Electroweak symmetry breaking

In the 1960s, Glashow, Salam and Weinberg [1, 2] showed that $\mathrm{SU}(2)_L$ and $\mathrm{U}(1)_Y$ can be grouped into a single $\mathrm{SU}(2)_L \otimes \mathrm{SU}(1)_Y$ electroweak symmetry. The electroweak symmetry is then broken, below $\mathcal{O}(100)$ GeV, into a $U(1)_e$ symmetry, which corresponds to the conservation of electric change (Q). During this symmetry breaking the W^3 and the B mix to form the familiar massive Z^0 and massless photon (γ), while the $W^{\{1,2\}}$ transform into the $W^{\pm}$ and also gain mass. Therefore, as we only observe the broken symmetry, we only observe

the massive $W^{\pm}$ and Z^0 bosons.

The EWSB in the SM is made possible by the inclusion of a complex scalar field, commonly referred to the Higgs field. The Higgs field is a doublet, and so consists of four real components[1]. Three of the components of the field, known as Goldstone bosons, become the longitudinal components of the $W^{\pm}$ and Z^0 during EWSB. This corresponds to generating masses for the $W^{\pm}$ and Z^0, while the γ is left massless. Fermion masses are also generated through Yukawa interactions with the Higgs field. The last component of the Higgs field is observable as a massive Higgs boson, although it has not yet been discovered. The search for the Higgs boson has been the focus of many experimental searches over the last two decades, the most recent of which were performed independently by ATLAS [18] and CMS [19].

2.1.3 Particle content

The twelve fermionic states of the SM are split into two types: quarks, which have colour charge; and leptons, which do not have colour charge. Furthermore, the fermions are grouped into three generations according to their mass ordering. The fermionic content of the SM can be seen in Table 2.1 for the leptons and Table 2.2 for the quarks. For each fermion there exists an anti-particle, which has the same mass as the equivalent particle but has all of its quantum numbers multiplied by negative one.

The twelve observable gauge bosons of the SM that mediate the strong, weak and electromagnetic forces after EWSB are shown in Table 2.3

2.2 Potential problems in the Standard Model

The SM is a very successful theory, directly supported by many experimental results [26]. However, there are some phenomenological arguments that may indicate that the SM does

[1] A complex scalar doublet has two complex components. As each complex component consists of a two real components, one of which is multiplied by the imaginary number $i = \sqrt{-1}$, the doublet as a whole has four real components.

Name	Symbol	Q	I_3	C	Mass
electron	e	-1	-1/2	0	511 keV
electron neutrino	ν_e	0	1/2	0	—
muon	μ	-1	-1/2	0	106 MeV
muon neutrino	ν_μ	0	1/2	0	—
tau	τ	-1	-1/2	0	1.78 GeV
tau neutrino	ν_τ	0	1/2	0	—

Table 2.1: The name, symbol, electric charge, weak isospin, colour charge and mass of the leptons [26].

Name	Symbol	Q	I_3	C	Mass
down	d	-1/3	-1/2	$\{r, g, b\}$	4.1 - 5.7 MeV
up	u	2/3	1/2	$\{r, g, b\}$	1.7 - 3.1 MeV
strange	s	-1/3	-1/2	$\{r, g, b\}$	80 - 130 MeV
charm	c	2/3	1/2	$\{r, g, b\}$	1.18 - 1.34 GeV
bottom	b	-1/3	-1/2	$\{r, g, b\}$	$4.19\ ^{+0.18}_{-0.06}$ GeV
top	t	2/3	1/2	$\{r, g, b\}$	$172.9 \pm 0.6 \pm 0.9$ GeV

Table 2.2: The name, symbol, electric charge, weak isospin, colour charge and mass of the quarks. For the lightest five quarks the mass is given in the $\overline{\text{MS}}$ scheme, while the top quark is measured directly [26].

Name	Symbol	Q	I_3	C	Mass
photon	γ	0	0	0	0
W^+	W^+	1	1	0	80.3 GeV
Z^0	Z^0	0	0	0	91.2 GeV
W^-	W^-	-1	-1	0	80.3 GeV
gluon	g	0	0	octet	0

Table 2.3: The name, symbol, electric charge, weak isospin, colour charge and mass of the gauge bosons. From top to bottom they are segmented into the relevant forces: electromagnetism; weak; and strong [26].

not describe the Universe as a whole up to large energy scales.

The hierarchy problem: The Higgs mechanism is introduced to break electroweak symmetry and generate masses in the SM. However, the mass of the Higgs boson is affected by the mass of other particles in the theory through virtual loop corrections to the square of the Higgs boson mass. These corrections are proportional to the square of the ultra-violet cutoff of the theory, which is the energy scale at which the current theory ceases to be a good description of physics. Therefore, if any new physics is introduced to the theory, for example at the Planck scale ($\mathcal{O}(10^{19})$ GeV), there is no reason that the Higgs boson mass should remain close to the scale of EWSB [27–30]. Indeed, one would expect the Higgs boson mass to be approximately the Planck mass. Furthermore, as all of the other particles in the SM gain mass through the Higgs mechanism, the entire SM particle spectrum would be pulled towards the Planck mass. This is clearly not a phenomenologically valid situation. These arguments are often used as a justification for searching for new physics at energy scales of 1 TeV, so that the ultra-violet cutoff of the SM is close to the Higgs mass, rather than the Planck scale.

Unification of couplings: The coupling strengths in the SM depend on the energy scale of the interaction [31]. This scale dependence means that the strengths of the electroweak and strong interactions become comparable at $\mathcal{O}(10^{16})$ GeV, known as the Grand Unified Theory (GUT) scale. Unification of the couplings could suggest that the SM is in fact some broken form of a more fundamental symmetry [32]. However, the SM couplings would have to be modified at some intermediate scale to precisely unify.

Matter content on the universal scale: Observations of the Universe at microwave frequencies have been used to probe the afterglow of the Big Bang [7, 33]. Analysis of this early light shows that the DM content of the Universe is approximately five times larger than that contained in baryons. This evidence for DM is supported by observations of interactions between galaxies [8] and the rotation curves of individual galaxies [34], among other sources. There are no SM particles that can account for DM, so at least one new weakly interacting, stable, massive particle would need to be introduced to

the theory.

2.3 Supersymmtery

One way by which the shortcomings of the SM can be addressed is via the introduction of a new symmetry that relates the spin of the SM particles to a new set of particles introduced by that symmetry - SUSY [11, 35–42]. The minimal addition to the SM when imposing SUSY is that each fermion and gauge field becomes a doublet, consisting of the original SM field and a new field with spin differing from the original by one half. Furthermore, the single Higgs doublet of the SM is replaced by two Higgs doublets corresponding to the Yukawa couplings for $I_3 = 1/2$ and $I_3 = -1/2$, such that five physical Higgs states (h^0,H^0,A^0,$H^{\pm}$) are generated.

The nomenclature of SUSY traditionally prepends 's' to all of the new scalar particles, while 'ino' is appended to all of the new fermions, relative to the original SM particle name. Symbolically a SUSY partner is annotated with a tilde, ˜. The pairing of these new particles with those of the SM can be seen in Table 2.4 for the SM fermions and Higgs sector and Table 2.5 for the SM gauge bosons.

Scalar bosons		**Fermions**	
squarks	$(\tilde{u}_L, \tilde{d}_L), \tilde{u}_R, \tilde{d}_R$	quarks	$(u_L, d_L), u_R, d_R$
sleptons	$(\tilde{\nu}_e, \tilde{e}_L), \tilde{e}_R$	leptons	$(\nu_e, e_L), e_R$
Higgs bosons	$(H_u^+, H_u^0), (H_d^0, H_d^-)$	higgsinos	$(\tilde{H}_u^+, \tilde{H}_u^0), (\tilde{H}_d^0, \tilde{H}_d^-)$

Table 2.4: The SM fermions and their SUSY partners, along with the Higgs sector in the MSSM. Only the first generation of SM fermions are shown, for simplicity. Chiral notation is used and the $SU(2)_L$ grouping is given.

Fermions		**Gauge bosons**	
gluinos	$\tilde{g} \times 8$	gluons	$g \times 8$
winos	$\tilde{W^{\pm}}, \tilde{W}^0$	W bosons	$W^{\pm}, W^0$
bino	$\tilde{B}^0$	B boson	B^0

Table 2.5: The SM gauge bosons and SUSY partners in the MSSM.

2.3.1 Supersymmetry breaking

If SUSY exists at all energy scales then new particles would be produced with masses equal to those of the SM particles. Since no fundamental scalar particles have been observed with masses corresponding to the SM fermions, SUSY must be broken. This symmetry breaking is performed at a very high, experimentally inaccessible energy scale and then propagated down to the experimental scale via mediating particles. The most frequently studied forms of SUSY breaking are gravity, gauge or anomaly mediated. In general, a large number of additional free parameters are added to the theoretical model by SUSY breaking, although these can be reduced by imposing particular assumptions and approximations.

The minimal way in which the SM can be extended to include broken SUSY is known as the 'Minimally Supersymmetric Standard Model' (MSSM) [43–47].

SUSY breaking also causes the different states to mix. The four neutral fermions in the MSSM ($\tilde{W}^0$,$\tilde{B}^0$,$\tilde{H}_u^0$,$\tilde{H}_d^0$) mix to produce four observable neutralinos, $\tilde{\chi}^0_{\{1,2,3,4\}}$, while the four charged fermions ($\tilde{W}^{\pm}$,$\tilde{H}_u^+$,$\tilde{H}_d^-$) mix to produce four observable charginos, $\tilde{\chi}^+_{\{1,2\}}$ and $\tilde{\chi}^-_{\{1,2\}}$. It is also possible for the different scalar states corresponding to SM chiral fermions to mix such that $\tilde{t}_L$ and $\tilde{t}_R$ produce the observable $\tilde{t}_1$ and $\tilde{t}_2$ states, for example. The precise values of the mixing angles depend on the nature of SUSY breaking.

2.3.2 Supersymmetric solutions to Standard Model shortcomings

Having introduced some of the basic concepts of SUSY, let us look at how this extension of the SM may be used to address the potential phenomenological issues posed in Section 2.2.

Stabilisation of the Higgs boson mass: The additional SUSY scalar particles provide additional terms in the corrections to the Higgs boson mass. In fact, the SUSY scalar terms act to cancel the SM fermion terms making it possible to introduce new heavy particles without pulling the Higgs boson mass away from the EWSB scale [47–52]. There is, however, a residual contribution to the Higgs boson mass from the SUSY

breaking terms, which indicates that the mass scale of the lightest SUSY particles should be close to the EWSB scale.

High energy convergence of couplings: The energy dependencies of the couplings result from virtual interactions that screen the bare particle charges. Therefore, SUSY will affect the level of screening, and so the energy dependence of the couplings, by adding more possible interactions. Depending on the specific nature of SUSY, this can cause the coupling strengths to unify at high energy scales [53–56].

***R*-parity and the lightest SUSY particle:** Pure SUSY can allow interactions that may result in rapid proton decay, for example via the transformation of an up and down quark pair into a quark plus a lepton, mediated by a squark. To prevent such scenarios, many SUSY models introduce R-parity (P_R) to maintain a stable proton. R-parity is defined as

$$P_R = (-1)^{3(B-L)+2s}, \tag{2.1}$$

where B is the baryon number, L is the lepton number and s is the spin of a given particle. This definition means that all SM particles have $P_R = +1$ and SUSY particles have $P_R = -1$. P_R is a multiplicatively conserved quantum number, such that if a particle decays to produce two new particles, the product of P_R for the two new particles must be equal to the P_R of the original particle. Therefore, the SUSY particles are produced in pairs which then decay via cascades with one SM particle and one SUSY particle leaving each vertex, if R-parity is conserved. Such cascades terminate with a lightest SUSY particle (LSP). As the LSP is stable it may be a valid candidate to contribute to DM, if it is electrically neutral and colourless [57, 58].

Therefore, if the SM is extended by adding SUSY, it is possible to provide solutions to some of the issues that the SM may encounter when considering high energy scales or matter distributions over large distance scales. In order to sufficiently protect the Higgs boson mass from the effects of adding new heavy particles, at least some SUSY particles should be close to the scale of EWSB ($\mathcal{O}(1)$ TeV). Furthermore, if R-parity is included then

a dark matter candidate is produced, along with distinctive signatures of many particles plus missing energy, resulting from the LSP-terminated cascades. These arguments make SUSY a favourable new physics scenario that can be searched for by analysing TeV scale collisions.

2.4 Physics at proton-proton colliders

The previous sections have addressed the theoretical basis of the SM and the resulting motivation for extending this theory using SUSY. In addition to these points it is useful to motivate the methods used to calculate the properties of physics processes at the LHC. The pp interactions at the LHC are governed by quantum chromodynamics (QCD) [59, 60], which describes how quarks and gluons scatter off of eachother. Many of the distinguishing properties of QCD result from the fact that the QCD coupling strength, α_S, is very strong at low energies and becomes weak at high energies. Therefore, QCD calculations must be aware of two regimes, the first being at high energies where perturbative techniques can be used, and the second being at low energies where perturbation theory breaks down. In the non-perturbative regime partons are said to be 'confined' in such a way as to produce colour-neutral hadronic states, known as mesons (with a quark and an anti-quark of the same colour) and baryons (with three quarks, each with a unique colour).

Partons share momentum with eachother in a confined state. This means that the partons that scatter at the LHC do so with unknown momenta on an event-by-event basis. Furthermore, individual quarks can radiate a gluon and gluons can split into quark/anti-quark pairs. These complicated processes are encompassed by parton distribution functions (PDFs), $f_i(x, Q^2)$, where i labels the type of parton, x gives the fraction of the proton's momentum that is carried by the individual parton, and Q represents the energy scale of the pp scattering process and is known as the factorisation scale. The PDFs are calculated by fitting to global experimental data [61–63]. For pp interactions close to the Z mass, the factorisation scale is $Q^2 \sim 10^4$ GeV and so resonant Z production where the two partons have similar momenta corresponds to $x \sim 0.01$. Under these conditions, the interactions at

the LHC are dominated by gluons.

As well as considering the sharing of momenta between the individual partons, the matrix element for the process of interest must be calculated. This must be calculated considering the momenta of the two interacting partons and the renormalisation scale, μ, which gives the high energy cutoff of the theory in order to make the resulting cross section finite. Due to the large coupling strength of strong interactions, it is possible that multiple partons can be produced in the final state, which means that an important distinction between the inclusive and exclusive cross sections is required. The parton-level cross section, $\sigma_{1+2\to X}(x_1, x_2, \mu)$, is then proportional to the square of the relevant matrix element.

Putting all of this together gives a calculable cross section according to:

$$\sigma_{p_2+p_2\to X} = \sum_{\text{partons}_1} \sum_{\text{partons}_2} \int \mathrm{d}x_1 \mathrm{d}x_2 f_1(x_1, Q) f_2(x_2, Q) \sigma_{1+2\to X}(x_1, x_2, \mu). \tag{2.2}$$

It should be noted that the parton-level cross sections include information about the phase space available for the final state. This covers the different ranges of momenta or angular states available for the final state. Therefore, if the interaction corresponds to the decay of a high mass state into low mass states, for example, then there will be a large amount of momentum available for the final state particles. In this case, the particles will be produced at high p_{T}. As most physics searches look for high mass particles, the corresponding experimental selections tend to require high p_{T} final states.

Chapter 3

The ATLAS detector at the Large Hadron Collider

3.1 The Large Hadron Collider

The LHC [64] is a superconducting pp and lead-lead synchrotron located at CERN. It sits in the old Large Electron-Positron collider (LEP) [65] tunnel, with a radius of 27 km. The LHC was designed to run with a beam energy of 7 TeV. However, an incident soon after the machine began operations in September 2008 [66], destroyed a section of magnets. Following the replacement of those magnets, and the installation of additional safety measures, the beam energy was reduced to 3.5 TeV when the LHC was turned back on in November 2009. The data used in this thesis were collected during 2011 with a centre of mass energy of $\sqrt{s} = 7$ TeV.

The LHC collisions are observed by seven different detectors: ALICE [67]; ATLAS [68]; CMS [69]; LHCb [70]; LHCf [71]; MoEDAL [72]; and TOTEM [73]. The information contained in this thesis covers observations of pp collisions by the ATLAS detector.

A series of linacs and synchrotrons are used to accelerate the beams to the required energies, as shown in Figure 3.1. Protons are produced by stripping hydrogen atoms in a

high electric field gradient and are injected into Linac2, which accelerates the single beam to 50 MeV. The beam is then passed to the Booster and accelerated to 1.4 GeV. The next stage in the acceleration chain is the Proton Synchrotron (PS), in which the beam energy is increased to 26 GeV. Final pre-injection acceleration is provided by the Super Proton Synchrotron (SPS), in which the beam energy reaches 450 GeV. At injection to the LHC, the beam is separated down two transfer lines, producing counter-circulating beams. The LHC then accelerates the beams to the desired beam energy of 3.5 TeV before starting collisions.

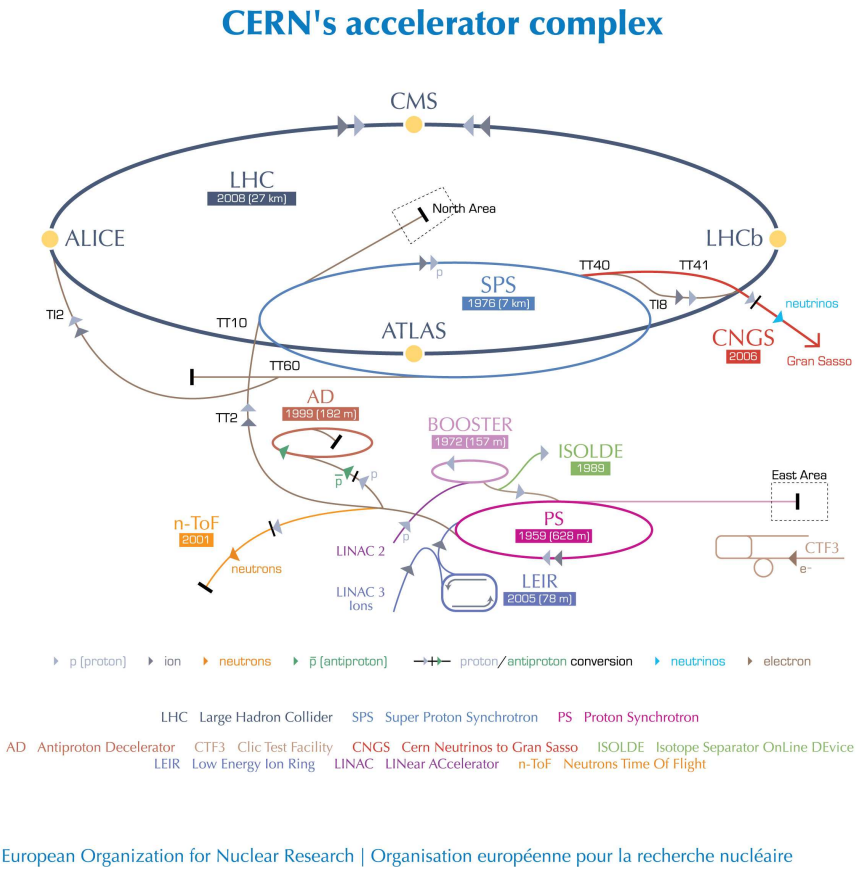

Figure 3.1: A computer generated schematic of the CERN accelerator complex layout. Taken from [74].

Many measurements that are performed by the detectors on the LHC require sensitivity to rare physics processes. In order to facilitate this, the LHC runs at very high luminosities. The necessity for these high luminosity conditions can be seen by considering the rate of events (N_i) expected for some process (i) with a particular cross section (σ_i) in a collider with a given luminosity ($\mathcal{L}$):

$$N_i = \mathcal{L}\sigma_i. \tag{3.1}$$

The value of σ_i is fixed by nature, so the luminosity must be high to generate an appreciable number of events for a particular rare process.

The luminosity in Equation 3.1 is also known as the instantaneous luminosity, with units $\mathrm{cm}^{-2}\mathrm{s}^{-1}$. In describing a dataset collected over time the integrated luminosity, $\int \mathcal{L}\mathrm{d}t$, is often used. The time integral of Equation 3.1 gives the total expected number of events for process i in the dataset of interest. The cross section is often expressed in units of 'barns' (b), where 1 b = 10^{-24} cm^2, and the integrated luminosity may be expressed in units of inverse barns.

The CERN Control Centre sets the conditions of the LHC and the luminosity is measured independently by ATLAS as described in Section 9.2. The peak luminosity used in this thesis is approximately 3×10^{33} $\mathrm{cm}^{-2}\mathrm{s}^{-1}$. This luminosity is high enough for many high cross section processes to occur per bunch crossing (BC), and these additional interactions can affect analyses as described in Chapter 9.

3.2 Overview of ATLAS

The ATLAS detector is a general purpose physics detector with close-to 4π coverage. It consists of multiple systems: the inner detector (ID); the calorimeter; the muon spectrometer (MS); the magnets; and the trigger and data acquisition (TDAQ), each of which consists of various sub-systems and will be covered in the following Sections. A graphic representation of the detector is given in Figure 3.2 and the detector is described in detail in [68].

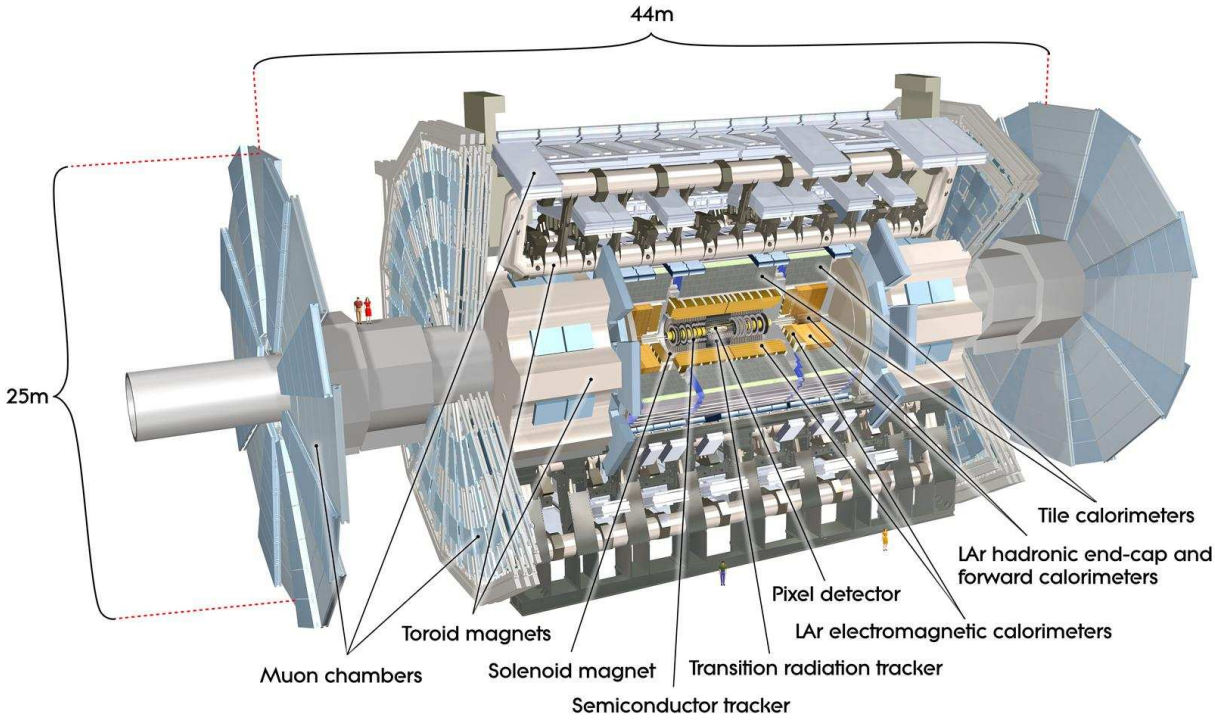

Figure 3.2: A computer generated schematic view of the ATLAS detector. Taken from [68].

3.3 Spatial and kinematic coordinate systems

ATLAS uses its own coordinate system, which will be referred to throughout this thesis. The x-axis is defined as pointing towards the centre of the LHC ring, the y-axis points vertically upwards from the centre of the Earth and the z-axis points along the beam axis, such that the system is orthogonal and right-handed. Sides A and C of the detector are defined as being positive and negative in z, respectively.

The azimuthal angle, $-\pi < \phi < \pi$, is the angle from the positive side of the x-axis in the x-y plane, while the polar angle, $0 < \theta < \pi$, is the angle from the positive side of the z-axis. A common coordinate that is used in particle physics is the pseudorapidity, η, which measures the coordinate with respect to the z-axis. The pseudorapidity is defined as

$$\eta = -\ln\left[\tan\left(\frac{\theta}{2}\right)\right] = \frac{1}{2}\ln\left(\frac{|\vec{p}| + p_{\mathrm{L}}}{|\vec{p}| - p_{\mathrm{L}}}\right), \tag{3.2}$$

where $\vec{p}$ is the particle's three-momentum and p_{L} is the z-component. Locations of detector components are generally expressed in terms of η because many models of hadronic production result in uniform particle production across values of η. The separation between particles in this coordinate system is generally referred to by the quantity $\Delta R = \sqrt{\Delta\eta^2 + \Delta\phi^2}$. This should not be confused with the value R, which is the linear distance from the z-axis.

At a hadron collider, like the LHC, it is not possible to know z-component of the momentum of the centre of mass frame. This is because the constituent partons[1] within a hadron share momentum according to parton distribution functions (see for example [62]). Therefore, it is common to use the transverse coordinate system, which is defined in the x-y plane such that the known kinematic properties of a particle are represented by a three-vector,

$$\mathbf{p}_{\mathrm{T}} = (E_{\mathrm{T}}, p_x, p_y) = (E_{\mathrm{T}}, \vec{p}_{\mathrm{T}}) = (E_{\mathrm{T}}, |\vec{p}_{\mathrm{T}}| \cos(\phi), |\vec{p}_{\mathrm{T}}| \sin(\phi)), \tag{3.3}$$

where p_x and p_y are the particle's momenta along the x-axis and y-axis respectively, the magnitude of the transverse momentum two-vector is $|\vec{p}_{\mathrm{T}}| = \sqrt{|p_x|^2 + |p_y|^2}$, and E_{T} is the transverse energy. This transverse momentum three-vector is defined with a mass, corresponding to the transformation of the invariant mass[2] into the x-y plane, known as the transverse mass,

$$m_{\mathrm{T}} = |\mathbf{p}_{\mathrm{T}}| = \sqrt{E_{\mathrm{T}}^2 - |\vec{p}_{\mathrm{T}}|^2}. \tag{3.4}$$

The beams collide in ATLAS with a small crossing angle, and as such the proton constituents interact with negligible $\vec{p}_{\mathrm{T}}$. However, the detector has finite resolution and some particles can pass through the detector unobserved, either because they do not fall within the fiducial volume or because their cross section with the detector material is very small. Therefore, by finding the total vector sum of visible momentum in the detector it is possible to define the momentum imbalance, known as the missing transverse momentum, as

[1] Parton is a term used to refer to a particle that forms a constituent part of a hadron - either a quark or a gluon.

[2] The invariant mass is defined as $m = \sqrt{E^2 - |\vec{p}|^2}$.

$$\mathbf{p}_{\mathrm{T}}^{\mathrm{miss}} = \left(E_{\mathrm{T}}^{\mathrm{miss}}, -\sum_i p_x^i, -\sum_i p_y^i \right) = \left(E_{\mathrm{T}}^{\mathrm{miss}}, |\vec{p}_{\mathrm{T}}^{\mathrm{miss}}| \cos\left(\phi^{\mathrm{miss}}\right), |\vec{p}_{\mathrm{T}}^{\mathrm{miss}}| \sin\left(\phi^{\mathrm{miss}}\right) \right), \quad (3.5)$$

where $E_{\mathrm{T}}^{\mathrm{miss}}$ is the missing transverse energy and i is the index corresponding to a given particle signature. It is common to make the assumption that the hypothesised missing particle that produces this imbalance is in the massless limit so that $E_{\mathrm{T}}^{\mathrm{miss}} = |\vec{p}_{\mathrm{T}}^{\mathrm{miss}}|$. In this case, the missing transverse momentum is fully defined by $E_{\mathrm{T}}^{\mathrm{miss}}$ and ϕ^{miss}. The massless assumption for $E_{\mathrm{T}}^{\mathrm{miss}}$ calculations will be assumed throughout this thesis.

3.4 Detector hardware

The various technologies used by ATLAS are covered in detail in [68]. A general overview of the different sub-detectors is given in this Section. First the ID and solenoid magnet, which provide tracking information, are discussed in Section 3.4.1. Next the calorimeters, which are used for energy measurement, are described in Section 3.4.2. Finally the MS and toroid magnet, which are used to measure muon tracks, are covered in Section 3.4.3.

3.4.1 Inner detector tracking

The ID tracking system consists of three devices: the Pixel tracker; the Semiconductor Tracker (SCT); and the Transition Radiation Tracker (TRT). These sit at the heart of the ATLAS detector, with an acceptance over the range $|\eta| \leq 2.5$. Specific details relating to the ID are given in [68], while further details relating to the design are given in [75, 76]. A graphical representation of the ID is shown in Figure 3.3.

The closest layer of ATLAS to the beam-pipe is the Pixel detector [77], which is built from radiation hard silicon pixels. The detector consists of three barrel layers and six end-cap discs. In this configuration a cleanly measured track would be expected to cross a total of

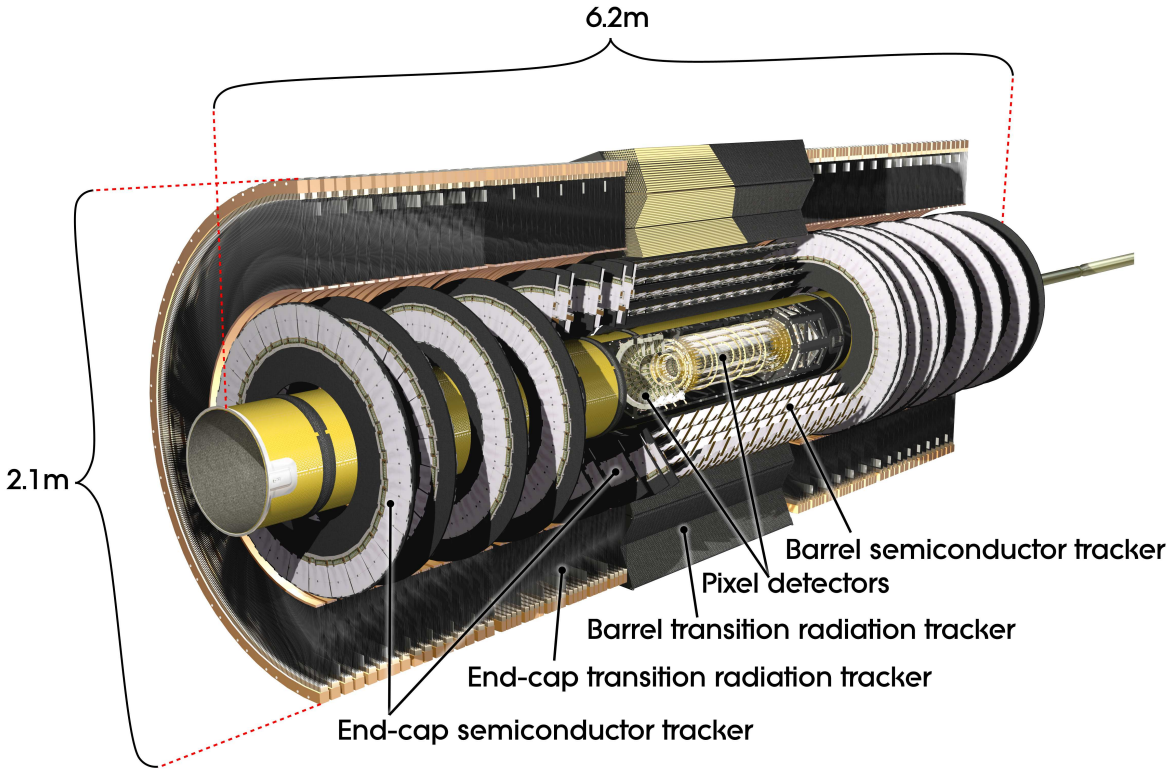

Figure 3.3: A computer generated schematic view of the ID. Taken from [68].

three layers. A total of 80.4 million read-out channels are used. The proximity to the beam pipe and high granularity measurements are necessary to reconstruct vertices for charged particles, where particle tracks point to a common origin.

Beyond the Pixel detector sits the SCT. This tracker also uses semiconductor technology to measure the passage of charged particles, but is built from strips rather than pixels. Each strip only gives information in two dimensions. However, the strips are mounted on both sides of a module with a stereo angle of 40 mrad between the two sides. Therefore, information from two sides of a module can be combined to give three dimensional measurements. The SCT consists of four barrel layers and 18 end-cap discs. Communication of data to and from the SCT is provided using optical-electronics links, which will be discussed in detail in Chapter 10.

The final layer of tracking is provided by the TRT. Straw drift tubes are arranged parallel with the z-axis in the barrel, providing information in the R-ϕ plane, while the straws are arranged radially in the end-caps, providing z and ϕ coordinate information. The TRT will

typically register 30 hits on a well reconstructed track. Foils with rapidly varying dielectric constant are arranged between the straws so that if a particle has a sufficiently high Lorentz γ factor it will emit X-ray photons, known as transition radiation. Therefore, low mass particles (electrons) will produce transition radiation, while heavier particles (hadrons) will not produce transition radiation. The TRT read-out distinguishes between hits without transition radiation and hits with transition radiation by setting a low threshold (LT) at 300 eV and high threshold (HT) at 6 keV. Only HT hits are considered to have produced transition radiation.

In order to provide bending of particle trajectories in the R-ϕ plane, such that their momenta can be measured, a 2 T solenoid magnet is located outside of the ID. The solenoid magnet has been designed to be as thin as possible to reduce the amount of showering in front of the calorimeters. This is achieved by using a single superconducting coil, cooled to 4.5 K, and by sharing the cryostat with the electromagnetic calorimeter.

3.4.2 Calorimetry

The ATLAS calorimeters are grouped into two main systems: the Electromagnetic Calorimeter (ECal), consisting of a Liquid Argon (LAr) barrel and LAr Electromagnetic End-Caps (EMECs); and the Hadronic Calorimeter (HCal), which is made up of a Tile Calorimeter (TileCal) barrel and LAr Hadronic End-Caps (HECs). Additional forward calorimetry is provided by the LAr Forward Calorimeters (FCals). The layout of the ATLAS calorimetry is shown in Figure 3.4. These calorimeters measure the energy of particles by inducing showering of the incident particle using absorbers and measuring the development of the shower using sampling layers.

The LAr barrel [78] has an acceptance of $|\eta| < 1.475$ and shares a cryostat with the solenoid magnet, in order to reduce the amount of material between the calorimeter and the beam pipe. The EMECs are coaxial wheels in separate cryostats that provide acceptance in the region $1.375 < |\eta| < 3.2$. A LAr presampler is also installed to make corrections for radiation in front of the detector in the region $|\eta| < 1.8$. The LAr barrel and the

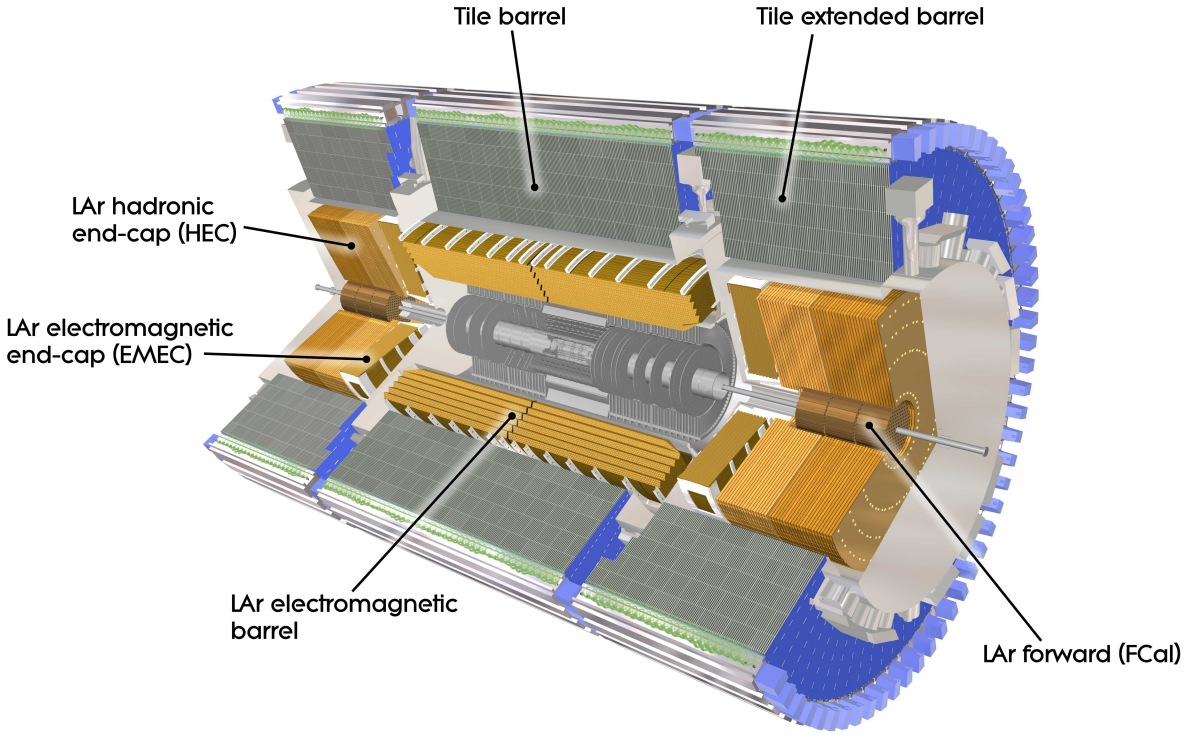

Figure 3.4: A computer generated schematic view of the calorimeters. Taken from [68].

EMECs use an accordion geometry of lead absorbers, providing full, symmetric coverage in ϕ. The thickness of the LAr barrel is > 22 radiation lengths, while the EMECs contain > 24 radiation lengths. In order to provide optimal energy resolution, the ECal is segmented into three sampling layers for $|\eta| < 2.5$ and two layers for $2.5 < |\eta| < 3.2$. The granularity of each layer varies with η as described in [68]. The segmentation and granularity of the ECAL allows different shower properties to be measured, for example the width and depth of the shower. The high granularity of the first layer also allows signatures of photons and electrons to be separated from the decay of neutral pions.

Outward from the ECal resides the HCal. In the barrel region the HCal is made up of the TileCal [79], which provides acceptance in the range $|\eta| < 1.0$. Two additional extended TileCal barrels cover the range $0.8 < |\eta| < 1.7$. Calorimetry is provided by alternating layers of steel wedge absorbers and scintillator tiles. This results in a thickness of > 9.7 interaction lengths. The scintillator signals are read out via wavelength shifting fibres, which send the scintillation light to photo-multipliers. LAr HECs provide acceptance in the

range $1.5 < |\eta| < 3.2$, while the forward-most coverage, of $3.1 < |\eta| < 4.9$, is provided by the FCals. The high $|\eta|$ acceptance of the HCal is vital to precision measurements of $E_{\mathrm{T}}^{\mathrm{miss}}$ as the forward region experiences a high particle flux during collisions. The HCAL is also designed in such a way as to allow the shapes of showers to be measured.

3.4.3 The muon spectrometer

The outer layer of detectors in ATLAS is responsible for measuring the trajectories of muons, which have small enough cross sections to traverse the calorimeter. The ATLAS MS consists of Monitored Drift Tubes (MDTs) and Cathode Strip Chambers (CSCs) for precision momentum measurements, while Resistive Plate Chambers (RPCs) and Thin Gap Chambers (TGCs) mostly provide input to the trigger. The magnetic field for momentum measurement is produced by a system of air-core toroids. A graphical representation of the muon system in ATLAS can be seen in Figure 3.5 and a summary is given in [80].

Precision measurements of muon tracks in the principle bending direction, R, over most of the acceptance range $|\eta| < 2.7$ are provided by MDTs. The MDTs are made up of tubes filled with gas that becomes ionised when traversed by a charged particle. A central wire then collects the electrons produced by ionisation and allows the signal to be read out. The MDTs are replaced by the CSCs for the inner layer in the acceptance range $2 < |\eta| < 2.7$ as this receives higher particle flux. The CSCs consist of four layers of radial multi-wire proportional chambers which read out on the cathode strips. In order to provide track measurements, the cathodes are segmented into strips perpendicular and parallel to the wires. Interpolation is used between neighbouring cathode strips to give the precise location of the hit.

The muon trigger covers the acceptance range $|\eta| < 2.4$ and the components focus on both providing trigger input and on providing the transverse track measurement. Measurements in the barrel region are performed by RPCs located in three concentric layers. These are made up of two separated resistive plastic laminate plates, with a gaseous mixture filling the gap. The passage of a charged particle across the gas causes break down and a charge avalanche forms. TGCs are used to trigger muons in the end-caps. These are multi-wire

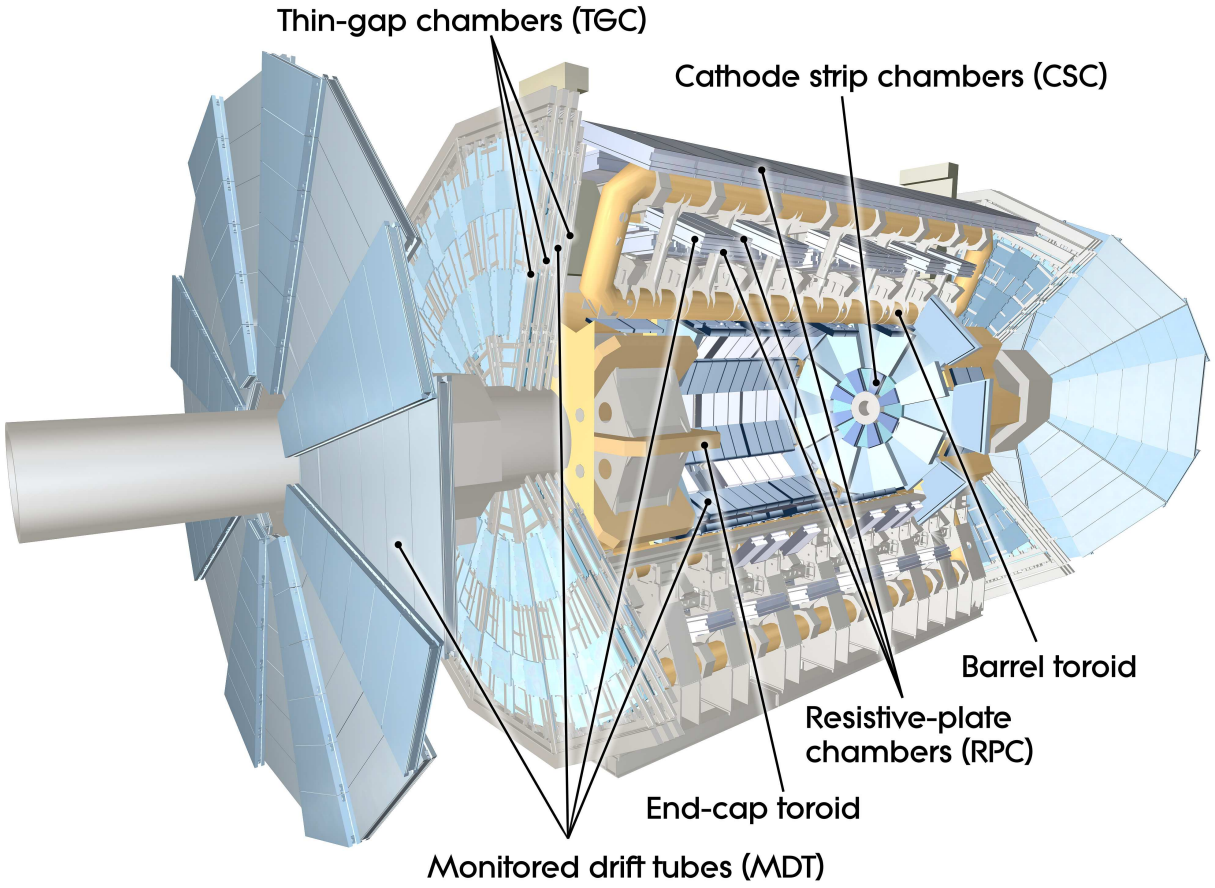

Figure 3.5: A computer generated schematic view of the MS. Taken from [68].

proportional chambers where the wire-to-cathode distance is smaller than the wire-to-wire distance. Such an arrangement gives very good time resolution.

Surrounding the muon system, apart from in the wheels, is an air-core toroidal magnet system. This provides bending in the R-z plane to allow the muon momentum to be measured. The barrel toroid consists of eight 'race track' shaped stainless steel vacuum vessels, which contain the superconducting magnets and cryostats. This system is cooled to 4.6 K, at which it can store a current of 20.5 kA. At this nominal current the bending power, characterised by the field integral $\int B\mathrm{d}l$, is between 1.5 Tm and 5.5 Tm. The end-cap toroids similarly consist of eight coils each and are stored in a single cryostat per end-cap. These end-cap magnets store the same current as the barrel toroids with bending power between 1 Tm and 7.5 Tm.

3.5 Object reconstruction and measurement

The signatures recorded by the detector are transformed into real physics objects, such as electrons, muons and jets, by using a set of algorithms. These calculate the properties of the tracks or calorimeter deposits in question and then classify the measurement. Much of what follows is described in more detail in [81].

3.5.1 Track reconstruction

Tracks are reconstructed in three stages. Initially, the space points generated from the SCT strip information are merged with the Pixel cluster information and the TRT data are transformed into calibrated drift circles. The second stage is track-finding, where a track is generated by extrapolating information from the three Pixel layers and the first SCT layer through the ID and performing a series of fits to control the track quality. After these tracks have been fully reconstructed, a post-processing stage is applied which implements vertex finding algorithms, followed by algorithms to search for photon conversions and secondary vertices. The resulting parameters from the fit to the ID hits are then used to calculate the momentum of the track.

3.5.2 Electron identification

The reconstruction and identification of electrons is based on a calorimeter seeded technique. A sliding-window algorithm [82] with size 5×5 cells is used to find energy depositions in the ECal. If the sum of the E_{T} contained in such a window exceeds the threshold of 3 GeV then a cluster seed is formed. Tracks that are not flagged as originating from a photon conversion are then extrapolated to the ECal and are matched to the cluster. This matching requires $\Delta\eta \times \Delta\phi < 0.05 \times 0.1$ and $E/p < 10$, where E is measured by the calorimeter and p is taken from the track. If a positive match is found, then the object is identified as an electron. In ATLAS terminology, this is termed as being reconstructed with the `AuthorElectron`

algorithm.

Further information can be included in the reconstruction of the electron, from both the ID and calorimeter. The precise definition of an electron is decided by the analysis according to their particular constraints on the purity of the sample and the required acceptance. Such criteria are termed loose, medium and tight selections, with loose giving lower purity but high acceptance and tight having high purity but lower acceptance. Examples of the information that goes into each of these definitions are

loose: Simple shower shape cuts in the middle ECal layer and loose matching between track and cluster.

medium: Extra shower shape cuts with information from the first ECal layer and track quality cuts.

tight: Tighter track matching with a hit in the first Pixel layer and a high ratio of HT to LT hits in the TRT. Isolation criteria are applied to the amount of activity allowed around the reconstructed electron cluster.

3.5.3 Jet reconstruction and energy measurement

All strongly interacting particles produced in a collision will result in a shower of particles, known as a jet, due to the asymptotic freedom[3] properties of Quantum Chromodynamics (QCD). The goal of jet reconstruction is to obtain a representation of the seed particle's four momentum by clustering calorimeter cells. In order to perform this reconstruction in a theoretically safe manner, a clustering algorithm must be implemented with the following constraints:

Infra-red safety: The algorithm should be insensitive to low p_{T} QCD radiation with respect to the seed particle so that the presence or absence of a low energy cell should

[3]The coupling between two strongly interacting particles increases as their separation increases. Eventually the potential energy stored between the two particles will get so high that new strongly interacting particles can be produced to bring the system to a lower energy state. Therefore, strongly interacting particles are only ever indirectly observed via confined states (apart from the top quark).

not affect the reconstruction of the jet.

Collinear safety: The algorithm should be insensitive to two particles being emitted in the same direction, or the equivalent energy being carried by only one particle.

In ATLAS, and throughout this thesis, the anti-k_{T} clustering algorithm [83] is used. This is applied to the cells in a calorimeter cluster that pass signal to noise thresholds, typically $E_{\mathrm{cell}} > 4\sigma_{\mathrm{cell}}$, in order to reduce the noise contribution to the jet energy. A radius parameter of $\Delta R = 0.4$ is used by the clustering algorithm in this thesis.

Having clustered the energy deposits, the energy of the jet must then be calibrated. This involves weighting the cell energies according to their position in the calorimeter, X_i, and the cell signal density, $\rho_i = E_i/V$, where V is the volume of the cell. The index i corresponds to a unique cell that is included in the jet cluster. The final reconstructed four-momentum of the jet is then given by

$$(E_{\mathrm{rec}}, \vec{p}_{\mathrm{rec}}^{\,\mathrm{jet}}) = \left(\sum_{i}^{N_{\mathrm{cells}}} w(\rho_i, \vec{X}_i) E_i, \sum_{i}^{N_{\mathrm{cells}}} w(\rho_i, \vec{X}_i) \vec{p}_i \right). \tag{3.6}$$

It should be noted that, for the purpose of the analysis presented here, hadronic taus are not distinguished from jets.

3.5.4 Muon reconstruction

Muons are reconstructed in ATLAS using either the MS on its own or in combination with the ID. This allows for different quality objects to be used in analyses as may be appropriate. Three methods of muon track reconstruction are used.

Standalone: Muon track reconstructed solely using the MS, with acceptance $|\eta| < 2.7$.

Combined: Combined fit using the muon track and an ID track, with acceptance $|\eta| < 2.5$.

Segment tagged: Combination of an inner detector track with a MS segment, with acceptance $|\eta| < 2.5$.

The matching between ID tracks and MS tracks or segments is performed using a χ^2-based statistical combination (STACO) algorithm.

Track reconstruction in the muon system follows a similar logical process to tracks in the ID - with a pre-processing stage to form drift circles, followed by a fitting stage to extract the track parameters. Additional corrections are made to the track momentum due to energy loss through the calorimeter, which is estimated using either the parametrised expected energy loss or the energy loss as measured by the calorimeter. The muon tracks can also be combined with ID tracks, which considerably improves the momentum resolution below 100 GeV, but can suppress backgrounds from punch-through[4] and the in-flight decays of pions or kaons.

3.5.5 Missing transverse energy reconstruction

As the collisions observed by ATLAS occur with a small crossing angle, it is possible to define the $E_{\mathrm{T}}^{\mathrm{miss}}$ variable (described in Section 3.3) under the assumption that the particle escaping the detector has no mass. The $E_{\mathrm{T}}^{\mathrm{miss}}$ is defined on an event-by-event basis by a global sum of the activity in the detector. The most basic definition is the sum of all of the calorimeter cell activity and the total energy of standalone muons. Corrections are applied to account for energy losses when crossing the cryostat between the LAr barrel and the TileCal. Additionally, cells that are associated with a high p_{T} object are replaced with the calibrated energy of that object. Cells that pass the calorimeter noise threshold but are not associated with a high p_{T} object are calibrated according to the weighting scheme defined in Section 3.5.3 and included in the $E_{\mathrm{T}}^{\mathrm{miss}}$ calculation (this is known as the cell-out term).

3.6 Trigger, data acquisition and computing

ATLAS implements a multi-level triggering system (Section 3.6.1) to reduce the rate at which data are collected so that they can be processed and stored. The extraction and storage of

[4]Punch-through occurs when a jet leaks into the muon system.

information from the detector are discussed in Section 3.6.2. Finally, the data must be accessible to a large number of users for analysis. To cope with this demand the Worldwide LHC Computing Grid (WLCG) [84] was developed, as will be detailed in Section 3.6.3.

3.6.1 The trigger system

The ATLAS trigger system consists of three levels. At level one (L1) the data rate is reduced from 40 MHz to 75 kHz, by searching for signals above a defined threshold in the MS and calorimeters. If a signal above threshold is found, then the data are passed to level two (L2), where particular regions of interest (RoI) are searched for. At the L2 stage sufficient event processing time is available for software trigger algorithms to be used and ID information to be included. This brings the data rate down below 3.5 kHz. Finally, the event filter (EF) uses an advanced software trigger to build the full event. After this stage the data rate is cut down to ~ 200 Hz, corresponding to a data volume rate of ~ 300 MB/s.

For example, the `EF_e20_medium` trigger, which is used in this analysis, is seeded at L1 by the `L1_EM14` trigger that fires when an ECAL deposit with $p_{\mathrm{T}} > 14$ GeV is observed. The event data is then passed to L2 in which the `L2_e20_medium` trigger fires if a RoI containing a medium electron with $p_{\mathrm{T}} > 20$ GeV is found. The event data and the RoI information are passed on to the EF in which the data is refined and triggered if the information available passes the `EF_e20_medium` trigger.

3.6.2 Data acquisition

The ATLAS data acquisition (DAQ) system reads the data off of the detector in events that pass L1, and stores them to await operations from L2. The RoI information is combined for input to L2, which makes the decision to pass or fail the event. If the decision is to fail the event, the data are permanently deleted. If the event is selected, then the full event information is built for EF input. The EF algorithms run on this data and, again, if a decision is made to fail the event the data are permanently lost. If the event is selected by

the EF, it is sorted into a data stream depending on which triggers it passed and the data are stored.

3.6.3 Computing and the grid

Each year ATLAS is expected to record 1 PB of data from the detector. In order to store the data in a way that is accessible for users to analyse, the WLCG was implemented. The full dataset is written to tapes at CERN's Tier-0 facility. The data are then copied to the 11 Tier-1 sites that are located around the world, where they are further distributed to the 160 smaller Tier-2 sites. Throughout this process the size of the data stored at each site is reduced dramatically by calculating information that is relevant for physics analyses and removing information that is generally not needed. Users can run their own code on the Tier-2 sites so that they only need to download the minimal amount of information that is necessary for their specific analysis.

Chapter 4

Event selection and object definitions

4.1 Data samples

During 2011 data-taking the ATLAS detector recorded data equivalent to an integrated luminosity of 5.2 fb^{-1}. However, some of this sample cannot be used in this analysis, due to detector conditions not being suitable for the required measurements. A good runs list (GRL) is used[1], which removes approximately 11% of the data, as shown in Table 4.1, leaving a total integrated luminosity of 4.7 fb^{-1} for analysis. The average error on the luminosity measurement over the 2011 dataset is 3.9%.

The luminosity is measured in short time intervals, known as Luminosity Blocks (LBs). The luminosity detectors and algorithms count events in order to calculate the integrated luminosity over the given LB. These LBs are then combined into Runs, corresponding to phases of stable data taking, and these Runs are combined into Periods, over which the machine and trigger conditions are stable. A summary of these Periods and their corresponding integrated luminosities before and after the GRL selection is given in Table 4.1.

[1]Specifically `data11_7TeV.periodAllYear_DetStatus-v36-pro10_CoolRunQuery-00-04-08_Susy.xml`

Period	Run Number	Date [dd/mm/yy]	Before GRL	After GRL
B	178044 - 178109	22/03/11 - 24/03/11	16.8 pb^{-1}	11.7 pb^{-1}
D	179710 - 180481	14/04/11 - 29/04/11	178 pb^{-1}	167 pb^{-1}
E	180614 - 180776	30/04/11 - 03/05/11	49.9 pb^{-1}	48.8 pb^{-1}
F	182161 - 182486	17/05/11 - 25/05/11	151 pb^{-1}	132 pb^{-1}
G	182726 - 183462	27/05/11 - 14/06/11	558 pb^{-1}	508 pb^{-1}
H	183544 - 184169	16/06/11 - 28/06/11	277 pb^{-1}	259 pb^{-1}
I	185353 - 186493	13/07/11 - 29/07/11	398 pb^{-1}	338 pb^{-1}
J	186516 - 186755	30/07/11 - 04/08/11	232 pb^{-1}	226 pb^{-1}
K	186873 - 187815	04/08/11 - 22/08/11	658 pb^{-1}	590 pb^{-1}
L	188902 - 190343	07/09/11 - 05/10/11	1.56 fb^{-1}	1.40 fb^{-1}
M	190608 - 191933	07/10/11 - 30/10/11	1.12 fb^{-1}	1.03 fb^{-1}
Total	178044 - 191933	22/03/11 - 30/10/11	5.20 fb^{-1}	4.71 fb^{-1}

Table 4.1: Summary of the Periods of ATLAS 2011 data-taking. Only ranges where good quality data exists are shown for corresponding Run numbers and dates. The integrated luminosity before and after the GRL is applied are shown.

4.2 Background Monte Carlo samples

MC samples were produced for the various physics processes that are expected to contribute as backgrounds to this analysis. The samples that are considered, along with the event generators used and the calculated total cross sections, are summarised in Table 4.2. For events generated with `Alpgen`, the matrix element is calculated with zero to five or more additional partons for W+jets, Z+jets and $t\bar{t}$, in order to improve the modelling of events with many jets in the final state. Relevant multiplicative factors are applied to extract the cross section per parton bin.

The parton distribution function (PDF) sets used are: `CTEQ6L1` [91] for `Alpgen` samples; `CT10` [92] for `MC@NLO` samples; and `MRSTMCal(LO**)` [93] for `Herwig` samples. Cross sections are calculated using: `FEWZ` [87] with the `MSTW2008NLO` [62] PDF set for W+jets and Z+jets; `HATHOR1.2` [86] with the `MSTW2008NLO` PDF set for $t\bar{t}$; and `MCFM` [90] with the `MSTW2008NLO` PDF set for dibosons. The combination of PDF sets, matrix element generators and cross section calculations are important for the reasons introduced in Section 2.4. The composite nature of protons means that the PDFs are required to find how the protons' momenta are distributed across their constituent partons. According to these momentum distributions,

Physics Process	Generator	Cross section [nb]
$t\bar{t}$	Alpgen2.13 [85]	0.165 NLO+NLL [86]
$W(\to \ell\nu)$+jets	Alpgen2.13 [85]	10.46 NNLO [87]
$Z(\to \ell\ell)$+jets ($m_{\ell\ell} > 40$ GeV)	Alpgen2.13 [85]	1.07 NNLO [87]
single top (t channel)	MC@NLO4.01 [88]	0.0071 NLO [88]
single top (s channel)	MC@NLO4.01 [88]	0.0005 NLO [88]
single top (Wt)	MC@NLO4.01 [88]	0.0146 NLO [88]
WW	Herwig6.5.20 [89]	0.0449 NLO [90]
WZ ($66 < m_Z < 116$ GeV)	Herwig6.5.20 [89]	0.0449 NLO [90]
ZZ ($m_Z < 60$ GeV)	Herwig6.5.20 [89]	0.0060 NLO [90]

Table 4.2: SM background processes simulated in this analysis. The generator used is shown along with the theoretical cross section.

the matrix elements for the process of interest are produced and then the cross sections are calculated. The various PDF sets are generated by different groups, with some subtle differences such as which datasets are used and the treatment of quark masses. Each matrix element generator also has unique attributes and is produced by a particular group. For example, MC@NLO provides matrix elements at next-to-leading order, while Alpgen generates matrix elements at leading order and allows control over the number of additional partons that are generated. The cross sections are then generally calculated at higher order than the matrix elements and applied as corrections to the cross sections provided by the matrix element generators.

The partons produced in the matrix elements generated by Alpgen are propagated into the parton shower and hadronisation process using MLM matching [94]. The showering of partons and hadrons is performed using Herwig, with the simulation of the underlying event provided by the Jimmy [95] interface. An additional correction is applied to the simulation of underlying event using the ATLAS AUET2 [96] tunes. Particles are then propagated through the ATLAS detector using GEANT4 [97] to simulate showering and smearing due to detector effects. All MC events are fed through a similar simulation chain.

The detector conditions observed during data taking are then overlaid on the events. This overlay includes the simulation of minimum bias events corresponding to multiple pp interactions in a given BC, known as pileup. These additional interactions are generated

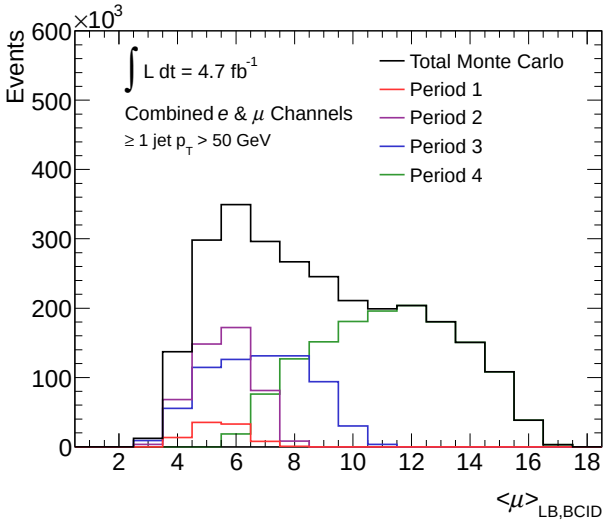

Figure 4.1: The $\langle\mu\rangle_{\mathrm{LB,BCID}}$ distributions in the different MC Periods. The MC are divided into the Periods listed in Table 4.3. Events are selected with one lepton and a jet with $p_{\mathrm{T}} > 50$ GeV to satisfy requirements of the muon trigger and the multijets background determination.

using `PYTHIA6` [98]. The overlay is performed so that the average number of minimum bias interactions per BC identifier[2] (BCID) and per LB ($\langle\mu\rangle_{\mathrm{LB,BCID}}$) in MC is matched to that in data for particular sets of Periods. The $\langle\mu\rangle_{\mathrm{LB,BCID}}$ distributions for each of these MC Periods are shown in 4.1. As well as overlaying minimum bias interactions, this also allows additional information from detector sub-systems to be matched to data. A summary of the detector conditions simulated in the different MC Periods is given in Table 4.3. Primarily, the implementation of Table 4.3 involves removing trajectories in particular regions of the detector that are no-longer operating as intended.

MC Period	1	2	3	4
Data Periods	B - D	E - H	I - K	L - M
Failed LAr FEBs	0	6	2	2
Failed TileCal modules	5	6	7	9
Failed Pixel modules	54	56	62	63
Failed B-layer modules	7	7	10	10

Table 4.3: Summary of the MC Periods of the ATLAS 2011 simulation. The corresponding data Periods are given along with the number of non-operational components in various sub-detectors that are accounted for in the simulation.

[2]Each potential crossing of the bunches at a particular point on the LHC ring for one full revolution of the machine is assigned a BCID. As the BCIDs are filled by transferring bunches from the SPS to the LHC, the luminosity in each BCID will tend to differ from the other BCIDs in that fill.

Having generated all of the particle trajectories for each event, the samples are then passed through digitisation algorithms to simulate the response of the detector. These detector responses are finally fed through reconstruction algorithms to produce the properties of the physics objects in that given event. The simulated MC events are passed through the same reconstruction algorithms as the recorded data, in order to facilitate the comparison of predictions with observations.

4.3 Trigger selection

A trigger selection has already been applied to the observed data in order to reduce the data-taking rate to a manageable level. However, the appropriate triggers for this analysis must be applied to both the observed data and the MC. The lowest un-prescaled[3] single lepton triggers for a particular Period of data-taking are used. As the luminosity observed by ATLAS tended to increase throughout 2011 data-taking, triggers that were un-prescaled in early Periods may become prescaled in later Periods. In the cases where this change of trigger means a significant change in trigger efficiency, the trigger must also be changed in MC.

4.3.1 Triggers in data

The observed data are split into multiple streams, of which the `Egamma` and `Muons` streams are of interest here. The triggers used for each data Period are given in Table 4.4.

In the case of the `Egamma` stream, the `EF_e20_medium` trigger is used for Periods B through J, while for Period K the `EF_e22_medium` trigger is used. Both of these triggers have efficiency $\geq 97\%$ for the selection of electrons with $p_{\mathrm{T}} > 25$ GeV [99]. The latest Periods (L through M) require a tighter definition of electrons to maintain a low p_{T} threshold while remaining un-prescaled. Additional requirements on hadronic activity and η-dependent p_{T} thresholds

[3]The lowest un-prescaled trigger is defined as the trigger that has the lowest lepton p_{T} threshold while having a rate that is low enough to select all events that would potentially pass it.

are also applied at Level 1. This trigger is known as EF_e22vh_medium1. Plateau efficiency is reached for electrons with $p_{\mathrm{T}} > 25$ GeV, although in this case the plateau efficiency is 95%. To recover efficiency losses at high electron p_{T}, this trigger is used in a logical OR with the EF_e45_medium1 trigger.

For the Muons stream, the EF_mu18 trigger is used for Periods B through I. This reaches plateau efficiency at 73% in the barrel and 86% in the end-caps for muons with $p_{\mathrm{T}} > 20$ GeV [100]. The latest Periods (J through M) have the additional requirement of a jet with $p_{\mathrm{T}} > 10$ GeV at Level 1. This keeps the data-taking rate low enough to remain unprescaled without raising the muon p_{T} cut. This trigger is known as EF_mu18_L1J10 and has similar efficiencies in the barrel and end-caps to EF_mu18, after a cut of $p_{\mathrm{T}}^{\mathrm{jet}} > 50$ GeV has been applied to the analysis. The loss of efficiency in the muon triggers is a result of the support structures that keep the muon chambers and the toroid magnet off of the ground. These cause acceptance losses when objects travel towards these muon 'feet'.

4.3.2 Triggers in Monte Carlo

The triggers used for the electron and muon selections in MC are also shown in Table 4.4. The change in trigger in the electron channel is made possible by the division of the MC samples into Periods according to Table 4.3.

Period	**Trigger in data**	**Trigger in MC**
	Electron	
B-J	EF_e20_medium	EF_e20_medium
K	EF_e22_medium	EF_e20_medium
L-M	EF_e22vh_medium1 OR EF_e45_medium	EF_e22vh_medium1 OR EF_e45_medium
	Muon	
B-I	EF_mu18	EF_mu18
J-M	EF_mu18_L1J10	EF_mu18

Table 4.4: Triggers used in data and MC for the electron and muon selections.

4.4 Object definitions

The detector produces a set of electronic responses, rather than definitive particle signatures. In order to definitively map the responses to physical particles it is necessary to explicitly define what is meant by electrons, muons, jets and $E_{\mathrm{T}}^{\mathrm{miss}}$. In general, objects are defined first at a pre-selection stage, with basic definitions that have high efficiencies but may also have larger fake-rates. These definitions are used for lepton counting and overlap removal. The objects that are used directly in the analysis have additional selection criteria, which reduce the fake-rates but also give lower efficiencies. Requirements on the p_{T} of objects to be in the plateaus of the trigger efficiencies are also employed at this stage. This analysis uses object definitions as given in [101] and [102]. These are summarised for jets in Table 4.5, electrons in Table 4.6 and muons in Table 4.7.

The reconstruction methods used by ATLAS result in electrons being reconstructed as jets. Therefore, all pre-selected electrons must first be removed from the list of jets in the event. To do this, electrons (and muons) are defined at the pre-selection stage apart from the overlap requirement. Jets are then removed if they overlap with a pre-selected electron within $\Delta R < 0.2$ in η-ϕ space. After this, electrons and muons are removed if they overlap with any remaining jets within $\Delta R < 0.4$ in η-ϕ space.

All object definitions are implemented using tools in the software package [103].

The selections are generally implemented with p_{T} cuts at the pre-selection stage to ensure that the objects can be well calibrated, and the p_{T} cuts are then raised at the signal stage to be either in the trigger plateau, as is the case for leptons, or to further improve the calibration, as is the case for jets. The cuts on η are driven by the acceptances of the relevant detectors, in particular the change in the jet acceptance is forced by the inclusion of the j_{vf} variable, described in detail in Chapter 9, which requires inner detector information. Further cuts are then applied to remove objects for which the response in the detector looks like it may be either an incorrectly identified object or noise.

Cut	Variable/description	
	Pre-selected jet	
Algorithm	`AntiKt4`	
Calibration	`TopoNewEM`	
Quality	Veto event if `VeryLooseBad`	
Acceptance	$p_{\mathrm{T}} > 20$ GeV, $\lvert\eta\rvert < 2.8$	
Overlap	$\Delta R(\mathrm{jet}, e) > 0.2$	
	Signal jet	
	No b-tag	b-tag
Acceptance	$p_{\mathrm{T}} > 25$ GeV, $\lvert\eta\rvert < 2.5$	$p_{\mathrm{T}} > 25$ GeV, $\lvert\eta\rvert < 2.5$
Pileup rejection	$j_{\mathrm{vf}} > 0.75$	$j_{\mathrm{vf}} > 0.75$
Track matching	—	$\Delta R(\mathrm{jet}, \mathrm{track}) < 0.4$
b-tagger	—	`JetFitterCombNN` > 1.8

Table 4.5: Summary of the object definitions for jets at the pre-selection stage and at the signal stage (without and with b-tagging). The signal selection is applied in addition to the pre-selection. For the bad quality jet veto, all jets with $p_{\mathrm{T}} > 20$ GeV and any $\lvert\eta\rvert$ value are considered to prevent contamination in the $E_{\mathrm{T}}^{\mathrm{miss}}$ calculation.

Cut	Variable/description
	Pre-selected electron
Algorithm	`AuthorElectron`
Acceptance	$p_{\mathrm{T}} > 10$ GeV, $\lvert\eta^{\mathrm{cl}}\rvert < 2.47$
Quality	`medium++`
Cluster information	Not `BadClusElectron`
Overlap	$\Delta R(e, \mathrm{jet}) > 0.4$
	Signal electron
Acceptance	$p_{\mathrm{T}} > 25$ GeV
Quality	`tight++`
Trigger match	$\Delta R(e^{\mathrm{reco}}, e^{\mathrm{trig}}) < 0.15$
Isolation	`ptcone20`$/p_{\mathrm{T}} < 0.1$

Table 4.6: Summary of the object definitions for electrons at the pre-selection stage and at the signal stage. The signal selection is applied in addition to the pre-selection.

Cut	Variable/description
	Pre-selected muon
Algorithm	`STACO`, segment-tagged or combined
Acceptance	$p_{\mathrm{T}} > 10$ GeV, $\lvert\eta^{\mathrm{cl}}\rvert < 2.4$
Quality	`loose`
ID track	Number of b-layer hits (if expected) ≥ 1
	Number of pixel hits + number of crossed dead pixel sensors ≥ 2
	Number of SCT hits + number of crossed dead SCT sensors ≥ 6
	Number of pixel holes + number of SCT holes < 3
	If $\lvert\eta^{\mathrm{track}}\rvert < 1.9$: $n^{\mathrm{TRT}}_{\mathrm{hits}} \geq 6$, $n^{\mathrm{TRT}}_{\mathrm{outliers}} < 0.9\, n^{\mathrm{TRT}}_{\mathrm{hits}}$
	If $\lvert\eta^{\mathrm{track}}\rvert > 1.9$ and $n^{\mathrm{TRT}}_{\mathrm{hits}} \geq 6$: $n^{\mathrm{TRT}}_{\mathrm{outliers}} < 0.9\, n^{\mathrm{TRT}}_{\mathrm{hits}}$
Overlap	$\Delta R(\mu, \mathrm{jet}) > 0.4$
	Cosmic muon
Cosmic veto	Veto event if $\lvert z_0\rvert > 1$ mm or $\lvert d_0\rvert > 0.2$ mm
	Poorly reconstructed muon
Reconstruction veto	Veto event if $\sigma(q/p)/\lvert q/p\rvert > 0.2$
	Signal muon
Acceptance	$p_{\mathrm{T}} > 20$ GeV
Trigger match	$\Delta R(\mu^{\mathrm{reco}}, \mu^{\mathrm{trig}}) < 0.15$
Isolation	$\Sigma p_{\mathrm{T}}(\Delta R(\mu, \mathrm{track}) < 0.2) < 1.8$ GeV excluding muon track

Table 4.7: Summary of the object definitions for muons at the pre-selection stage and at the signal stage. The signal selection is applied in addition to the pre-selection. The cosmic and poor reconstruction vetoes are also shown. For cosmic muons the veto is applied after overlap, while for poorly reconstructed muons the veto is applied regardless of proximity to jets, otherwise the veto definitions are applied in addition to the pre-selection.

4.4.1 Missing transverse momentum

In this analysis $E_{\mathrm{T}}^{\mathrm{miss}}$ is defined as the transverse momentum vector opposite from the vectorial sum of the following reconstructed objects:

- Jets calibrated at the EM+JES scale with $p_{\mathrm{T}}^{\mathrm{jet}} > 20$ GeV;
- The signal lepton;
- Additional non-isolated muons;
- Topological calorimeter clusters not associated with an object listed above, which are calibrated at the EM scale (the cell-out term).

4.5 Event cleaning

Even events that have passed both the GRL and trigger selections may contain poorly reconstructed objects, or objects from sources that could be detrimental to the analysis. Therefore, the following additional selections are applied:

Jet and $\boldsymbol{E}_{\mathbf{T}}^{\mathbf{miss}}$ cleaning: The event is vetoed if it contains a jet flagged as being poorly measured or if the LAr barrel calorimeter reports an error. These criteria prevent poorly reconstructed jets entering the analysis and protect the $E_{\mathrm{T}}^{\mathrm{miss}}$ calculation from calorimeter noise bursts.

LAr hole veto: Certain Periods of ATLAS data in 2011 contain response holes in the LAr barrel calorimeter. These are due to malfunctioning front-end boards (FEBs), as listed in Table 4.3. This veto considers all pre-selected jets that point towards such a hole and vetoes the event if the estimated non-measured energy in the jet has a large impact on $E_{\mathrm{T}}^{\mathrm{miss}}$. This cut is documented in [104];

Primary vertex cut: The highest $\sum_{\mathrm{tracks}} p_{\mathrm{T}}^{\mathrm{tracks}}$ vertex must be associated with at least five tracks. This ensures that the event has a well reconstructed primary vertex;

Cosmic and bad muon veto: If an event is found to contain a cosmic muon, according to Table 4.7, the event is vetoed. Similarly, any event containing a muon with poorly

reconstructed momentum is vetoed. Both of these criteria are implemented to protect the $E_{\mathrm{T}}^{\mathrm{miss}}$ calculation.

4.6 Monte Carlo correction factors and uncertainties

Certain aspects of the MC, such as efficiencies and energy measurement, may not perfectly match data even after the event selection and cleaning have been applied. However, it is possible to estimate the degree to which these quantities disagree and to correct for them.

These correction factors will, in general, have a level of uncertainty associated with them. Uncertainties are propagated through the analysis by adjusting the source by one standard deviation in the positive and negative directions and observing the effect on the resulting distributions. A summary of these corrections and uncertainties follows:

Jet energy scale: It is possible to extract the calibration of jets using various methods. In the ATLAS dataset studied here, MC comparisons with data, test beam measurements and analysis of pp collision data collected in 2010 are used to estimate the calibration factors and their uncertainty [105]. Uncertainties are considered for light jets, heavy flavour jets and events with large jet activity, with values provided by [106]. The accuracy to which the jet energy scale can be determined is often a dominant source of uncertainty in experiments at the LHC due to the complex nature of jets and the large numbers of particles produced per BC, see for example [107]. The uncertainty on the p_{T} of a given jet varies from about 2% to 14%, however the resulting effect on the number of events passing a given selection can vary in a non-trivial manner;

Electron energy scale and resolution: Corrections to the measurement of the energy of electrons are derived by measuring the properties of well understood processes, such as the width and central value of the $Z \to \ell\ell$ and $J/\psi \to \ell\ell$ resonances [108]. Further corrections are applied to correct the momenta of electrons that fall in the crack region of the ECal, in the range $1.37 < |\eta| < 1.52$. The corrections and resulting uncertainties are applied using [109]. The effect of the uncertainty on the measurement of the electron

p_{T} varies from about 0.3% to 1.6%;

Muon ID and MS resolution: Measurements of the muon momenta are performed independently in the inner detector and the muon spectrometer. Therefore, corrections are applied to measurements by these systems individually. The corrections are derived by comparing the p_{T} spectra in data and MC and are applied via a smearing function [110]. The values for the corrections and their uncertainties are provided by [111]. The uncertainty on the muon resolution scale factors are below 1%;

$\boldsymbol{E}_{\mathbf{T}}^{\mathbf{miss}}$ terms: The corrections to the above measurements and their uncertainties are propagated into the $E_{\mathrm{T}}^{\mathrm{miss}}$ calculation as appropriate. Additionally, corrections and uncertainties are applied to account for the cell-out term and for pileup. The necessary modifications to the $E_{\mathrm{T}}^{\mathrm{miss}}$ calculation are provided by [112];

Lepton reconstruction and trigger efficiencies: Corrections relating to the lepton reconstruction and trigger efficiencies are estimated using the 'tag-and-probe' technique. This involves measuring a resonance using one lepton with tight selection criteria, the tag, and another lepton with loose criteria, the probe. The corresponding efficiency is the rate at which loose probes are accepted by the tight criteria. The corrections and associated uncertainties for electrons and muons are provided by [109] and [113], respectively. The uncertainties on lepton reconstruction and trigger efficiencies are generally at or below the 1% level;

***b*-tagging efficiency:** In regions of the analysis where a jet definition requiring b-tagging is employed, corrections to the associated efficiency are applied on a jet-by-jet basis. These corrections are derived from datasets which study $t\bar{t}$ events or jets containing muons [114]. The corrections and corresponding uncertainties are provided by [115]. The uncertainty on the b-tagging scale factors vary from about 7% at low $p_{\mathrm{T}}^{\mathrm{jet}}$ to 17% at high $p_{\mathrm{T}}^{\mathrm{jet}}$;

$\boldsymbol{p}_{\mathbf{T}}^{\boldsymbol{W}}$ reweighting: Comparisons between the W-boson p_{T} (p_{T}^{W}) spectrum in the MC dataset generated with `Alpgen` and the observed data show a slope, which indicates that `Alpgen` produces W bosons with higher p_{T} than observed in data [101]. The p_{T}^{W} can potentially have a large effect on this analysis as it modifies the expected lepton p_{T} and the $E_{\mathrm{T}}^{\mathrm{miss}}$.

In order to remedy this effect, the p_{T}^{W} is taken from events generated using `Sherpa` [116]. This correction is performed by producing a reweighting function in p_{T}^{W}, corresponding to the ratio between `Sherpa` and `Alpgen` at truth level. Scale factors produced from this are applied on an event-by-event basis. This method is described and studied in detail in [102]. The uncertainty on the p_{T}^{W} reweighting is estimated by removing the p_{T}^{W} weights. The range of this uncertainty is then made to be symmetric about the nominal distribution that has the weights applied. As the weighting is performed as a function of p_{T}^{W}, the size of this uncertainty will vary from about 5% at low p_{T}^{W} to 28% at high p_{T}^{W}.

4.7 Theoretical uncertainties

Certain decisions have to be made when configuring the generators used in this analysis. As the dominant backgrounds are estimated using `Alpgen`, uncertainties relating to this generator are considered, with motivation from discussions with the author of `Alpgen` [102]. The statistical model introduced in Section 7.6 is sensitive to theoretical uncertainties that affect the shape of distributions, rather than uncertainties that affect the total cross section of the backgrounds. As such, only theoretical uncertainties affecting the shape of kinematic variables are considered for the background samples. Uncertainties on the cross sections of signal samples must also be considered when testing specific theoretical models. Theoretical uncertainties in this analysis are discussed in detail in [101, 102] and are summarised below:

Generator scale: The factorisation scale in `Alpgen` gives an overall scaling to the total cross section, and so is not considered in this analysis. However, the renormalisation scale is concerned with the k_{T} of each vertex in the calculation and so can affect the jet multiplicity of the resulting events. This is applied in the analysis as an additional scaling of each individual N_{parton} sample, according to expectations when the k_{T} parameter is set to twice or half of its nominal value;

MLM matching threshold: Another theoretical parameter that can have an important

effect on the shape of kinematic distributions is the choice of the MLM matching threshold, $p_{\mathrm{T}}^{\mathrm{min}}$. This parameter prevents double counting of jet multiplicities between the matrix element and parton shower stages of the calculation. Initially, partons are generated with $p_{\mathrm{T}} > p_{\mathrm{T}}^{\mathrm{min}}$ and showered, but not hadronised. The showered products are clustered into jets with parameters $E_{\mathrm{T}}^{\mathrm{min}} > p_{\mathrm{T}}^{\mathrm{min}} + 5$ GeV and a cone radius $\mathrm{R} < 0.4$. Partons are associated with the nearest jet and are considered matched if $\Delta\mathrm{R}(\mathrm{parton}, \mathrm{jet}) < 0.4$. If the number of matched partons does not equal the number of generated partons, then the event is discarded. The default value for this parameter is $p_{\mathrm{T}}^{\mathrm{min}} = 15$ GeV. The uncertainty is estimated by generating events with $p_{\mathrm{T}}^{\mathrm{min}} = 30$ GeV and considering the overall change in the predicted rate for each jet multiplicity bin in the control regions, or the overall rate in the signal regions;

Signal cross section calculation: The uncertainty on the calculated signal cross section is estimated as part of the nominal cross section calculation by comparing events generated using different PDF sets. This is described in detail in Section 5.3.1;

Initial state radiation: An additional uncertainty is considered for the Simplified SUSY Model signal points (introduced in Section 5.3.3), to account for the effect of initial state radiation (ISR). ISR occurs when a parton in the initial state of the matrix element radiates and can result in a harder SUSY interaction. If this happens, then the SUSY cascade will have a boost, which may make it easier to detect scenarios with low mass differences that would otherwise have low p_{T} and fail the acceptance cuts of the analysis. To estimate the impact of this effect, a parametrised form of the scaling of the cross section is used, as described in [102], for signal points where the mass difference between the gluino and the LSP is less than 300 GeV.

4.8 Kinematic distributions after selection

After applying the event and object selections defined above it is worth checking the agreement between the observed data and the SM estimates. This is done at this stage to ensure that there are no clear additional corrections that should be applied and that all the SM

backgrounds have been accounted for. Two selections are implemented: the first requires one lepton plus three jets, where the leptons are selected according to Tables 4.6 and 4.7, the highest p_{T} signal jet has $p_{\mathrm{T}}^{\mathrm{jet}_1} > 100$ GeV and the third highest p_{T} signal jet has $p_{\mathrm{T}}^{\mathrm{jet}_3} > 25$ GeV; the second selection requires one lepton, as defined in Tables 4.6 and 4.7, plus four jets, all of which have $p_{\mathrm{T}}^{\mathrm{jet}} > 80$ GeV. The distributions used to check this agreement are m_{T}, $E_{\mathrm{T}}^{\mathrm{miss}}$ and $m_{\mathrm{eff}}^{\mathrm{inc}}$. Where

$$m_{\mathrm{T}} = \sqrt{2p_{\mathrm{T}}^{\ell} E_{\mathrm{T}}^{\mathrm{miss}}(1 - \cos(\Delta\phi(\vec{p}_{\mathrm{T}}^{\ell}, \vec{p}_{\mathrm{T}}^{\mathrm{miss}})))}, \tag{4.1}$$

and

$$m_{\mathrm{eff}}^{\mathrm{inc}} = E_{\mathrm{T}}^{\mathrm{miss}} + p_{\mathrm{T}}^{\ell} + \sum_{\mathrm{jet}} p_{\mathrm{T}}^{\mathrm{jet}}. \tag{4.2}$$

In these equations, a superscript ℓ indicates that the property is assigned to an electron or muon and $\Delta\phi$ is the angle between the two vectors in the argument in the x-y plane. The sum in $m_{\mathrm{eff}}^{\mathrm{inc}}$ runs over all jets that pass the signal jet selection in that event. These distributions can be seen in Figure 4.4. The multijet background is determined according to the prescription detailed in Section 6.1.

In the 3-jet distributions, the W+jets contribution is larger than the $t\bar{t}$ contribution in most bins. Therefore, the p_{T}^{W} correction has a more appreciable affect in this region when compared to the 4-jet region, which generally has larger $t\bar{t}$ rates than W+jets. The agreement between data and MC is generally good, in particular the m_{T} and $E_{\mathrm{T}}^{\mathrm{miss}}$ distributions have a similar shape and normalisation in the 3-jet region. This will be important when performing the background estimates, as the rates of W+jets and $t\bar{t}$ will be extrapolated from control regions into the signal regions using these variables. There is some evidence for a downward slope in the $m_{\mathrm{eff}}^{\mathrm{inc}}$ variable in the 3-jet region, however.

In the 4-jet region, the numbers of events start to become low in data for more moderate values of the plotted variables. However, a systematic shift downwards in the SM prediction

compared to the observed data is present. The background estimation technique for W+jets and $t\bar{t}$ employed by this analysis, as described in Section 6.2, involves simultaneously fitting the rate of W+jets and $t\bar{t}$ in control regions. Therefore, if this shift remains in the control regions, one can expect the fit to account for this by modifying the overall normalisation of the W+jets or $t\bar{t}$ samples.

The $E_{\mathrm{T}}^{\mathrm{miss}}$ distribution falls rapidly in the standard model. This is because in events with real $E_{\mathrm{T}}^{\mathrm{miss}}$, such as W+jets, the distribution corresponds to the p_{T} of the neutrino, while events with fake $E_{\mathrm{T}}^{\mathrm{miss}}$ such as many multijets events the distribution falls even faster and only significantly populates the first few bins. SUSY may be manifest in this distribution by a flattening at high $E_{\mathrm{T}}^{\mathrm{miss}}$ values corresponding to the measurement of the energy that is carried away from the event by the LSP. As both the 3-jet and 4-jet distributions do not show significant signs of flattening, then there is no clear evidence for signs of new physics.

The m_{T} distribution peaks close to the W mass as it is essentially measuring the invariant mass of the W after a transformation into the transverse plane. However, at m_{T} values greater than the W mass the distribution falls very quickly before flattening in the extreme tail. Events in the tail of the distribution, in the SM prediction, will mainly be a result of either the W width or from mismeasurement of the $E_{\mathrm{T}}^{\mathrm{miss}}$ or p_{T}^{ℓ}. New physics signals, such as SUSY, will tend to over populate the tail of this distribution as the parent particle may not be a W and so the invariant mass transformation will no longer be valid. There is no sign of over population in the tail, however, and so there is no clear sign of new physics in this distribution.

The $m_{\mathrm{eff}}^{\mathrm{inc}}$ distribution gives an indication of the total energy in the event. As new physics generally requires new particles to be produced with masses larger than those present in the SM, it would be expected that any new physics signals, such as SUSY, will increase the number of events in the tail of this distribution. Again, these is not a clear significant excess in the tail of this distribution and so there is no clear sign of new physics.

In summary, it appears that there is good agreement with the SM in all of these distributions and that there are no significant signs of new physics that are manifest in the ways

that one would expect if a strong new physics signal was present. It should be noted that the selection cuts applied to these distributions are quite loose and so one would only expect to see new physics signals with large cross sections compared to the SM in these distributions. The next part of this thesis will introduce cuts and techniques to improve the sensitivity to more subtle signs of potential new physics.

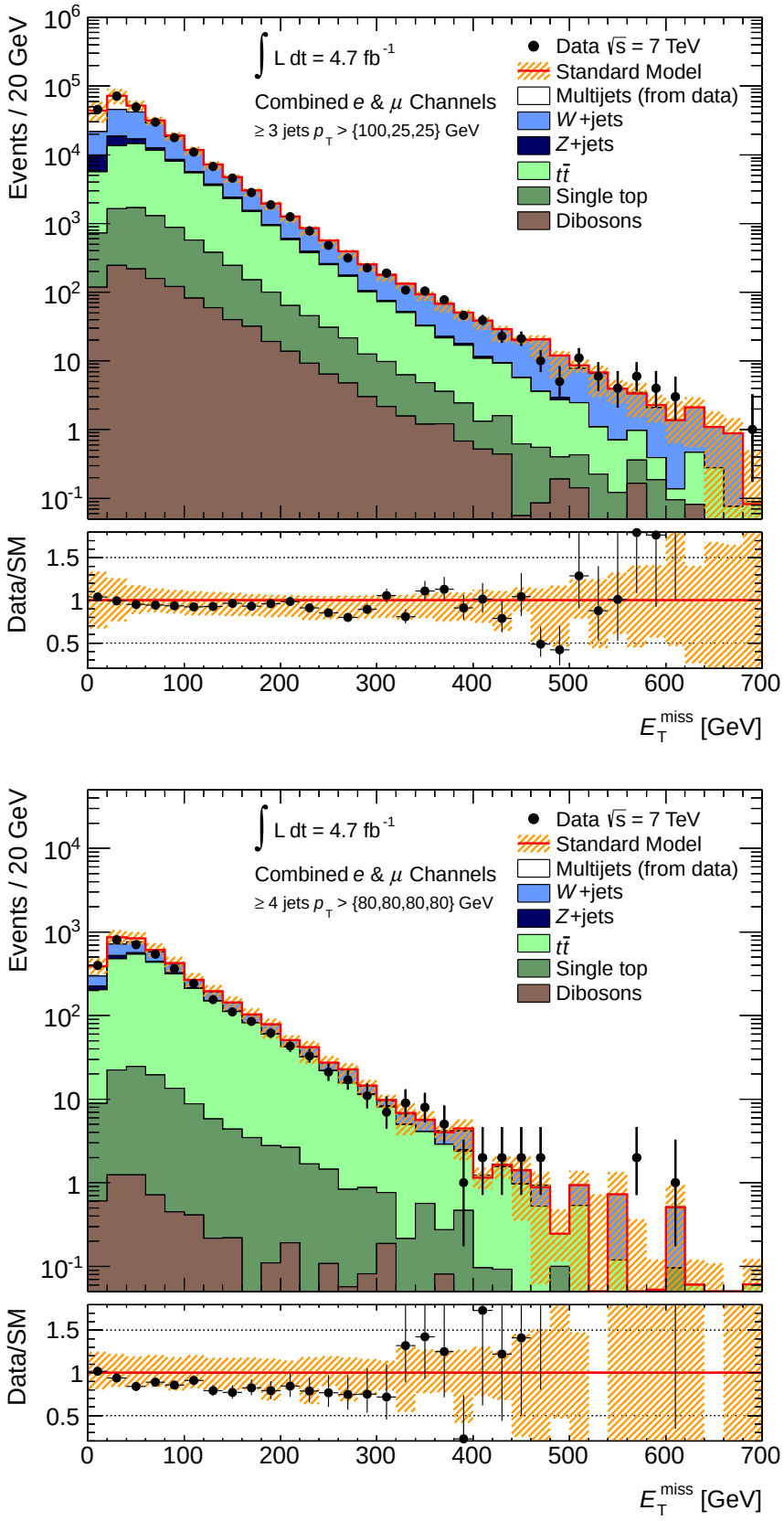

Figure 4.2: Data and MC comparisons for $E_{\mathrm{T}}^{\mathrm{miss}}$ for one lepton plus three jets (left) and one lepton plus four jets (right) selections. The hashed band shows the combined uncertainties from MC statistics, the jet energy scale and multijets background determination. These uncertainties are assumed to be fully uncorrelated.

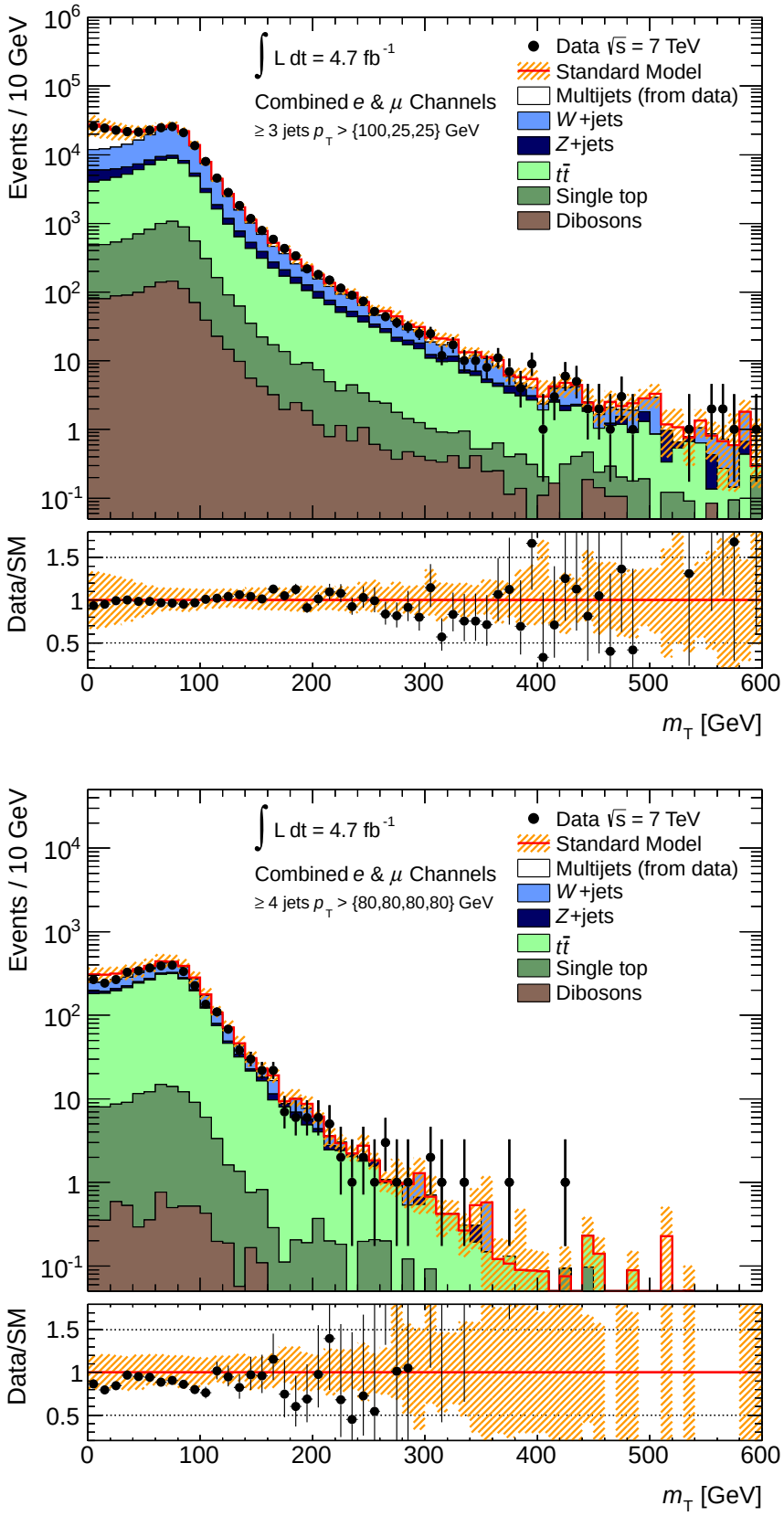

Figure 4.3: Data and MC comparisons for m_{T} for one lepton plus three jets (left) and one lepton plus four jets (right) selections. The hashed band shows the combined uncertainties from MC statistics, the jet energy scale and multijets background determination. These uncertainties are assumed to be fully uncorrelated.

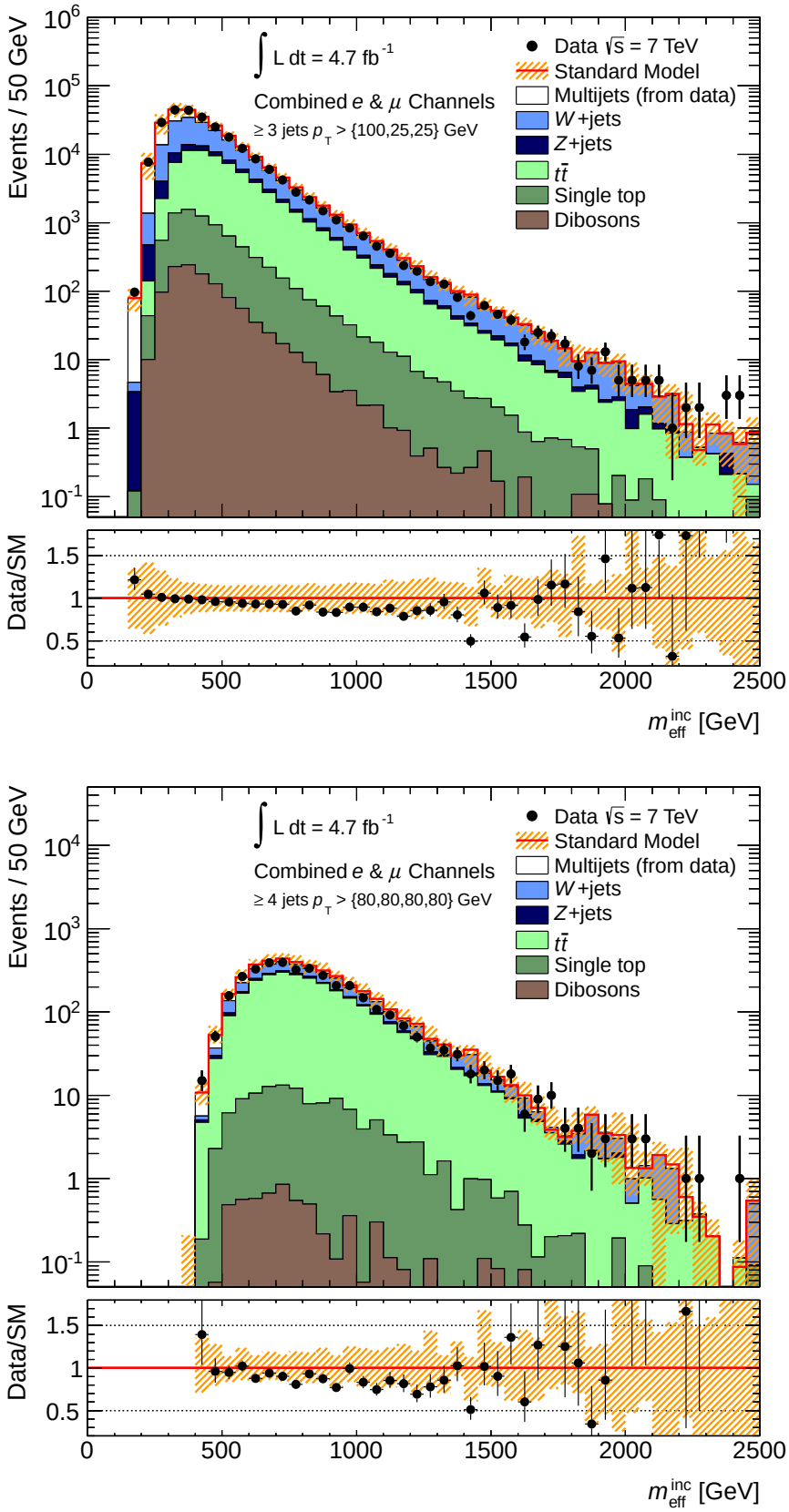

Figure 4.4: Data and MC comparisons for $m_{\text{eff}}^{\text{inc}}$ for one lepton plus three jets (left) and one lepton plus four jets (right) selections. The hashed band shows the combined uncertainties from MC statistics, the jet energy scale and multijets background determination. These uncertainties are assumed to be fully uncorrelated.

Part II

Searching for supersymmetry

Chapter 5

Search strategy

5.1 Overview

The phenomenology of SUSY is such that it may manifest itself in a variety of different ways, depending on how nature sets the value of each parameter in the theory. This means that searches for SUSY at collider experiments tend to analyse particular final states, in which SUSY-like signals would appear as deviations from the predictions of the SM. The particular analysis presented here uses signal regions with exactly one high p_{T} electron or muon[1]. This makes the analysis sensitive to decays in which the SUSY particles flow through a cascade that includes a chargino. In order to reflect the environment of the LHC, in which strong interactions dominate, it is also expected that the decay will be initiated by a squark or gluino. Therefore, jeDancer obv. ts are expected in the final state. Finally, as this analysis considers R-parity conserving SUSY, significant $E_{\mathrm{T}}^{\mathrm{miss}}$ is expected in the final state in the form of a pair of LSPs. An example of such a decay is given in Figure 5.1. Using regions in which such decays may be expected to have large rates relative to the SM allows the search to be performed by counting events in binned distributions. Deviations in these distributions from predictions without SUSY contributions may indicate the presence of signal.

[1]This thesis will generally use the term lepton to mean electron or muon, as taus are not differentiated from jets in this analysis.

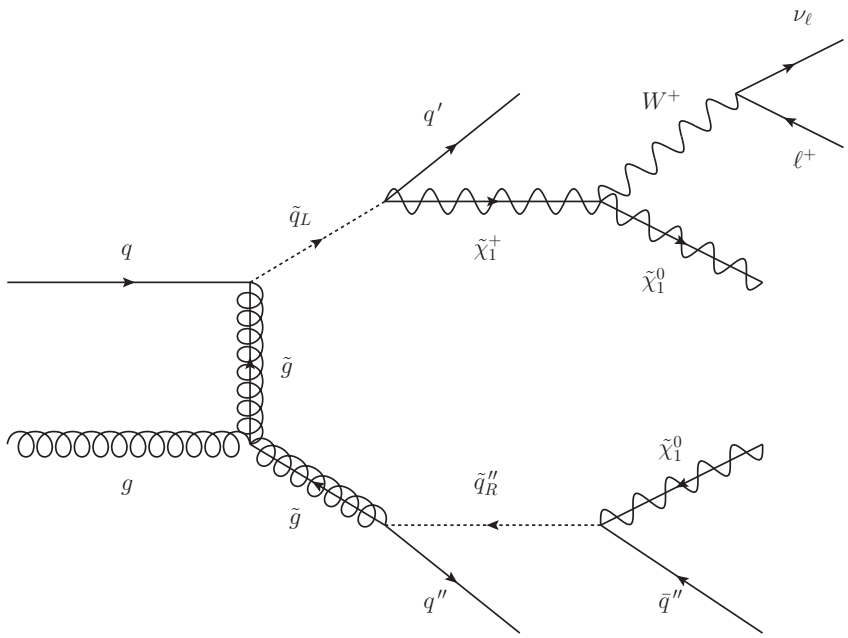

Figure 5.1: An example of a pair of SUSY cascade decays with one lepton, three jets and missing transverse momentum in the final state.

There are various SM processes that can produce similar topologies to the signal decays in this analysis. Most notably top quark pair production and W boson production in association with jets can give events that look very similar to those expected from SUSY cascades. These dominant backgrounds are determined using dedicated control samples to constrain their normalisation in MC simulations relative to the observed data. These normalisations are then extrapolated to signal enhanced regions using the shape of particular variables in MC. Additionally, the background from multijet processes, where leptons are either faked by a jet or the decay of a heavy hadron in a jet produces a high p_{T} lepton, are estimated directly from the observed data. The backgrounds from subdominant processes are taken directly from the MC prediction. The background estimation methods used in this analysis are described in detail in Chapter 6.

In order to extract the expectation of the backgrounds in signal enriched regions, a simultaneous fit is performed for all of the control and signal regions. This takes account of the dominant systematics and their affect on the extrapolation of the background normalisations. The shapes of kinematic variables are used in the control regions to better constrain the effects of systematics and shapes are also used in the signal regions to enhance the sta-

tistical power for exclusion. The statistical model constructed in this analysis is described in Chapter 7.

5.2 Signal regions

Kinematic cuts are applied to the data samples in order to discriminate events that have the characteristics of SUSY cascades from those expected to be common in the SM. The cuts used in this analysis are identical to those used in [101]. Considering the topology suggested in Figure 5.1, while maintaining reasonable selection efficiencies, results in the following selections:

High $E_{\mathrm{T}}^{\mathrm{miss}}$: In R-parity conserving SUSY scenarios, the LSP ($\tilde{\chi}_1^0$) will be stable and so carry energy away from the event, as it only interacts weakly. Similarly the neutrino produced in the decay of the chargino ($\tilde{\chi}_1^{\pm}$) through a W boson will escape the detector. A cut of $E_{\mathrm{T}}^{\mathrm{miss}} > 250$ GeV removes events that do not satisfy these criteria;

High m_{T}: Decays of top pairs and single W bosons that produce one lepton and a neutrino will tend to have m_{T} of the lepton-$E_{\mathrm{T}}^{\mathrm{miss}}$ system (defined in Equation (4.1)) close to, or below, the W mass at approximately 80 GeV. Using this information, a cut of $m_{\mathrm{T}} > 100$ GeV can be expected to remove a significant proportion of SM events corresponding to leptonic W or semi-leptonic[2] $t\bar{t}$ decays;

High $m_{\mathrm{eff}}^{\mathrm{inc}}$: As SUSY has not been observed by any previous analyses, it is expected that most of the SUSY partners will be heavy (if they exist). The decay products from a particle with high mass will tend to be produced at high p_{T}, unless the mass difference between the SUSY partners is small. In this analysis, cuts of $m_{\mathrm{eff}}^{\mathrm{inc}} > 1200$ GeV and $m_{\mathrm{eff}}^{\mathrm{inc}} > 800$ GeV are used when setting model-independent limits. In the case of specific SUSY model exclusion, the shape of $m_{\mathrm{eff}}^{\mathrm{inc}}$ is used and no explicit cut is applied. It should be noted, however, that an implicit cut on this variable is always present

[2] An event in which a $t\bar{t}$ pair decays such that one side only produces hadrons, while the other side produces a lepton, $E_{\mathrm{T}}^{\mathrm{miss}}$ and a b-jet is said to be semi-leptonic.

from the object selection detailed in Section 4.4 and any additional $E_{\mathrm{T}}^{\mathrm{miss}}$ and $p_{\mathrm{T}}^{\mathrm{jet}}$ requirements;

m_{eff} has a significant $\boldsymbol{E_{\mathrm{T}}^{\mathrm{miss}}}$ component: In order that the $E_{\mathrm{T}}^{\mathrm{miss}}$ in an event is predominantly from real sources, such as neutrinos and potentially LSPs, it is required that the $E_{\mathrm{T}}^{\mathrm{miss}}$ forms a significant fraction of the total transverse momentum in the event. Fake $E_{\mathrm{T}}^{\mathrm{miss}}$ can be produced by mis-measurement of physics objects, predominantly jets, as such mis-measurement would introduce a fake imbalance in the sum of the objects' momenta in the event. However, the effect of this mis-measurement will be greater for higher p_{T} objects. Therefore, selections of $E_{\mathrm{T}}^{\mathrm{miss}}/m_{\mathrm{eff}-3} > 0.3$ and $E_{\mathrm{T}}^{\mathrm{miss}}/m_{\mathrm{eff}-4} > 0.2$ are used to reduce the effects of these mis-measurements. Here, $m_{\mathrm{eff}-\mathrm{N}}$ is defined as

$$m_{\mathrm{eff}-\mathrm{N}} = E_{\mathrm{T}}^{\mathrm{miss}} + p_{\mathrm{T}}^{\ell} + \sum_{i}^{N} p_{\mathrm{T}}^{\mathrm{jet}_i}, \tag{5.1}$$

where N is the specific number of jets required in the selection.

Two signal regions are used to account for different topologies that have the expected properties of SUSY cascades. These signal regions correspond to selections with three jets or at least four jets and are statistically independent so that they may be combined in the simultaneous fit. The signal regions used for setting model-independent limits are called h1l3jT and h1l4jT for the three and four jet selections respectively. In this notation the T denotes a tight selection, meaning that an explicit $m_{\mathrm{eff}}^{\mathrm{inc}}$ cut has been applied. Further selections are used for exclusion, called h1l3j and h1l4j, which are equivalent to the respective tight selections, but do not apply the explicit $m_{\mathrm{eff}}^{\mathrm{inc}}$ cut. The tight selections are summarised in Table 5.1.

5.3 Signal samples

In the event that this analysis does not observe a significant signal it is possible to set limits on given models as a function of their free parameters. This is done by generating grids of signal points on which the exclusion power of the analysis can be tested on a point-by-point

Cut	h1l3jT	h1l4jT
Number of signal leptons	Exactly 1	
Number of pre-selected leptons	Exactly 1	
$E_{\mathrm{T}}^{\mathrm{miss}}$ [GeV]	> 250	
m_{T} [GeV]	> 100	
$p_{\mathrm{T}}^{\mathrm{jet}\,\{1,2,3\}}$ [GeV]	$> \{100, 25, 25\}$	$> \{80, 80, 80\}$
$p_{\mathrm{T}}^{\mathrm{jet}\,4}$ [GeV]	< 80	> 80
$E_{\mathrm{T}}^{\mathrm{miss}}/m_{\mathrm{eff-N}}$	$E_{\mathrm{T}}^{\mathrm{miss}}/m_{\mathrm{eff}-3} > 0.3$	$E_{\mathrm{T}}^{\mathrm{miss}}/m_{\mathrm{eff}-4} > 0.2$
$m_{\mathrm{eff}}^{\mathrm{inc}}$ [GeV]	> 1200	> 800

Table 5.1: The selection of the signal enriched regions used in this analysis. These correspond to tight selections, with an explicit $m_{\mathrm{eff}}^{\mathrm{inc}}$ cut. Loose selections will also be used where the explicit $m_{\mathrm{eff}}^{\mathrm{inc}}$ cut is removed. The loose selections are otherwise equivalent to the h1l3jT and h1l4jT selections, above, and are called h1l3j and h1l4j respectively.

basis. Two classes of SUSY model are tested in this analysis: the MSUGRA model, which reduces the SUSY parameter space down to five free parameters by requiring the unification of particle masses and couplings at the GUT scale; and a Simplified Model, which removes the high energy scale SUSY parameters and adds parameters corresponding to observable masses and couplings at the TeV scale.

5.3.1 Cross sections and associated uncertainties

The cross sections and relevant uncertainties associated with the SUSY signal points used in this analysis are calculated with the NLL-fast [117] interpolation tool for models where the squark and gluino masses are between 200 GeV and 2 TeV (100 GeV and 1 TeV for stop or sbottom production). Prospino 2.1 [118] is used for all other processes.

Uncertainties arising from the calculation of the cross section can be large when considering SUSY models, as the potentially high mass of the particles can probe regions of the PDFs that are not well constrained by current measurements. Therefore, two different sets of PDFs are used when determining the signal cross sections and their uncertainties. The PDFs that are used are the `CTEQ6.6` [119] and `MSTW2008` [120] sets. The factors entering the uncertainty calculation are:

Scale uncertainty: One must chose factorisation and renormalisation scales when performing calculations in QCD in order to produce convergent results. The uncertainty arising from this choice is assessed by calculating the cross section with both the renormalisation and factorisation scale set to twice and half of the mean mass of the SUSY partners produced;

PDF uncertainty: Both the `CTEQ6.6` and `MSTW2008` PDF sets provide a large number of uncertainties to cover the various experimental errors associated with the PDFs. Each uncertainty is considered in turn and found to produce either an upward or downward variation of the cross section. The uncertainty associated with the PDF is, therefore, asymmetric and has two components, PDF+ and PDF−. Each of these components is then calculated as the quadratic sum of the uncertainties that produce positive or negative variations respectively;

Strong coupling uncertainty: In order to assess the uncertainty on the value of the strong coupling (α_s) used in the cross section calculations, the `CTEQ6.6AS` [121] variations are implemented. The uncertainty on α_s is taken to be half the difference from each of the extreme variations of these parameters. Note that this uncertainty only applies to the cross sections that are calculated using the `CTEQ6.6` PDF set.

The total asymmetric uncertainties from the `CTEQ6.6` and `MSTW2008` PDF sets are then individually defined as the quadratic sum of the different associated uncertainties

$$\mathrm{CTEQ}_{+(-)} = \sqrt{\mathrm{CTEQ}^2_{\mathrm{PDF}+(-)} + \mathrm{CTEQ}^2_{\mathrm{scale}+(-)} + \mathrm{CTEQ}^2_{\alpha_s+(-)}}; \tag{5.2}$$

$$\mathrm{MSTW}_{+(-)} = \sqrt{\mathrm{MSTW}^2_{\mathrm{PDF}+(-)} + \mathrm{MSTW}^2_{\mathrm{scale}+(-)}}. \tag{5.3}$$

The total cross section and its uncertainty are then calculated by finding the maximum cross section in the positive direction (σ_+) and the minimum cross section in the negative direction (σ_-) between the two PDF sets,

$$\sigma_+ = \max[\text{CTEQ} + \text{CTEQ}_+, \text{MSTW} + \text{MSTW}_+]; \quad (5.4)$$

$$\sigma_- = \min[\text{CTEQ} - \text{CTEQ}_-, \text{MSTW} - \text{MSTW}_-]. \quad (5.5)$$

Using these, the cross section is then the mean,

$$\sigma = \frac{\sigma_+ + \sigma_-}{2}, \quad (5.6)$$

and the uncertainty on the cross section is the symmetrised deviation,

$$\Delta\sigma = \frac{\sigma_+ - \sigma_-}{\sigma_+ + \sigma_-}. \quad (5.7)$$

5.3.2 The MSUGRA grid

A common model that is used to test the exclusion power of a SUSY search is MSUGRA. This model is produced by the requirement of the minimal addition of particles to the known SM spectrum and the unification of SUSY partner masses and couplings at the GUT scale. This is performed under the gravity-mediated SUSY breaking scenario and results in five free parameters[3].

The specific model tested in this analysis has three of these parameters fixed, such that $A_0 = 0$, $\tan(\beta) = 10$ and $\mu > 0$. The choice of these values is primarily to facilitate comparisons of analyses between ATLAS and CMS, allowing both experiments to sample from the same plane in parameter space. It should also be noted that the variation of these parameters have been shown to have very small effects on the results of analyses similar to that presented in this thesis [107]. Furthermore, values of high $\tan(\beta)$ tend to affect the

[3]The free parameters in MSUGRA are: the unified scalar mass (m_0); the unified gaugino mass ($m_{1/2}$); the trilinear coupling (A_0); the ratio of the vacuum expectation values of the two Higgs doublets ($\tan\beta$); and the sign of the higgsino mass parameter (μ).

SUSY partners of the third generation of SM particles, and dedicated analyses exist to search for these scenarios.

Having set the parameters as described above the only free parameters that remain are m_0 and $m_{1/2}$. Within this space, a total of 863 points are generated with $m_0 = \{100 : 4260\}$ GeV and $m_{1/2} = \{30 : 750\}$ GeV, with between 10000 and 25000 events at each point. In order to speed up the process of generating these points only 399 points are generated with the full ATLAS simulation package [122], while 464 are generated using the `ATLFAST2.0` [123] fast simulation package. The main difference between the full and fast simulations is that the fast simulation uses a parametrised showering for the calorimeters, while the full simulation uses a full `GEANT4` [97] simulation. Therefore, the fast simulation gives a good approximation of the full simulation for most events. The distribution of the MSUGRA points across the grid can be seen on the left side of Figure 5.2.

The mass spectra and branching ratios were generated using `ISAJET7.80` [124]. Events were then generated using `HERWIG++2.4.2` [125] with the `MRST2007LO*` [126] PDF set. In order to improve the suitability of the selection used in this analysis, events that were found to contain no coloured particles were removed at event generation stage. The cross section is plotted as a function of the grid parameter space on the left side of Figure 5.3 and the distribution of the uncertainty is given on the left side of Figure 5.4.

5.3.3 The Simplified Model grid

In order to set limits on more general SUSY-like models, so called Simplified Models can be considered. These models only consider one specific decay, with 100% branching ratio, from a pair of SUSY partners. This scenario reduces the complexity of the model such that the total cross sections depend only on the masses selected for the initial particles in the decay chain. It should be noted, however, that the momenta of the SM particles that are produced in the decay can be low if the selected Simplified Model spectrum has small mass differences between the SUSY partners. In turn this can make Simplified Models a strong test case for the sensitivity of an analysis to near-degenerate spectra.

This analysis will set limits on a Simplified Model where two gluinos are produced. Each of these gluinos then decay to two jets and the lightest chargino, which is assumed to be pure Wino. The chargino then decays into a W boson and the LSP, which is assumed to be the lightest neutralino and pure Bino. All other particles are assumed to be at masses beyond the direct sensitivity of the LHC experiments[4]. This results in three free parameters in the model: the mass of the gluino; the mass of the LSP; and the mass of the chargino. In the grid considered by this analysis, the mass difference between the chargino and the LSP is precisely half of the mass difference between the gluino and the LSP. This leaves only the gluino and LSP masses as the free parameters, and points are generated in this plane as seen on the right of Figure 5.2.

Events are generated for the Simplified Model grid using `MadGraph5v1.3.27` [127], interfaced to `PYTHIA6` [98] and using the `CTEQ6L1` [61] PDF set, with an extra jet in the matrix element. In order to propagate coloured particles from the matrix element into the hadronisation processes, the MLM matching parameter is chosen to be the minimum of 50 GeV and the mass of the lightest SUSY partner in the matrix element. The cross sections as a function of gluino mass for this model are shown on the right side of Figure 5.3 and the associated uncertainties are show on the right side of Figure 5.4.

[4]The additional particle masses are set to 4.5 TeV, to be precise.

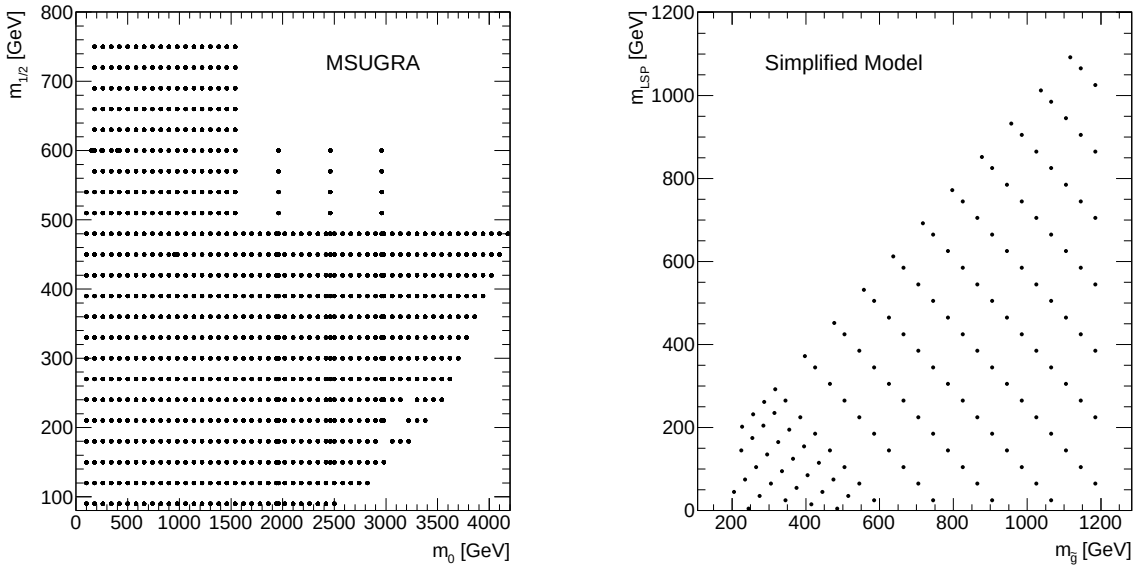

Figure 5.2: The distribution of points simulated in the MSUGRA m_0-$m_{1/2}$ plane (left) and the Simplified Model $m_{\tilde{g}}$-m_{LSP} plane (right). In the MSUGRA grid, no points are generated in the lower right region as such points do not produce EWSB. Also, the lack of points in the top left region of the MSUGRA grid is due to the production of a charged LSP.

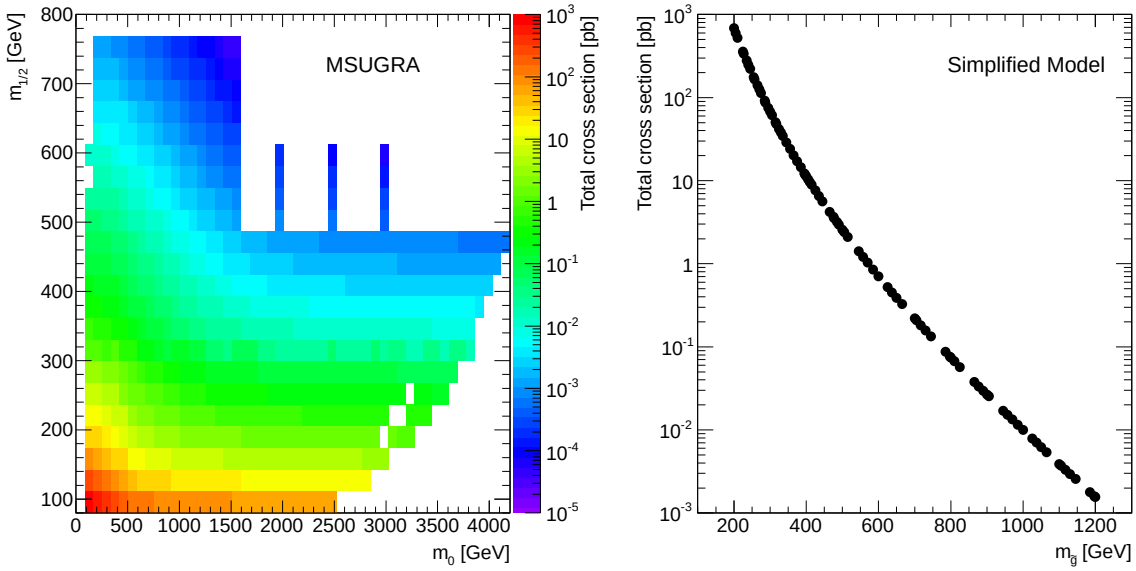

Figure 5.3: The cross section of signal points simulated in the MSUGRA m_0-$m_{1/2}$ plane (left) and the Simplified Model as a function of $m_{\tilde{g}}$ (right). In the MSUGRA grid, no points are generated in the lower right region as such points do not produce EWSB. Also, the lack of points in the top left region of the MSUGRA grid is due to the production of a charged LSP.

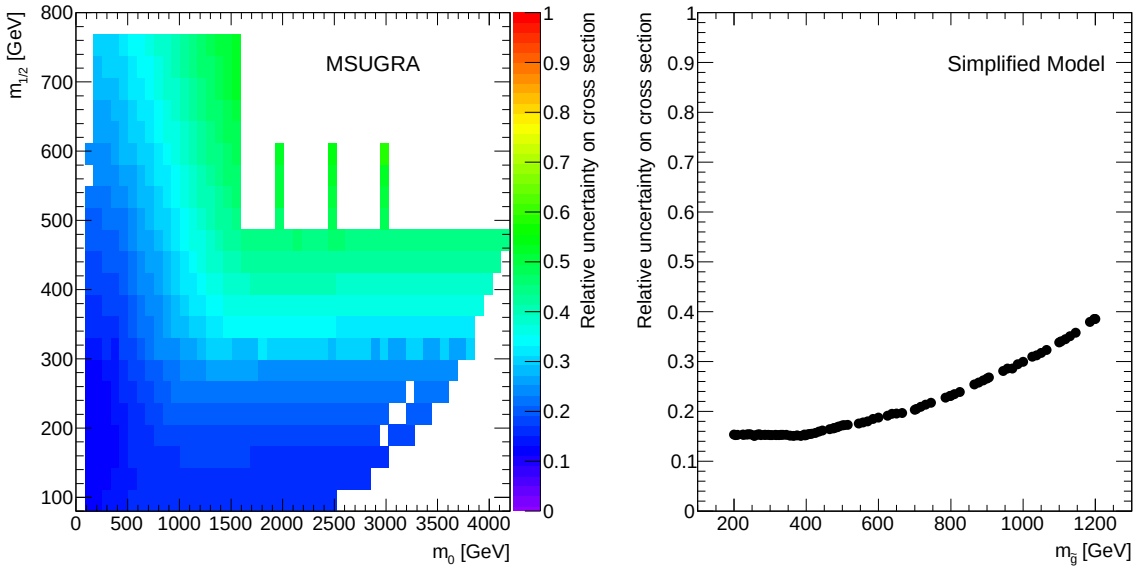

Figure 5.4: The total uncertainty on the cross section of signal points simulated in the MSUGRA m_0-$m_{1/2}$ plane (left) and the Simplified Model as a function of $m_{\tilde{g}}$ (right). In the MSUGRA grid, no points are generated in the lower right region as such points do not produce EWSB. Also, the lack of points in the top left region of the MSUGRA grid is due to the production of a charged LSP.

Chapter 6

Background determination

6.1 Multijet backgrounds and the matrix method

The QCD rate at a hadron collider is often large when compared to the rate at which the events of interest are produced. Therefore, it is impractical to generate sufficient numbers of MC events to effectively represent processes that produce multiple jets. To account for this the background contribution from such processes, which primarily include the faking of leptons by jets and the production of real leptons from the decays of heavy flavour jets, are determined using the observed data.

Two sets of events are generated, with differing lepton definitions. These datasets are labelled 'tight' and 'loose', which apply or remove the 'Isolation' criteria given in Tables 4.6 and 4.7. A further 'loose-not-tight' sample can be derived that contains the events in the loose sample that do not contribute to the tight sample.

The efficiency for fake and real leptons to pass the isolation cut (ϵ_{fake} and ϵ_{real} respectively) are then found using dedicated control samples. These efficiencies are used to determine the number of fake and real leptons that pass this cut ($N_{\text{fake}}^{\text{tight}}$ and $N_{\text{real}}^{\text{tight}}$ respectively) in some region of phase space, Ω:

$$
\begin{aligned}
N^{\,\text{tight}} &= N^{\text{tight}}_{\text{fake}} + N^{\text{tight}}_{\text{real}} \\
&= \epsilon_{\text{fake}}(\Omega) N^{\text{loose}}_{\text{fake}} + \epsilon_{\text{real}}(\Omega) N^{\text{loose}}_{\text{real}} \; ; \qquad (6.1) \\
N^{\,\text{loose-not-tight}} &= (N^{\text{loose}}_{\text{fake}} - N^{\text{tight}}_{\text{fake}}) + (N^{\text{loose}}_{\text{real}} - N^{\text{tight}}_{\text{real}}) \\
&= (1 - \epsilon_{\text{fake}}(\Omega)) N^{\text{loose}}_{\text{fake}} + (1 - \epsilon_{\text{real}}(\Omega)) N^{\text{loose}}_{\text{real}}, \qquad (6.2)
\end{aligned}
$$

where N^{tight} and $N^{\text{loose-not-tight}}$ are the total number of events in the tight and the loose-not-tight samples respectively. The efficiencies of the isolation cut for real and fake leptons are given by:

$$
\epsilon_{\text{real}} = \frac{N^{\text{tight}}_{\text{real}}}{N^{\text{loose}}_{\text{real}}}; \quad \epsilon_{\text{fake}} = \frac{N^{\text{tight}}_{\text{fake}}}{N^{\text{loose}}_{\text{fake}}}, \qquad (6.3)
$$

where $N^{\text{tight}}_{\text{real (fake)}}$ are the number of real (fake) leptons that pass the tight selection and $N^{\text{loose}}_{\text{real (fake)}}$ are the number of real (fake) leptons that pass the loose selection.

In order to determine the contamination of fake leptons in the tight lepton selection, the $N^{\text{tight}}_{\text{fake}}$ parameter must be extracted. This can be done by considering that the total number of events in the loose or tight samples is just the sum of the fake and real events in those samples. Doing so generates the following matrix equation:

$$
\begin{pmatrix} N^{\,\text{loose}} \\ N^{\,\text{tight}} \end{pmatrix} = \begin{pmatrix} 1/\epsilon_{\text{fake}} & 1/\epsilon_{\text{real}} \\ 1 & 1 \end{pmatrix} \begin{pmatrix} N^{\text{tight}}_{\text{fake}} \\ N^{\text{tight}}_{\text{real}} \end{pmatrix}. \qquad (6.4)
$$

It is now possible solve for $N^{\text{tight}}_{\text{fake}}$ by inverting the matrix in Equation (6.4) and noting that $N^{\,\text{loose}} = N^{\,\text{loose-not-tight}} + N^{\,\text{tight}}$. Solving for $N^{\text{tight}}_{\text{fake}}$ leads to:

$$
N^{\text{tight}}_{\text{fake}} = \frac{\epsilon_{\text{fake}}}{\epsilon_{\text{real}} - \epsilon_{\text{fake}}} \left(\epsilon_{\text{real}} N^{\,\text{loose-not-tight}} - (1 - \epsilon_{\text{real}}) N^{\,\text{tight}} \right). \qquad (6.5)
$$

It should be noted that this method is only valid if ϵ_{real} and ϵ_{fake} are sufficiently different, which is the case as shown in the discussion later in this Section.

Using Equation (6.5), $N_{\text{fake}}^{\text{tight}}$ can be calculated on an event-by-event basis by considering whether or not the lepton in the event passes the isolation cut. In the case that $\epsilon_{\text{real}} > \epsilon_{\text{fake}}$, which is true if the isolation cut preferentially selects real leptons rather than fakes, then an event with a lepton in the loose-not-tight selection picks up a positive weight, while an event with a lepton in the tight selection picks up a negative weight. If a boolean variable, $\delta(\text{tight})$, is defined such that it has a value of 1 for events with a tight lepton and a value of 0 for events with a loose-not-tight lepton, then these weights can be written as

$$w_{\text{fake}}^{\text{tight}} = \frac{\epsilon_{\text{fake}}}{\epsilon_{\text{real}} - \epsilon_{\text{fake}}} \left(\epsilon_{\text{real}} - \delta(\text{tight})\right). \tag{6.6}$$

The multijet contribution in each bin is established by histogramming the events in the loose sample with these weights applied.

The efficiencies required to perform these calculations are derived in separate control regions. For ϵ_{real}, a selection is applied to events in a sample enhanced in $Z \to \ell\ell$, with an $E_{\text{T}}^{\text{miss}} < 30$ GeV cut to suppress W+jets. This produces efficiencies of $\epsilon_{\text{real}}^{\text{electron}} = (88 \to 94.6)\% \pm 0.2\%$, and $\epsilon_{\text{real}}^{\text{muon}} = 97\% \pm 0.1\%$. The value of ϵ_{fake} is derived in samples with loose lepton selections where an additional jet is required in the event. The fake efficiencies are found to be $\epsilon_{\text{fake}}^{\text{electron}} = (11 \to 32)\% \pm 3\%$ and $\epsilon_{\text{fake}}^{\text{muon}} = 23\%$ with a small uncertainty. For the electron selection, an additional efficiency for events in which a b-tagged jet is present is derived. The values of these efficiencies are provided in the package [128], which also gives methods that can be used to derive the event-by-event weights. More information on the matrix method can be found in [102] and [104].

Uncertainties on this method are taken in two parts: the statistical uncertainty from the size of the loose sample; and the systematic uncertainty, which includes information on the accuracy to which the efficiencies can be determined. The statistical uncertainty is defined as the sum of the squares of the weights for a given bin, whereas the systematic uncertainty

can be found by propagating the uncertainties on the efficiencies through Equation (6.6).

The distributions of the number of jets with $p_{\mathrm{T}} > 25$ GeV, for a selection with at least one jet with $p_{\mathrm{T}} > 50$ GeV, $E_{\mathrm{T}}^{\mathrm{miss}} < 30$ GeV and $m_{\mathrm{T}} < 40$ GeV in the electron and muon channels are shown in Figure 6.1. These cuts are used to select a region that is expected to be enhanced in multijet events compared to the other backgrounds. From these it can be seen that the multijets determination technique provides a good agreement, within uncertainties, between expectation and observation for this particular selection.

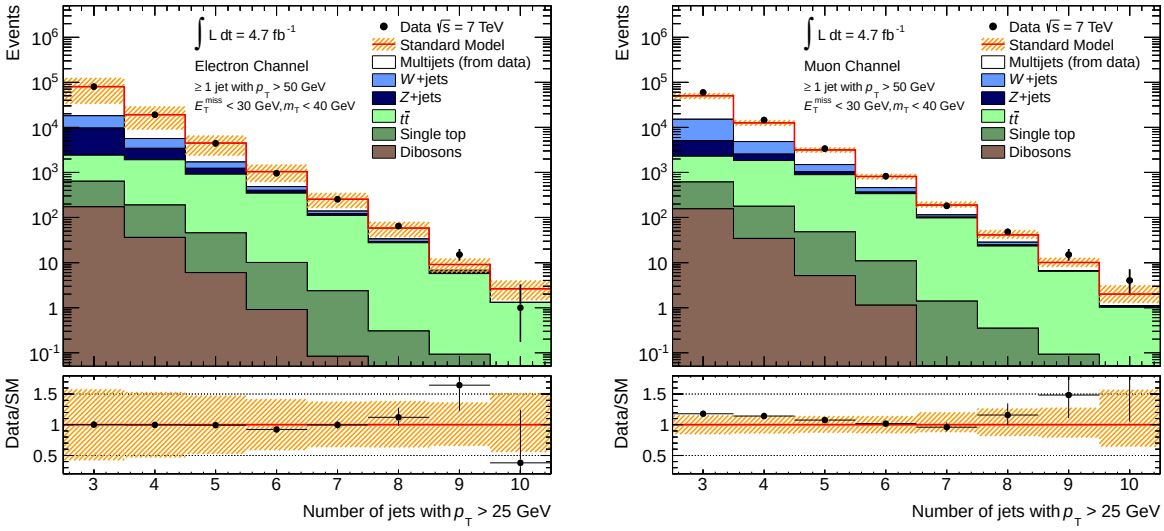

Figure 6.1: The distributions of the number of jets with $p_{\mathrm{T}} > 25$ GeV for a selection requiring at least one jet with $p_{\mathrm{T}} > 50$ GeV, $E_{\mathrm{T}}^{\mathrm{miss}} < 30$ GeV and $m_{\mathrm{T}} < 40$ GeV in the electron (left) and muon (right) channels. The hashed band shows the combined uncertainties from MC statistics, the jet energy scale and the multijets background determination. These uncertainties are assumed to be fully uncorrelated.

6.2 Dominant electroweak backgrounds

The search for SUSY in this analysis is designed to select events where a lepton is produced in a decay chain with jets and significant $E_{\mathrm{T}}^{\mathrm{miss}}$. The highest cross section processes that satisfy these criteria, which are the dominant backgrounds to the search, are the production of W+jets and top pairs ($t\bar{t}$). Both of these can have topologies that are very similar to the desired SUSY signal either by leptonic W decays, semi-leptonic $t\bar{t}$ decays or fully leptonic $t\bar{t}$ decays where one lepton is not identified. Examples of such topologies are shown in

Figure 6.2. These can be compared to the example signal topology given in Figure 5.1.

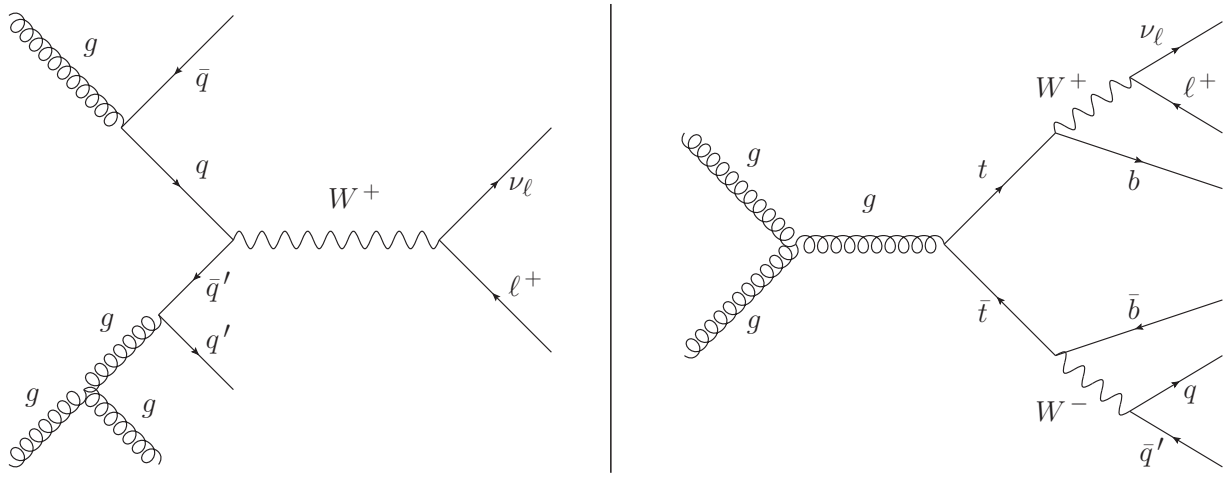

Figure 6.2: Example Feynman diagrams for the production of a leptonically decaying W boson in association with jets (left) and semi-leptonic top pair production (right).

The total rates of these processes are much lower than those that produce multijets. This means that it is feasible to produce sufficient numbers of MC events to represent the expectation in data. However, in order to reduce some contributions from detector effects, such as the luminosity uncertainty, and to reduce the amount to which the analysis relies on cross sections derived from theory, the normalisations of these samples are taken from a pair of control regions and extrapolated to the signal regions. This also, potentially, allows various uncertainties to be constrained by constructing the statistical model as outlined in Chapter 7. In order to make use of this feature, the number of jets with $p_{\mathrm{T}} > 25$ GeV is chosen as the discriminating shape. This jet counting distribution is particularly sensitive to the separation of `Alpgen` MC samples into individual numbers of partons and so can be expected to constrain uncertainties from theory relating to this, which are described in Section 4.7.

The control region selection criteria for the W+jets enhanced region (WR) and the $t\bar{t}$ enhanced region (TR) are given in Table 6.1, and are the same as those used in [101]. The lower cuts on $E_{\mathrm{T}}^{\mathrm{miss}}$ and m_{T} remove a large proportion of the multijet background, while the upper cuts aim to prevent significant contamination from potential signals. This effectively results in a selection close to the peak of the $m_{\mathrm{T}}(W)$ distribution. The $m_{\mathrm{eff}}^{\mathrm{inc}}$ and jet cuts are used to select a region of phase space that is close to the signal regions, in terms of the

overall energy scale of the event. A b-tagged jet requirement is used to separate the two control regions, as $t\bar{t}$ will generally be produced with two b-jets, and the rate for W+b-jets is small compared to that of inclusive W+jets production.

Cut	**WR**	**TR**
Number of signal leptons	Exactly 1	
Number of pre-selected leptons	Exactly 1	
Number of signal jets	At least 3	
$p_{\mathrm{T}}^{\mathrm{jet}}$ [GeV]	$> \{80, 25, 25\}$	
m_{T} [GeV]	$40 < m_{\mathrm{T}} < 80$	
$E_{\mathrm{T}}^{\mathrm{miss}}$ [GeV]	$30 < E_{\mathrm{T}}^{\mathrm{miss}} < 120$	
$m_{\mathrm{eff}}^{\mathrm{inc}}$ [GeV]	> 400	
Number of b-tagged jets in 3 highest p_{T} jets	Exactly 0	At least 1

Table 6.1: The selection of the W+jets and $t\bar{t}$ enhanced control regions (WR and TR respectively) used in this analysis. Note that all cuts are common to the two regions apart from the b-tagging requirements.

The distributions of the number of b-tagged jets in the three highest p_{T} jets with the combined WR and TR selection for the electron and muon channels are shown in Figure 6.3. Note that the bin with zero b-tagged jets is expected to be dominated by W+jets events, while the bins with one or more b-tagged jets are expected to predominantly contain $t\bar{t}$ events.

6.3 Sub-dominant backgrounds

The additional, sub-dominant, backgrounds that are considered in this analysis, namely the production of Z+jets, single tops and dibosons, are taken directly from their respective MC. This means that they are not constrained in the fitting procedure and their normalisations are propagated to all control and signal regions directly.

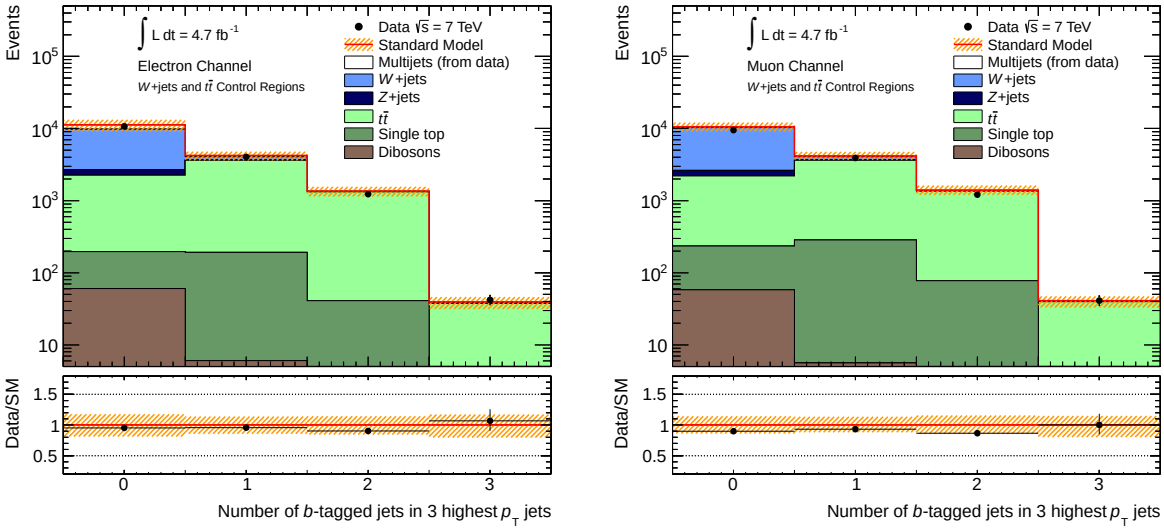

Figure 6.3: The distributions of the number of b-tagged jets in the three highest p_{T} jets for the combined W+jets and $t\bar{t}$ selections in the electron (left) and muon (right) channels. The hashed band shows the combined uncertainties from MC statistics, the jet energy scale and the multijets background determination. These uncertainties are assumed to be fully uncorrelated.

Chapter 7

Constructing the statistical model

7.1 Introduction

Many analyses in particle physics wish to extract either a measurement of, or a limit on, the strength of some signal. In particular, searches for signs of new physics, such as SUSY, require comparisons to be made between predictions of rates expected from SM processes and the observed data. Particular signal scenarios can also be tested by including predictions from those scenarios in the statistical model. This poses three important questions:

1. How should the statistical model be constructed?
2. Are the data consistent with a particular theoretical model of new physics?
3. What limits can be set on the rates of any new theoretical model?

The first question will be addressed in this Section, while the tools required to answer the latter two are covered in Appendices A.3 and A.4, respectively.

Most SUSY searches to date have constructed models based on the number of events passing a set of cuts, for example [104]. Such analyses use background enhanced regions to constrain the cross section of particular SM processes and then extrapolate these rates to a background depleted (but potentially signal enhanced) region.

The analysis presented here builds on those ideas, but constructs the statistical model in a very different manner. Rather than just counting events passing particular cuts, this analysis constructs histograms for a particular observable in that cut region. Each histogram bin can be thought of as a counting experiment, but the use of histograms allows more information to be included in the statistical model. In principle, this allows the uncertainties on certain parameters of the statistical model, the inputs to which are either provided by groups studying the performance of the detector or by theorists, to be measured as part of the analysis.

Much of the following is described in detail in [129], but the essential points for building the model are interpreted here. The notation is defined such that Roman characters correspond to observable quantities, while Greek characters correspond to parameters of the statistical model.

7.2 The HistFitter framework

To facilitate the construction of the statistical model, this analysis uses the `HistFitter` [130] framework, the development of which was a major focus of my work. The model itself is built using `HistFactory` [129], which is part of the `RooStats` [131] package. `HistFitter` provides a means to generate the histograms that are fed into `HistFactory`, in an easily configured way, and implements statistical tests on the resulting model.

The `HistFitter` framework provides three major extensions to `HistFactory`:

- Firstly, it is possible to use `ROOT` [132] `TTree` objects as inputs. These objects store event data in a set of branches for each event. This makes it possible to apply a series of cuts directly to these branches, rather than having to iterate over the data and apply the cuts to each event. In applying cuts directly to the branches the calculation time required to populate the necessary histograms is greatly reduced, compared to iterative methods. Therefore, users can apply cuts that represent the final stages of analysis, such as the definition of control and signal regions, without producing prohibitive

computational times. This in turn allows the user to easily test the application of their new statistical model on their dataset, with appropriate blinding criteria satisfied. The execution speed is further increased by tracking the histograms that have already been generated, so as not to waste CPU time re-generating unnecessary data;

- Secondly, the XML files that are used by HistFactory to set up the statistical model are written within HistFitter, based on the users input configuration. These XML files can be reasonably long and complex, in general, and the design of HistFitter attempts to offset the details of these XML files by interpretting a configuration file, written in Python. The use of a flexible object-oriented language, such as Python, means that the code can interpret the objects that the user defines in their configuration as the neccessary XML sequences without the user needing detailed knowledge of the XML itself. Furthermore, during the analysis of the user's configuration, it is possible to further manipulate the data, such as to perform normalisations and extract floating point values relating the relative scales of different histograms;
- Thirdly, it provides a simple integration with the statistical analysis tools within RooStats. The TWorkspace object that is produced as the output of HistFactory contains detailed information about the statistical model that the user has constructed. This information must then be passed on to calculation tools in order to extract explicit information regarding the limits that can be set on the signal strength within the statistical model, values that quantify the agreement with various hypotheses that are to be tested, and so on. HistFitter is directly integrated with such calculation tools, using C++, and allows the user to extract the desired quantified statistical information from their model without having to implement their own analysis framework or to pass their model into an additional tool.

As mentioned above, the usage of HistFitter requires the user to write a configuration file in Python. This uses a set of classes that are provided within HistFitter that are both designed to approximately mirror the XML schema in HistFactory and perform the necessary manipulations to the data such as to produce the desired histograms and to extract the

information required to populate the XML files. This is all managed by a singleton class that tracks the histograms that have already been generated, so as not to duplicate CPU effort, and which provides general controls that configure the general properties of the statistical model, such as what information to initially setup the system to produce the histograms, and communicate with the other Python objects as well as mediating the interface with the C++ components.

The objects required to build a configuration file use a class heirarchy structure, down which information is passed when a new object is added to the statistical model:

- The top level class is TopLevelXML, instances of which can be thought of as interchangeable with the statistical model itself. For example, a TopLevelXML object will represent the background-only hypothesis;
- The next level down is the Measurement class. This provides information like the parameter of interest to use, if any constraint terms or parameters are to be treated in special ways. The Measurement object can be thought of as defining specific settings for the statistical model, which may change for different measurements, in general;
- The third level is the ChannelXML class. This is the point at which the grouping of parameters in the following Sections becomes apparent. A ChannelXML object will represent, for example, a control or signal region and will then contain all of the remaining information to define that channel, or region;
- Next is the Sample class. This is where the operations are performed to configure how the histograms should be populated for a given sample;
- The Sample class also allows the application of Systematics objects, instances of the lowest class in the heirarchy and definitions of the different systematics types.

The heirarchy method is very useful for constructing less verbose configuration files. For example, a list of common samples may be added to the TopLevelXML object and their effect will be applied to all ChannelXML objects that are known to that TopLevelXML object. It is also possible to add objects at any level at any time, so a Sample may be added to a

`ChannelXML` that is already known to a `TopLevelXML` object, but that `Sample` would only be known to the `ChannelXML` to which it had been assigned. Another useful feature is that objects can be cloned. This is particularly useful for `TopLevelXML` objects, as a representation of a common background-only statistical model can be constructed and then cloned. The properties necessary to define other statistical models, such as a model-independent statistical model, can then be added to the new `TopLevelXML` without having to start again with adding all of the common definitions.

It is hoped that the details of the information that the user must enter into their configuration is relatively intuitive and represents the statistical model in terms of properties that Physicists will tend to be familiar with, such as systematics, control regions, signal regions, and so forth. Once the user has constructed their statistical model within the configuration file, `HistFitter` is then run by entering a single command line statement, with various inputs that determine which calculations to perform, such as limit setting and hypothesis testing, allowing all of the analysis stages from control and signal region population to analysis of the statistical model to be performed in one step. In addition to these features, `HistFitter` can be easily modified to be executed on multiple CPU cores, for example in a batch farm, by defining scripts that execute the model using unique sets of signal points. This can also help to speed up the analysis for the user, particularly when processing large grids of signal points, as is common in SUSY analyses.

7.3 Event counting and histograms

Let us begin the process of building a statistical model by considering a most basic counting experiment, with one bin for the entire analysis and background expectations that are known to perfect accuracy. First we will define a set of samples, $s \in \{\text{sig}, \text{bkg}_1, ...\}$, representing each of the expected background processes and the signal model that is being tested. Each sample then has a nominal expected event count (ν_s). The expected event yield for all background processes is fixed in the statistical model if we assume that all backgrounds present in the

data are accounted for and known exactly. However, the number of signal events in the observed data is not known a priori and so must be allowed to float in the statistical model. This freedom is included by introducing the signal strength (μ) which gives the yield of the signal sample in question relative to the theoretically predicted number of events. Using the information that we have so far, we can write the expected number of events for the signal plus background model as

$$\nu = \mu\nu_{\text{sig}} + \sum_{s\neq\text{sig}} \nu_s. \tag{7.1}$$

To extend the single bin analysis to an analysis that makes use of a histogram, let us introduce a set of bins, $b \in \{\text{bin}_1, ...\}$. In this notation, the expected histogram is

$$\nu^b = \mu\nu^b_{\text{sig}} + \sum_{s\neq\text{sig}} \nu^b_s. \tag{7.2}$$

Now that we have defined our statistical model, we can start to think of how the data will relate to our expectation. If we only consider a single distribution, producing a particular observed histogram (n^b), then we must find the probability density function (pdf) of our statistical model. A common choice for the pdf for counting experiments is the Poisson distribution[1]. This choice is generally made for analyses that expect a fairly low event count and for which the probability for an event to occur is low. Such a situation is characterised by the law of rare events, where a large number of trials are used but the probability of any trial giving the desired outcome is small, resulting in an intermediate number of expected events. In this case the Poisson distribution can actually be considered as a limiting case of the binomial distribution. The Poisson distribution is used in this case rather than the binomial as it has a simpler function form and only requires knowledge of the expected number of events, rather than the number of trials and the probability of a trial being a success as is required when using the binomial distribution. To save space, the Poisson distribution is

[1]The Poisson distribution is defined such that, for an expected number of events ν, the probability of observing n events is $\mathcal{P}(n\,|\nu) = \frac{\nu^n e^{-\nu}}{n!}$.

abbreviated to Pois($n\,|\nu$).

When considering a model with multiple bins, we have to account for the fact that the probability of observing a particular histogram is conditional on all of the bins having particular values. Therefore, the resulting probability for observing a particular histogram n^b in our current model, given that we expect the histogram ν^b, is the product of the probabilities of observing the particular count for each bin

$$\mathcal{P}\left(n^b|\mu\right) = \prod_b \text{Pois}\left(n^b|\nu^b\right) = \prod_b \text{Pois}\left(n^b \middle| \mu\nu^b_{\text{sig}} + \sum_{s\neq\text{sig}} \nu^b_{\text{s}}\right). \tag{7.3}$$

7.4 Adding uncertainties

So far we have a model with only one free parameter, μ. In reality, we will not know the nominal statistical model perfectly - there will be uncertainties originating from various sources. Therefore, we must add further parameters to the model to account for these uncertainties.

Certain parameters are constrained by previous measurements, which means that they are free to float but are bounded by some pdf so that the statistical model is penalised if a constrained parameter moves too far from its expectation. Measurements of calibrations and efficiencies, as well as theoretical predictions, are known as 'sources' and have such constraints. A particular experiment will measure the values of sources as auxiliary measurements, $a \in \{a_i, ..., a_N\}$, with some uncertainty. However, the experiment is only run once, and future experiments may observe different values of those auxiliary measurements. Therefore, the true mean values of the sources, $\alpha \in \{\alpha_1, ..., \alpha_N\}$, are not known a priori and they must be extracted from the statistical model. If enough information is included in the statistical model, then the data can be used to constrain the true value of each α and its uncertainty (Δ_α).

Other parameters are 'unconstrained', and are allowed to float freely (within some pre-

defined range).

The types of parameters used in this model are:

NormFactor: These are unconstrained normalisations of the MC samples, denoted $\phi_s(\alpha)$, relative to the number of events in the input nominal model. The signal strength, μ, is a special case of such a parameter;

Luminosity: The luminosity, λ_s, enters the fit with a Gaussian constraint for any sample that is normalised according to the direct theoretical predictions. In the case of the nominal fit configuration, this is only the case for the signal sample. For other samples, the nominal measured luminosity, L_0 is used;

OverallSys: These parameters correspond to an overall shift up or down in the normalisation of the given histogram, with the symbol $\eta_s(\alpha)$. An ambiguity is immediately evident in this situation - when the value of α is changed, what values should η take? This is solved by defining an interpolation procedure, which says that if α is shifted within the constraint term, then this is propagated into the value of η by defining two exponential distributions, one in the positive direction from $\alpha = 0$ and one in the negative direction. The values of η are fixed at $\alpha = \pm 1$ according to the relative normalisations calculated from the input histograms, and then the appropriate value of η can be found for any intermediate value of α;

HistoSys: These parameters correspond to systematics that have an effect on the shape and overall normalisation of the histogram of interest, and are denoted $\sigma_{sb}(\alpha)$. The input in this case is a pair of histograms that represent the distribution at one standard deviation of the source from nominal. There is now a situation where an interpolation must be used between the nominal and shifted histograms. This is performed by a bin-by-bin piecewise linear interpolation, where two straight lines are used to extract the values of $\sigma_{sb}(\alpha)$ on either side of the nominal value. Only one value of α is used across all of the bins, as each systematic is represented by a single constraint, but each bin may have a larger or smaller deviation at $\alpha = \pm 1$ than its neighbour. Therefore the shape of the histogram is allowed to change, or 'morph' in this process;

NormHistoSys: As a HistoSys, but normalised according to the ratio between the total number of events in the statistical model for the shifted histogram to the number of events in the nominal histogram. In this way the component of uncertainty that affects the overall cross section that the statistical model is sensitive to is factored out and included in the normalisation parameters;

ShapeSys: Some parameters in the model will need to be constrained with bin-by-bin scale factors, $\gamma_b(\alpha)$. In this case, a constraint parameter is defined for each bin. The distribution is therefore allowed to morph but in an independent manner for each bin. This removes any additional information that may allow the associated systematic to be changed within the model. An example of such an effect is the uncertainty due to the MC statistics. These are constrained by either Poisson or Gaussian distributions.

Generally, parameters of the types HistoSys and OverallSys are correlated either between all samples, as is the case for experimental uncertainties, or between sub-sets of the samples, for some theoretical uncertainties.

We can now extend Equation (7.2) to find the expected histogram with all uncertainty parameters included,

$$\nu_b(\phi, \alpha) = \sum_s \lambda_s \; \gamma_b(\alpha) \; \phi_s \; \eta_s(\alpha) \; \sigma_{sb}(\alpha). \tag{7.4}$$

We must also modify Equation (7.3) to account for the effect of the uncertainty parameters. Now that we have parameters that quantify the uncertainties on various sources, we are concerned with the probability of observing a given histogram in data and a set of auxiliary measurements, given the sets of unconstrained and constrained parameters in the model,

$$\mathcal{P}(n_b, a|\phi, \alpha) = \prod_b \text{Pois}(n_b|\nu_b) \; G(L_0|\lambda, \Delta_L) \; \prod_i P_i(a_i|\alpha_i). \tag{7.5}$$

Where P_i defines the distribution used to constrain α_i.

7.5 Multiple channels

This analysis intends to take information from control and signal regions. Therefore, the model must be adapted further to account for measurements in multiple channels, $c \in \{\text{chan}_1, ...\}$. The final set of expected histograms is then given by

$$\nu_{cb}(\phi, \alpha) = \sum_s \lambda_{cs}\ \gamma_{cb}(\alpha)\ \phi_s\ \eta_{cs}(\alpha)\ \sigma_{csb}(\alpha), \tag{7.6}$$

and the probability of observing a set of histograms in a set of channels is

$$\mathcal{P}(n_{cb}, a|\phi, \alpha) = \prod_c \prod_{b \in b_c} \text{Pois}(n_{cb}|\nu_{cb})\ G(L_0|\lambda, \Delta_L)\ \prod_i P_i(a_i|\alpha_i), \tag{7.7}$$

where b_c corresponds to the bins of the distribution characterising channel c.

Note that in the same way that some uncertainties are correlated across samples, it is also possible to correlate parameters across channels. This is of particular importance for the NormFactors affecting the W+jets and $t\bar{t}$ samples as the normalisation is fitted simultaneously in the relevant control regions. Therefore, the expected normalisations are extracted while taking into account various uncertainties, the cross contamination between W+jets and $t\bar{t}$ in the two regions and the contamination from other samples. Furthermore, if the signal regions are included in the simultaneous fit, then these background normalisation values can be used to constrain the signal strength, μ.

7.6 Nominal model configuration

Now that we have the tools in place to construct an arbitrary model for a multi-channel shape fit, we can apply this to the one-lepton SUSY search. In this we will have separate normalisations for all of the SM processes considered, as well as the signal, and parameters defined for the experimental and theoretical uncertainties discussed in Sections 4.6 and 4.7.

The configuration of the nominal statistical model is described in Table 7.1. Note that the uncertainty on the jet energy scale is treated as a ShapeSys as the methods used to estimate this uncertainty contain implicit correlations, which may be unphysically manipulated if the uncertainty was treated as a HistoSys.

We should also define the histograms that will be used to constrain the statistical model in the control and signal regions:

- For the control regions (WR and TR) the number of jets with $p_{\mathrm{T}} > 25$ GeV will be used. For both of these selections the histograms will use unit binning and count events with jet counts of 3 through 9. Events which fall in the overflow of this distribution will not be considered.
- For the loose signal regions (h1l3j and h1l4j) the $m_{\mathrm{eff}}^{\mathrm{inc}}$ distribution will be used. In the case of h1l3j, the histogram used will have six bins covering the range $400 < m_{\mathrm{eff}}^{\mathrm{inc}}\ [\mathrm{GeV}] < 1600$, with the final bin also containing events that fall into the overflow. For h1l4j, the histogram used will have four bins covering the range $800 < m_{\mathrm{eff}}^{\mathrm{inc}}\ [\mathrm{GeV}] < 1600$, with the final bin also containing events that fall into the overflow.

Using the information above, relating to how the necessary nominal histograms should be constructed, and the information in Table 7.1, which defines how to treat the different parameters in the model, an appropriate configuration can be built for input into `HistFitter`. An outline of the `HistFitter` configuration files was given in Section 7.2.

Parameter	Type	Samples	Channels	Constant?
Signal normalisation	NormFactor	Signal	All	No
W+jets normalisation	NormFactor	W+jets	All	No
$t\bar{t}$ normalisation	NormFactor	$t\bar{t}$	All	No
Z+jets normalisation	NormFactor	Z+jets	All	Yes
Single top normalisation	NormFactor	Single top	All	Yes
Dibosons normalisation	NormFactor	Dibosons	All	Yes
Jet energy scale	ShapeSys	All	—	No
MC and multijets statistics	ShapeSys	All	—	No
W+jets k_{T} scale	NormHistoSys	W+jets	All	No
$t\bar{t}$ k_{T} scale	NormHistoSys	$t\bar{t}$	All	No
W+jets $p_{\mathrm{T}}^{\mathrm{min}}$	NormHistoSys	W+jets	CR, SR	No
$t\bar{t}$ $p_{\mathrm{T}}^{\mathrm{min}}$	NormHistoSys	$t\bar{t}$	CR, SR	No
Multijets systematic	HistoSys	Multijets	All	No
p_{T}^{W} reweighting	HistoSys	W+jets	All	No
$E_{\mathrm{T}}^{\mathrm{miss}}$ cell-out	HistoSys	All	All	No
$E_{\mathrm{T}}^{\mathrm{miss}}$ pileup	OverallSys	All	All	No
Electron energy scale	OverallSys	All	All	No
Electron energy resolution	OverallSys	All	All	No
Muon ID resolution	OverallSys	All	All	No
Muon MS resolution	OverallSys	All	All	No
Trigger efficiency	OverallSys	All	All	No
Lepton efficiency	OverallSys	All	All	No
b-tagging efficiency	OverallSys	All	WR & TR	No
Signal cross section	OverallSys	Signal	All	No
Initial state radiation	OverallSys	Signal	All	No

Table 7.1: The parameter settings in the nominal fit configuration. Note that ShapeSys cannot be shared between channels as it forms one independent parameter for each bin in the statistical model. The $p_{\mathrm{T}}^{\mathrm{min}}$ parameters are implemented in each of the CR and SR independently.

Chapter 8

Results

8.1 Background-only fit

In order to test the ability of the analysis to constrain the parameters in the model, a background-only fit is performed, according to the procedures laid out in Appendix A.1. This uses the W+jets and $t\bar{t}$ control regions, defined in Table 6.1, to isolate the corresponding processes. A simultaneous fit to both of these regions is performed to extract the relative normalisation of the W+jets and $t\bar{t}$ samples in data relative to their expected normalisation from MC. Furthermore, this fit is performed using the number of jets with $p_{\mathrm{T}} > 25$ GeV in these regions, which adds information to the fit that can potentially be used to constrain uncertainties in the model using the observed data.

After the fit has been performed in the control regions, the resulting values for the parameters in the model are projected on to other, statistically independent regions of phase space. If these regions are selected such that the signal contamination is expected to be rather small, they can be used to check that the extracted parameters are valid in general, rather than forcing the parameters in one region alone. This is important to allow the result to be validated, and as such are referred to as validation regions, which are described in Table 8.1. These attempt to produce selections that are dominated by W+jets or $t\bar{t}$ events while being closer in phase space to the signal regions than the control regions. This is

performed by looking at similar selections to the control regions but with high $E_{\mathrm{T}}^{\mathrm{miss}}$. An additional selection is used to check the extrapolation of the control regions to high m_{T}.

Cut	**WVR**	**TVR**	**HMTVR**
Number of signal leptons	Exactly 1		
Number of pre-selected leptons	Exactly 1		
Number of signal jets	At least 3		
$p_{\mathrm{T}}^{\mathrm{jet}}$ [GeV]	$> \{80, 25, 25\}$		
$m_{\mathrm{eff}}^{\mathrm{inc}}$ [GeV]	> 400		
m_{T} [GeV]	$40 < m_{\mathrm{T}} < 80$		> 80
$E_{\mathrm{T}}^{\mathrm{miss}}$ [GeV]	$120 < E_{\mathrm{T}}^{\mathrm{miss}} < 250$		$30 < E_{\mathrm{T}}^{\mathrm{miss}} < 250$
Number of b-tagged jets in 3 highest p_{T} jets	Exactly 0	At least 1	—

Table 8.1: The selection of the W+jets, $t\bar{t}$ and high m_{T} validation regions (WVR, TVR and HMTVR respectively) used in this analysis.

The final stage of the background-only fit involves projecting the parameters that have been constrained in the control regions on to the signal regions, as defined in Table 5.1. Clearly this should only be performed once a finalised model configuration has been obtained as it is at this stage that the first signs of a signal may be expected to revealed.

The complete background-only fit result and correlation matrix are given in Appendix B.1.

8.1.1 Constraining parameters in control regions

The resulting event yields for the individual background processes in the control regions can be seen in Table 8.2 and the number of jets with $p_{\mathrm{T}} > 25$ GeV in the WR and TR can also be seen in Figure 8.1. Note that the expected yield of both W+jets and $t\bar{t}$ events have been decreased by the fit, relative to the MC input. One should take care when considering these numbers as it is not only the normalisation factors that affect the yields, the effect of all of the parameters in the model must be considered. In particular, correlations between different parameters mean that the uncertainty on the yields for individual samples may be different from the uncertainty on the overall expected yield.

Selection	**WR**	**TR**
Observed events	20187	10427
Fitted total SM events	20188.70 ± 190.71	10425.76 ± 130.86
Fitted $t\bar{t}$ events	3829.30 ± 687.55	8395.17 ± 521.00
Fitted W+jets events	13501.99 ± 1363.45	916.14 ± 231.87
Fitted Z+jets events	824.95 ± 82.95	46.55 ± 8.62
Fitted diboson events	119.14 ± 12.89	14.53 ± 1.85
Fitted single top events	320.53 ± 42.36	579.85 ± 46.33
Fitted multijets events	1592.79 ± 1287.59	473.52 ± 468.05
Expected SM events before fit	22182.28	10977.90
MC $t\bar{t}$ events	4424.76	9038.14
MC W+jets events	14807.29	915.73
MC Z+jets events	835.96	43.18
MC diboson events	120.92	13.59
MC single top events	337.30	560.73
Data-driven multijets events	1656.06	406.53

Table 8.2: SM background yields in the WR and TR control regions. Nominal MC expectations (normalised to MC cross-sections) are given for comparison. The errors shown are the statistical plus systematic uncertainties.

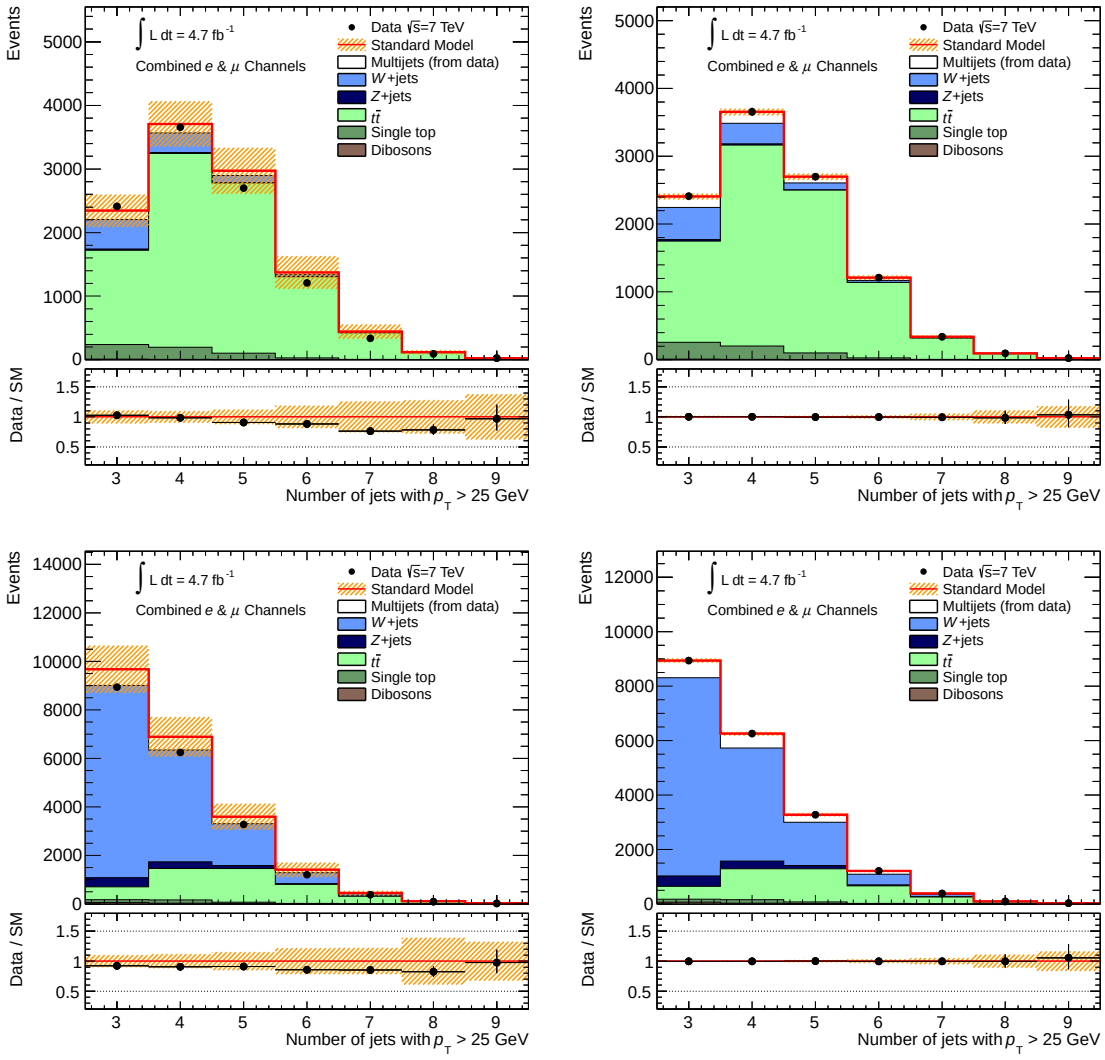

Figure 8.1: The distribution of the number of jets with $p_{\mathrm{T}} > 25$ GeV in the $t\bar{t}$ (top) and W+jets control regions before (left) and after (right) the background-only fit has been performed.

8.1.2 Checking the fit in validation regions

Using the fit result obtained in the previous Section a series of cross checks were performed to assess the accuracy of the fit in additional regions of phase space before studying the signal regions. This was done by projecting the fit result onto the regions listed in Table 8.1. The resulting expected yields from the fit for each sample in each validation region can be seen in Table 8.3. These show that, even for measurements taken in statistically independent regions from those used to constrain the fit, good agreement between the fitted yield and the yield in the observed data is obtained.

This analysis also relies on the extrapolation of the result over variable shapes, so further cross checks were made that the shapes of certain kinematic variables were also correctly estimated in these validation regions. The distributions of $E_{\mathrm{T}}^{\mathrm{miss}}$ in the WVL1 and TVL1 regions and m_{T} in the HMTV1 can be seen in Figure 8.2. These show good agreement in all distributions after the fit, when the size of the errors on the background estimate are considered.

Selection	**WVL1**	**TVL1**	**HMTVL1**
Observed events	5208	2413	34451
Fitted total SM events	5168.34 ± 1115.10	2547.27 ± 311.78	33811.55 ± 4206.86
Fitted $t\bar{t}$ events	1187.77 ± 247.07	2125.54 ± 283.38	13541.30 ± 1732.62
Fitted W+jets events	3727.77 ± 1033.75	220.85 ± 65.38	15891.19 ± 3114.68
Fitted Z+jets events	54.81 ± 5.95	2.82 ± 0.52	1327.53 ± 82.37
Fitted diboson events	63.92 ± 7.22	7.13 ± 1.13	172.74 ± 11.18
Fitted single top events	118.74 ± 16.62	177.24 ± 18.67	1001.29 ± 61.31
Fitted multijets events	15.33 ± 85.00	13.69 ± 52.42	1877.51 ± 2111.29
Expected SM events before fit	5626.28	2678.48	36484.42
MC $t\bar{t}$ events	1344.70	2255.24	14897.32
MC W+jets events	4024.07	226.11	17207.99
MC Z+jets events	55.00	2.68	1326.98
MC diboson events	64.21	6.85	172.57
MC single top events	122.97	173.91	1002.06
Data-driven multijets events	15.33	13.69	1877.51

Table 8.3: SM background yields in the WVL1, TVL1 and HMTVL1 validation regions. Nominal MC expectations (normalised to MC cross-sections) are given for comparison. The errors shown are the statistical plus systematic uncertainties.

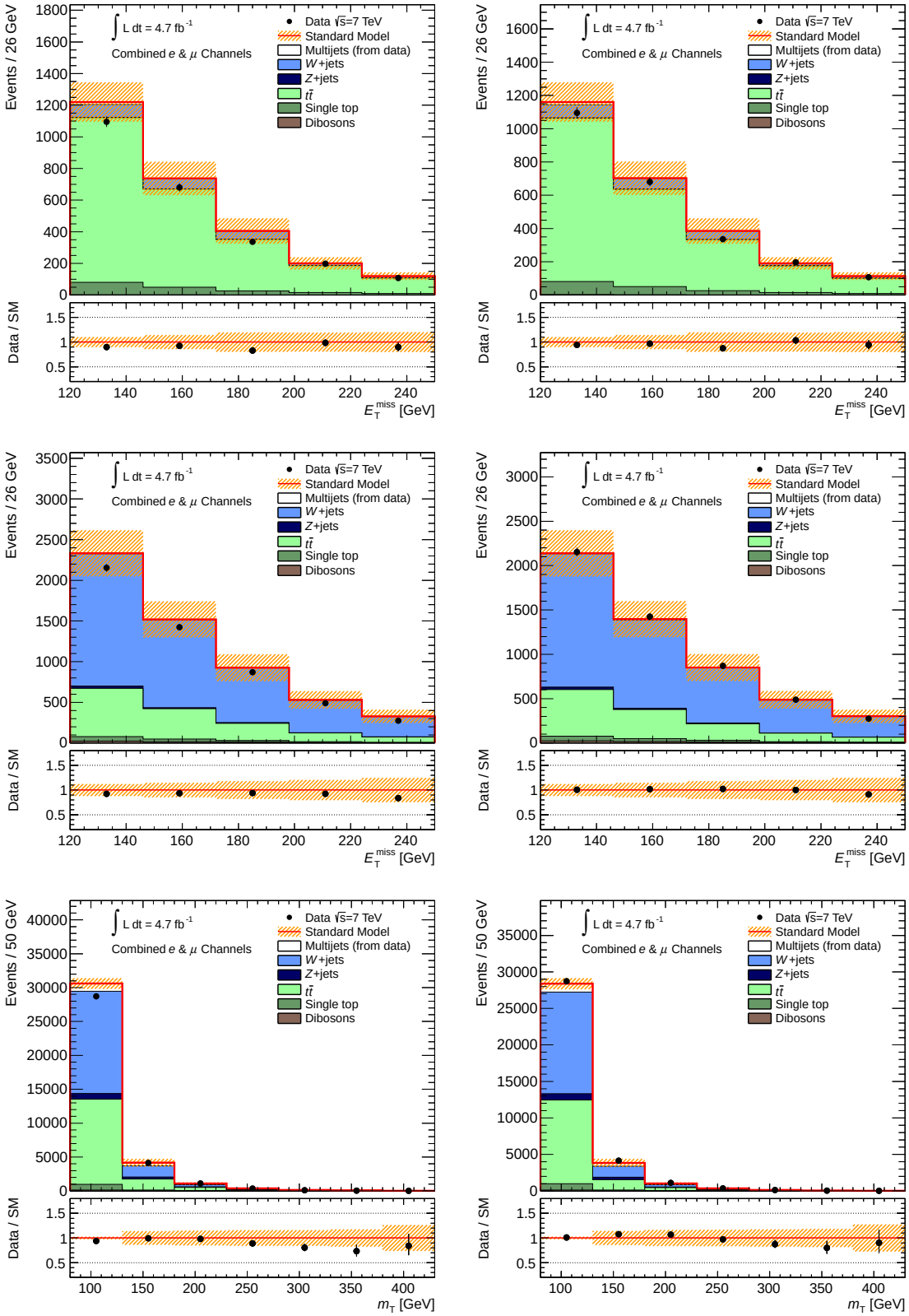

Figure 8.2: The distribution of the number of jets with $p_{\mathrm{T}} > 25$ GeV in the $t\bar{t}$ (top), W+jets (middle) and high m_{T} validation regions before (left) and after (right) the background-only fit has been performed.

8.1.3 Searching for new physics in signal regions

With a fit that is under control and validated, we can now look into the signal regions to search for potential signs of new physics. This is done, initially, by treating the signal region in the same manner as the validation regions in the previous Section. In doing this, the parameters that are constrained in the control regions are projected onto the signal regions and the fitted event yields are extracted for the SM processes. These yields are shown in Table 8.4. By comparing the fitted total SM yield with the observed yields in all of the loose and tight signal regions, it is clear that there are no significant excesses seen by this analysis. Indeed, all signal regions predict greater event yields than are observed. However, the size of the total error on the background expectation is large and the observed yields are consistent with the expected yields to within one standard deviation. It is also interesting to note that, while the h1l4j and h1l4jT regions have similar fitted SM yields, the error is smaller for h1l4j which is likely to be because this region uses shape information while h1l4jT only considers the overall yield.

To check that the $m_{\text{eff}}^{\text{inc}}$ shape is well determined in the signal regions, the distributions of $m_{\text{eff}}^{\text{inc}}$ are shown in the two loose signal regions in Figure 8.3. In both cases the agreement between the expectation and observation is improved after the fit. However, it should be noted that for these results no fitting is performed in the signal regions, only extrapolation of model parameters. Therefore, we can conclude that, given the measurements of the dominant background processes in the control regions, there is no discrepant signal shape in this analysis.

The dominant systematic uncertainties in the signal regions are shown before and after the fit in Appendix C.

Selection	**h1l3j**	**h1l4j**	**h1l3jT**	**h1l4jT**
Observed events	82	6	3	6
Fitted total SM events	91.68 ± 20.40	7.25 ± 1.87	5.06 ± 1.89	7.14 ± 2.59
Fitted $t\bar{t}$ events	40.15 ± 8.74	4.75 ± 1.37	1.37 ± 0.52	4.75 ± 1.86
Fitted W+jets events	40.59 ± 15.63	1.52 ± 0.52	2.51 ± 1.19	1.52 ± 0.62
Fitted Z+jets events	0.41 ± 0.08	0.00 ± 0.00	0.09 ± 0.03	0.00 ± 0.00
Fitted diboson events	3.25 ± 0.40	0.11 ± 0.03	0.33 ± 0.11	0.11 ± 0.04
Fitted single top events	5.10 ± 0.59	0.58 ± 0.14	0.48 ± 0.17	0.58 ± 0.20
Fitted multijets events	2.19 ± 3.12	0.29 ± 0.35	0.29 ± 0.37	0.17 ± 0.30
Expected SM events before fit	102.21	8.21	5.52	8.10
MC $t\bar{t}$ events	47.57	5.58	1.63	5.58
MC W+jets events	43.70	1.66	2.71	1.66
MC Z+jets events	0.41	0.00	0.09	0.00
MC diboson events	3.25	0.11	0.33	0.11
MC single top events	5.10	0.58	0.48	0.58
Data-driven multijets events	2.19	0.29	0.29	0.17

Table 8.4: SM background yields in the h1l3j, h1l4j, h1l3jT and h1l4jT signal regions. Nominal MC expectations (normalised to MC cross-sections) are given for comparison. The errors shown are the statistical plus systematic uncertainties.

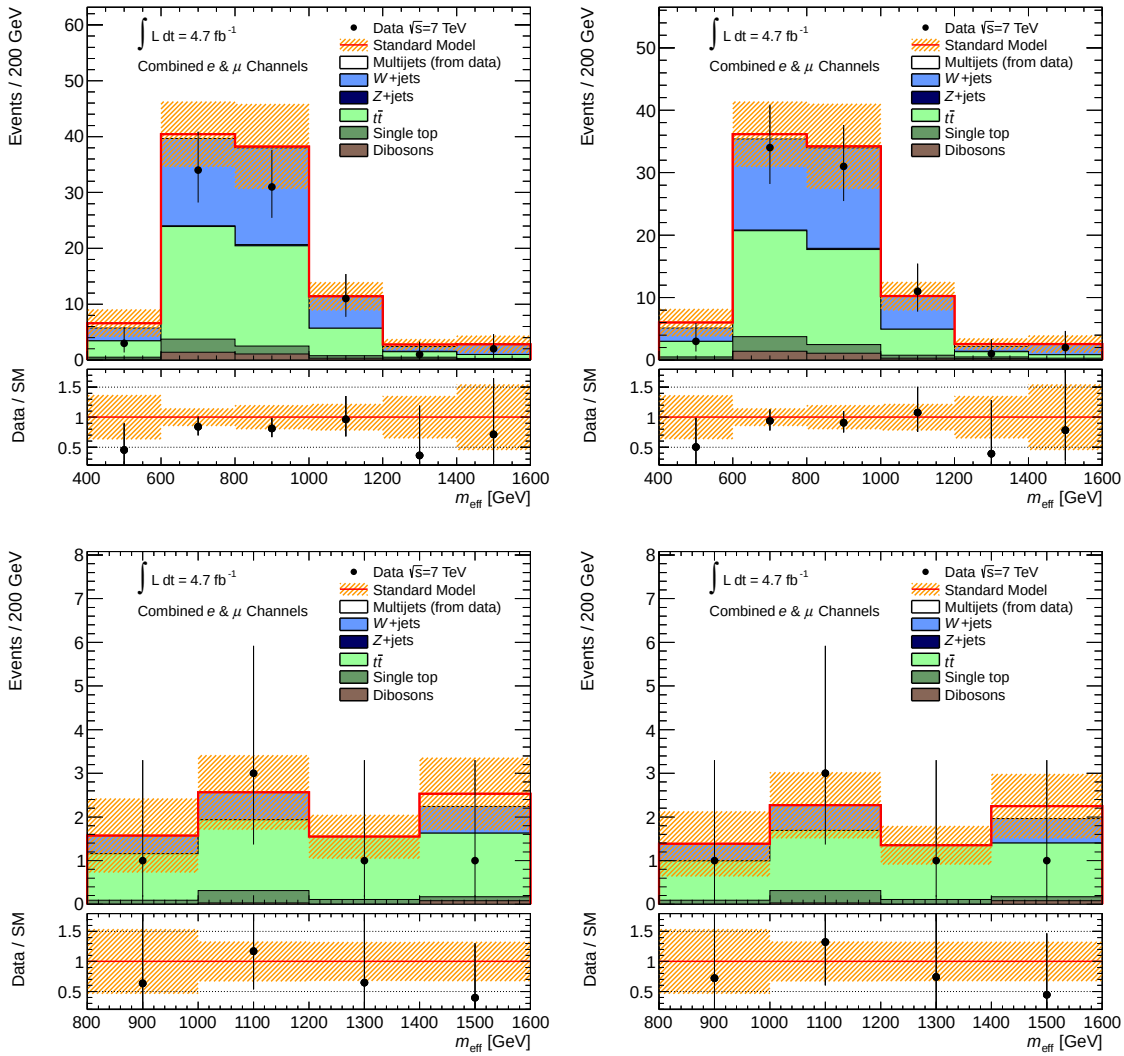

Figure 8.3: The $m_{\text{eff}}^{\text{inc}}$ distribution in the h1l3j (top) and h1l4j (bottom) signal regions before (left) and after (right) the background-only fit has been performed.

8.2 Setting model independent limits

Now that the yields in all of the control, validation and signal regions have been checked, and no signal found, we can investigate the properties of the signals that may still be present in the analysis, but statistically hidden. This is first performed in a model independent manner, according to Appendix A.4. A series of hypothesis tests are performed on a dummy signal, implanted as a single event in the tight signal regions (h1l3jT and h1l4jT). These hypothesis tests are evaluated under the CL_s metric, which is defined as the ratio of the signal plus background p-value to the background-only p-value. This choice penalises scenarios to which the analysis has little sensitivity, and so prevents such points from being excluded through statistical fluctuations. The strength of this dummy signal is allowed to fluctuate over a range that crosses the 95% CL_s limit. Therefore, the point at which the signal strength crosses this limit is the maximum number of events that are still allowed from any theoretical model in that region (at the 95% CL_s confidence level).

The results of these scans are shown in Figure 8.4. One can interpret these graphs such that any point on the CL_s line that falls below 0.05 is excluded with 95% confidence level according to CL_s. The green and yellow bands give, respectively, the one and two standard deviation uncertainty bands on the CL_s value. Therefore the width of the bands across the 0.05 p-value line give the one and two standard deviation uncertainties on the CL_s 95% confidence level exclusion.

The values of these 95% confidence level results are shown in Table 8.5. In generating these results 5000 MC toys were produced per each signal strength value that was tested. The interpretation of these limits in terms of a 95% confidence level limit on the efficiency times cross section ($\epsilon\sigma$) for any possible theoretical model is also given. Here the efficiency is defined as the fraction of the total cross section of a process to which the given signal region is sensitive. The values on the table mean that any model with an $\epsilon\sigma$ value greater than about 1 fb^{-1} would be excluded at the 95% confidence level by this analysis.

The fit result and correlation matrix for this model configuration are given in Ap-

pendix B.2.

In order to compare general results with those presented in this thesis, a sample of efficiencies for the MSUGRA grid are provided in Table 8.6. The statistical uncertainty on each measurement and the uncertainty from the jet energy scale are also shown for comparison. Note that the tight signal regions are used in this Section, and the resulting exclusion may not be comparable with the results presented in the next Section.

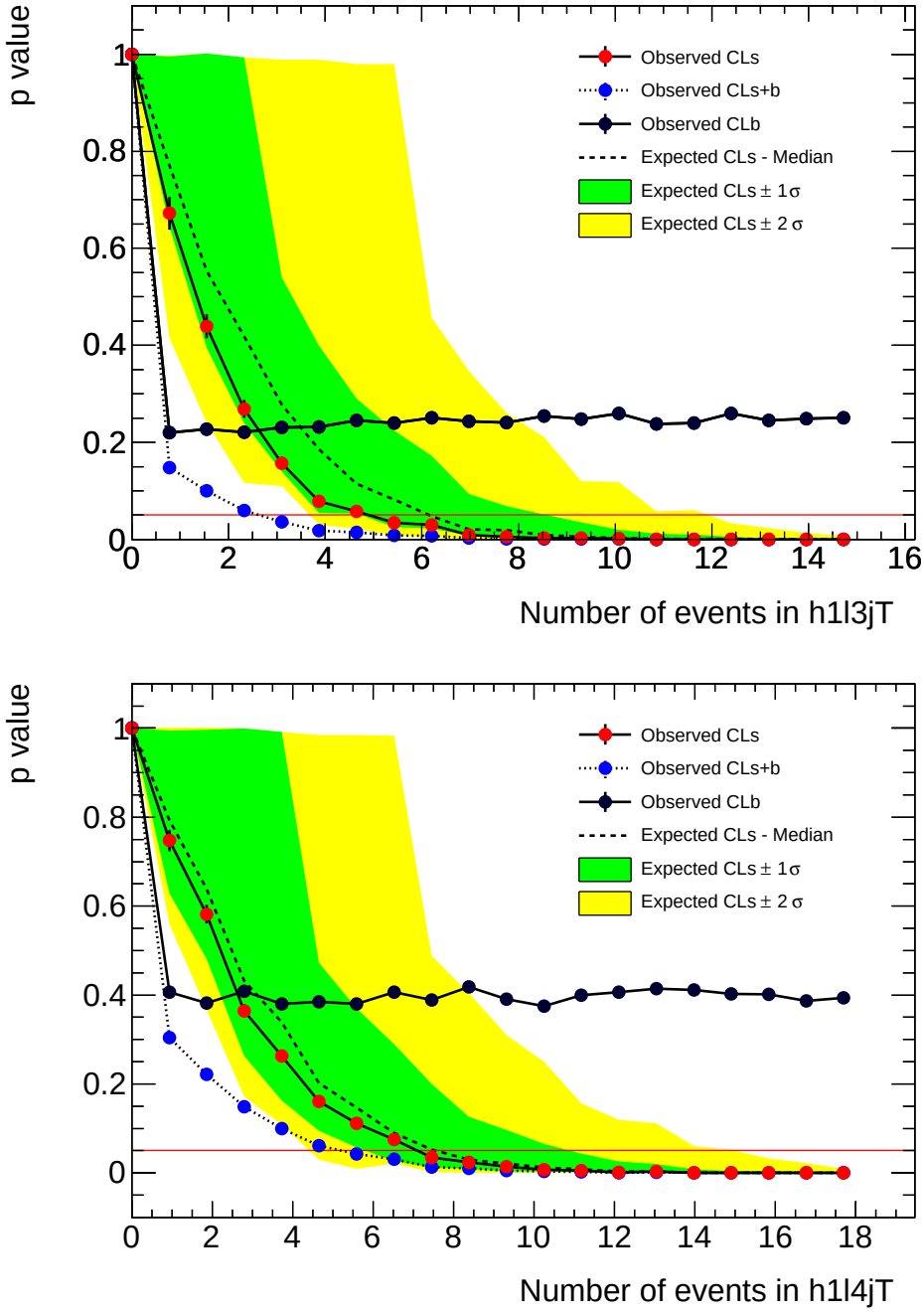

Figure 8.4: The distribution of p-values for the CL_s, CL_{s+b} and CL_b hypotheses in the h1l3jT (top) and h1l4jT (bottom) signal regions. In order to avoid false exclusion of models with low expected signal event yields, the CL_s value is considered for model independent exclusion. All signal yield values where the points lie below the 0.05 line (red) are excluded at 95% confidence level.

Signal channel	$\langle\epsilon\sigma\rangle^{95}_{\rm obs}$[fb]	$S^{95}_{\rm obs}$	$S^{95}_{\rm exp}$
h1l3jT	1.04	4.89	$6.14^{+2.45}_{-1.40}$
h1l4jT	1.51	7.10	$7.57^{+3.33}_{-1.74}$

Table 8.5: 95% CL upper limits on the visible cross-section ($\langle\epsilon\sigma\rangle^{95}_{\rm obs}$) and on the observed ($S^{95}_{\rm obs}$) and expected ($S^{95}_{\rm exp}$) number of signal events for the various signal regions.

m_0 [GeV]	$m_{1/2}$ [GeV]	ϵ(h1l3jT)	ϵ(h1l4jT)	σ [fb]
340	300	$0.0074 \pm 0.0009 \pm 0.0010$	$0.0107 \pm 0.0010 \pm 0.0022$	1150
340	540	$0.0184 \pm 0.0014 \pm 0.0010$	$0.0230 \pm 0.0015 \pm 0.0023$	21.8
1060	420	$0.0102 \pm 0.0010 \pm 0.0004$	$0.0515 \pm 0.0023 \pm 0.0031$	18.5
1860	480	$0.0109 \pm 0.0010 \pm 0.0005$	$0.0538 \pm 0.0023 \pm 0.0035$	1.51
2580	420	$0.0022 \pm 0.0004 \pm 0.0007$	$0.0098 \pm 0.0010 \pm 0.0019$	225

Table 8.6: The efficiencies and cross sections for a selection of points from the MSUGRA grid. The error on the efficiency is shown as the statistical uncertainty and the systematic uncertainty on the jet energy scale.

8.3 Exclusion fit

Tests were also performed on specific SUSY models using grids of signal points, according to the procedures given in Appendix A.3. A hypothesis test is performed at each point on the grid to extract the CL_s value and uncertainty bands. For these tests, the signal strength is fixed to unit value, as the cross section of the point being tested is known. Therefore, each signal point corresponds to a single central CL_s value and its standard deviation in the positive and negative directions. Any given point is excluded at 95% confidence level if $CL_s < 0.05$. Lines are then drawn on the grid to represent the region of excluded points and the range of the boundary of that region corresponding to a shift of one standard deviation on the CL_s value. This can be interpretted as any point lying within the boundary of the central value being excluded at least at 95% confidence level, while any point outside this curve is not excluded. The same arguements apply for the uncertainty range. These results are produced using the asymptotic approximation.

An example fit result and correlation matrix for the MSUGRA model point with $m_0 =$ 580 GeV and $m_{1/2} = 240$ GeV is show in Appendix B.3.

8.3.1 The MSUGRA plane

The first specific model that will be tested is MSUGRA, which was described in 5.3.2, and the CL_s exclusion grid is shown in Figure 8.5. This shows an observed exclusion which is at consistently higher masses compared to the expected exclusion, which corresponds to the under-fluctuations in data compared to expectations as observed in Table 8.4. In terms of model parameters, for $m_{1/2} < 300$ GeV points with $m_0 < 3500$ GeV are excluded, while for $m_0 < 800$ GeV points with $m_{1/2} < 500$ GeV are excluded. This corresponds to exclusions of squark masses below about 1100 GeV and gluino masses below about 800 GeV. For equal squark and gluino masses, points with masses below about 1200 GeV are excluded. Theoretical limits are reached corresponding to a charged LSP at low m_0 and high $m_{1/2}$, and a the failure to break electroweak symmetry at high m_0 and low $m_{1/2}$.

8.3.2 The Simplified Model plane

A Simplified Model has also been studied in this analysis, and was described in Section 5.3.3. As this grid is represented by a parametrised model, in the sense that the cross sections are determined by the measurable quantities rather than some underlying physics, it is also of interest to study the sensitivity of the analysis to a floating cross section at each point. This, along with the 95% confidence level CL_s exclusion contours are shown in Figure 8.6.

The colour gradient represents the cross section at each point that would be excluded if it could float, much in the same way as the model independent limits were derived in Section 8.2. From this it can be seen that very low cross sections, down to 20 fb, are excluded in the bulk of the grid while the cross section must be higher in order to be excluded in regions where the gluino mass becomes close to the LSP mass, where the excluded cross section rises towards 100 pb. It should be noted that the generated cross sections fall quickly as a function of gluino mass, as was shown in Figure 5.3.

In terms of the exclusion contour, gluino masses out to just beyond 900 GeV are excluded at the 95% confidence level, for low LSP masses. In such scenarios, the phase space available for the decay products is larger than cases there the LSP mass and the gluino mass are similar. Therefore the decay products will be produced with more kinetic energy, and so higher transverse momentum. The analysis presented here applies high p_{T} cuts to the selected objects and so is most sensitive to these scenarios with large mass differences. Theoretical scenarios with small mass differences would tend to result in final states with low p_{T} objects, for which the efficiency of this analysis is small. Therefore, this analysis has little sensitivity close to the diagonal where $m_{\tilde{g}} \sim m_{\mathrm{LSP}}$.

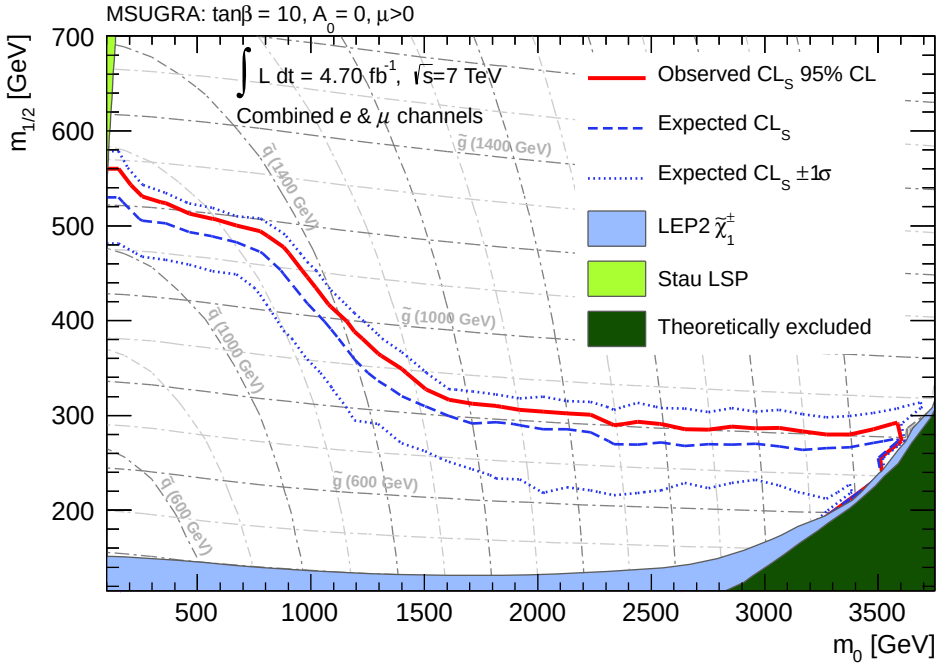

Figure 8.5: The exclusion grid for MSUGRA produced by this analysis. Theoretical exclusion at high m_0 and low $m_{1/2}$ is due to a failure to break electroweak symmetry, while at low m_0 and high $m_{1/2}$ a charged LSP is produced [133]. The direct chargino search from LEP [134] is also shown.

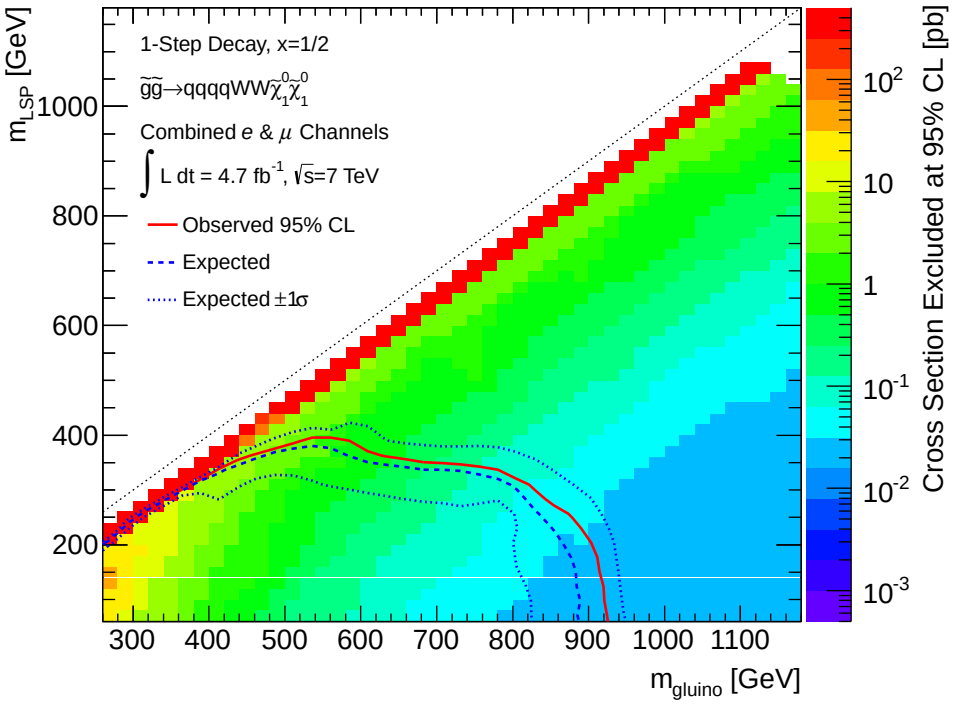

Figure 8.6: The exclusion grid for the Simplified Model produced by this analysis. The contours show the CL_s 95% confidence level exclusion, while the colour gradient shows the cross section that would be excluded by the analysis at that particular point, at the 95% confidence level.

8.4 Improvements due to statistical treatment

Now that the main results of this analysis have been obtained using the statistical model described in Chapter 7, it is instructive to see what effect the construction of this model has on the analysis. This can be done by building similar statistical models, but without the constraints from kinematic shapes in particular selections. Two of such less sophisticated statistical models are considered: the first uses single bins in all of the control and signal regions; the second uses the nominal (binned) control regions, with constraints from the number of jets with $p_{\mathrm{T}} > 25$ GeV, but keeps a single bin for each of the signal regions. The resulting normalisations of the different samples in the fit for the MSUGRA SUSY model point with $m_0 = 580$ GeV and $m_{1/2} = 240$ GeV are shown in Table 8.7.

From Table 8.7 it can be seen that the nominal configuration gives the most precise measurement for all of the unconstrained normalisations by up to a factor of two. The signal normalisation is improved when moving from the single bin signal regions, while the background normalisations are improved when the single bin control regions are replaced with kinematic constraints. Throughout this process the central value of all of the normalisation parameters remain consistent, within errors. It is important to note that the measurement of the background normalisations is not affected by the choice of a binned or shape-dependent signal region.

Normalisation	**Single bin CR & SR**	**Single bin SR**	**Nominal**
Signal	$0.0 \pm 4.1 \times 10^{-2}$	$0.0 \pm 4.8 \times 10^{-2}$	$0.0 \pm 2.6 \times 10^{-2}$
W+jets	$8.6 \times 10^{-1} \pm 3.1 \times 10^{-1}$	$9.1 \times 10^{-1} \pm 1.8 \times 10^{-1}$	$9.1 \times 10^{-1} \pm 1.8 \times 10^{-1}$
$t\bar{t}$	$9.2 \times 10^{-1} \pm 1.9 \times 10^{-1}$	$9.1 \times 10^{-1} \pm 1.0 \times 10^{-1}$	$9.1 \times 10^{-1} \pm 1.0 \times 10^{-1}$

Table 8.7: Comparison of the resulting normalisation parameters for different statistical model configurations, defined in the text. The values are shown for a simultaneous fit to the control and signal regions with the MSUGRA theoretical model point with $m_0 = 580$ GeV and $m_{1/2} = 240$ GeV.

Part III

Supplementary studies

Chapter 9

Pileup in the ATLAS detector

9.1 Pileup at the LHC

The LHC is the highest luminosity hadron collider that has ever been built, with a maximum instantaneous luminosity of 2×10^{33} cm^{-2}s^{-1} up to the Summer of 2011. While allowing the sensitivity of physics studies to increase at a high rate, this also means that processes with a very large cross section can occur multiple times per BC. Such additional interactions are termed 'pileup' and the effects are classified as in-time and out-of-time.

9.1.1 In-time pileup

In-time pileup effects occur in the same BC as the triggered event. These correspond to the additional tracks and calorimeter deposits resulting from multiple interactions between the bunches. Such detector signatures can be reconstructed as jets and so can effect the number of jets and the number of vertices in an event.

Many ATLAS analyses have jet counting cuts and can be affected if jets from the pileup interactions are selected. For example, an event that would not have been accepted by the analysis can pass the event selection by including pileup jets. Similarly, in events that require an isolated lepton that lepton may overlap with a pileup jet and again the selection efficiency

would be modified due to the additional interactions.

9.1.2 Out-of-time pileup

The finite response time of the ATLAS sub-detectors means that it can be possible for signals to span more than one BC. This can lead to, for example, changes in the energy scale of jets from out-of-time deposits in the calorimeters.

9.2 Luminosity measurement with ATLAS

Many aspects of the ATLAS physics program rely on accurate measurement of the luminosity delivered by the LHC. The luminosity is extracted by ATLAS using dedicated detectors and algorithms according to [135]. In general, the instantaneous luminosity ($\mathcal{L}$) is given by

$$\mathcal{L} = \frac{\langle\mu\rangle n_b f_r}{\sigma_{\text{inel}}}, \tag{9.1}$$

where $\langle\mu\rangle$ is the average number of inelastic interactions per BC, n_b is the number of colliding bunches, f_r corresponds to the machine revolution frequency[1], and σ_{inel} is the total inelastic pp cross section.

However, the LHC operates at an energy that has not been previously studied. This means that σ_{inel} is only known from theoretical predictions, at least in the early phases of ATLAS data-taking. To remove theoretical assumptions in the luminosity calculation, it is possible to re-define the luminosity in terms of the average number of visible interactions per BC, $\langle\mu^{\text{vis}}\rangle \equiv \epsilon\langle\mu\rangle$, and the total visible pp inelastic cross section, $\sigma_{\text{inel}}^{\text{vis}} \equiv \epsilon\sigma_{\text{inel}}$. These efficiencies cancel when calculating the luminosity, which reduces to

$$\mathcal{L} = \frac{\langle\mu^{\text{vis}}\rangle n_b f_r}{\sigma_{\text{inel}}^{\text{vis}}}. \tag{9.2}$$

[1] $f_r = 11.25$ kHz at the LHC

Therefore, σ_{inel} can be used as a calibration constant and the luminosity can then be calculated by determining $\langle\mu^{\text{vis}}\rangle$. Measurements of $\sigma_{\text{inel}}^{\text{vis}}$ are provided by van der Meer scans [136], while the measurement of $\langle\mu^{\text{vis}}\rangle$ is performed by integrating counts of interactions observed over a LB.

9.3 Evolution of luminosity and pileup

After the calibrated luminosity has been determined for a given LB it is then possible to estimate the absolute value of $\langle\mu\rangle$. This requires assuming some value for σ_{inel}, which is taken to be the calculation from `PYTHIA6` [98], corresponding to $\sigma_{\text{inel}} = 71.5$ mb. This agrees well with the measured total inelastic cross section of $\sigma_{\text{inel}} = 69.4 \pm 2.4$ (exp.) $\pm$ 6.9 (extr.) mb [137]. The $\langle\mu\rangle$ value can then be found by evaluating

$$\langle\mu\rangle = \frac{\mathcal{L}\sigma_{\text{inel}}}{n_b f_r} = 6.36 \times 10^{-30}\text{cm}^2\text{s}\ \frac{\mathcal{L}}{n_b}. \tag{9.3}$$

Note that $\langle\mu\rangle$ can be extracted in various ways, depending on how n_b is defined. If n_b is the total number of interacting BCs, then the average number of interactions per LB and per BCID ($\langle\mu\rangle_{\text{LB,BCID}}$) is obtained. Instead, if $n_b = 1$ and the value of $\mathcal{L}$ is measured for a given BCID, then the average number of interactions per LB ($\langle\mu\rangle_{\text{LB}}$) is obtained for that specific BCID.

Due to continual development of the LHC machine properties, the peak instantaneous luminosity observed by ATLAS tends to increase with time, see for example [138]. This may also correspond to an increase in $\langle\mu\rangle$, depending on the particular changes made to the LHC. For example, if the luminosity of individual bunches is increased then $\langle\mu\rangle$ will also increase, assuming that the number of bunches in the machine remains constant. However, if n_b is increased then $\langle\mu\rangle$ will decrease, assuming that the total luminosity remains constant, which would mean decreasing the luminosity per bunch. Some example detector conditions for Runs during 2010 and 2011 are shown in Table 9.1.

Run Number	Date	$\mathcal{L}^{\max}(\mathrm{cm}^{-2}\mathrm{s}^{-1})$	n_b	$\langle\mu\rangle^{\max}_{\mathrm{LB,BCID}}$
167776	28/10/2010	1.81×10^{32}	348	3.31
179710	15/04/2011	2.30×10^{32}	214	6.84
186721	02/08/2011	1.96×10^{33}	1317	9.47

Table 9.1: Typical luminosity dependent properties for a selection of runs in 2010 and 2011 [139].

9.4 Pileup in Monte Carlo

The ATLAS MC simulation includes pileup effects by overlaying a set of minimum bias events according to the methods described in Section 4.2. This method is sufficient for analyses that use a stable dataset, in a period where the machine is not active. However, as was shown in Section 9.3, the pileup conditions in ATLAS tend to change with time. A given MC production can take months to complete and so it is not efficient to produce a new set of MC samples every time the pileup conditions change. Therefore, each production is performed with a nominal setting for the $\langle\mu\rangle$ distribution. This is used as a sample from which Poisson distributions can be derived in bins of $\langle\mu\rangle$ to find the number of pileup events to use in the overlay. The MC samples can then be reweighted at a later stage such that the $\langle\mu\rangle$ distributions agree in data and MC. In this way the correct pileup conditions are included in the MC and conditions that are not relevant for the data are excluded.

9.4.1 Pileup reweighting

For the 1.04 fb^{-1} analyses, the pileup conditions in MC were reweighted to mimic data using the bin-by-bin ratio of the $\langle\mu\rangle_{\mathrm{LB,BCID}}$ distrubtion in data to the $\langle\mu\rangle$ distribution in MC. These distributions are shown on the left of Figure 9.1. In this process the normalisation is corrected for the difference in bin widths between data and MC, so that the MC cross section of the process is recovered after the reweighting procedure is applied. This creates a lookup table where the necessary pileup weight can be extracted using the MC $\langle\mu\rangle$ value used to simulate a given event. The set of weights obtained for the 1.04 fb^{-1} dataset and the `mc10b` production are shown in Table 9.2.

This technique results in the loss of a large number of MC events, as can be seen from the large number of zero and close to zero weights that are produced. This can be important for studies that have low event counts in certain regions and may become limited by the statistical error due to the low number of events in MC. In order to investigate the effect of the weights produced in this method, an additional comparison between the $\langle\mu\rangle_{\mathrm{LB}}$ distribution in data and the $\langle\mu\rangle$ distribution in MC is used in a similar way to the $\langle\mu\rangle_{\mathrm{LB,BCID}}$ reweighting. As can be seen in Figure 9.1, the tail of the $\langle\mu\rangle_{\mathrm{LB}}$ distribution in data has entries at higher values than the $\langle\mu\rangle_{\mathrm{LB,BCID}}$ distribution. This produces more non-zero weights but there is still a significant loss of MC events due to near zero weights. The comparison of the weights produced in this case are also shown in Table 9.2.

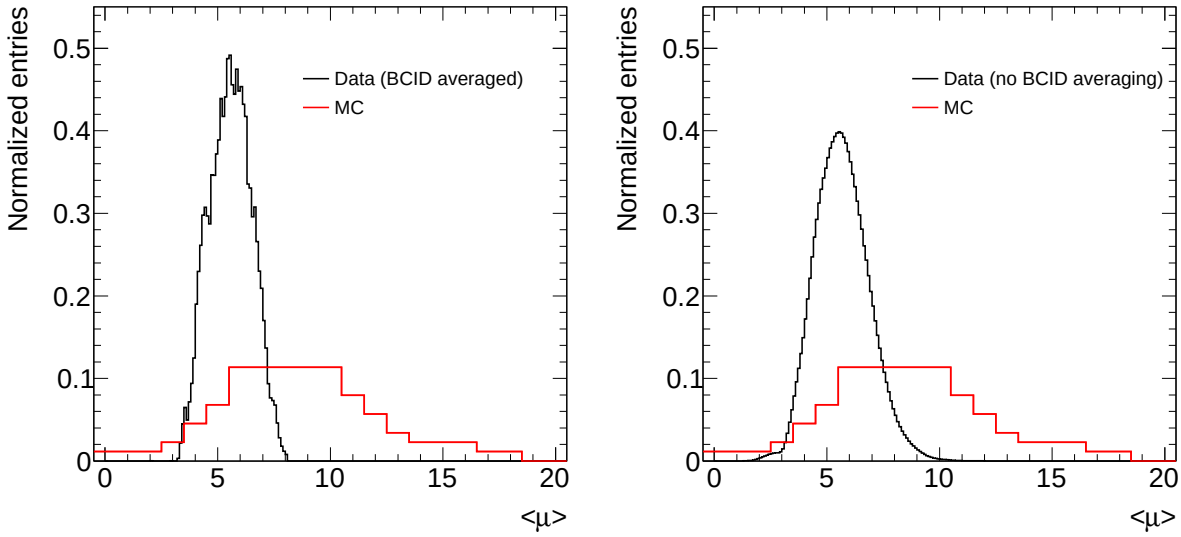

Figure 9.1: The $\langle\mu\rangle_{\mathrm{LB,BCID}}$ (left) and $\langle\mu\rangle_{\mathrm{LB}}$ (right) distributions in data compared to the $\langle\mu\rangle$ distribution in MC. The normalisation in data accounts for the binning in MC.

9.5 Estimating the actual number of interactions

As already mentioned, the number of interactions produced in a given BC is a Poisson process with mean $\langle\mu\rangle$. Therefore, it is possible to use the distributions given in Figure 9.1 to estimate the distribution of the actual number of interactions (N_{int}) for a given dataset. This is performed by generating a set of Poisson distributions, each with a mean $\langle\mu\rangle$ and a

MC $\langle\mu\rangle$	$\langle\mu\rangle_{\mathrm{LB,BCID}}$ Weight	$\langle\mu\rangle_{\mathrm{LB}}$ Weight
1	0.00	0.01
2	0.00	0.27
3	0.26	0.84
4	3.12	3.10
5	4.71	4.38
6	3.17	2.66
7	1.37	1.46
8	0.13	0.47
9	0.00	0.11
10	0.00	0.02

Table 9.2: Weights obtained from the $\langle\mu\rangle_{\mathrm{LB,BCID}}$ and $\langle\mu\rangle_{\mathrm{LB}}$ pileup reweighting methods for each MC $\langle\mu\rangle$ bin.

relative normalisation given by the fraction of luminosity at that $\langle\mu\rangle$ value. The distribution of $\langle\mu\rangle$ is denoted $f(\langle\mu\rangle)$. The individual Poisson distributions produced at each value of $\langle\mu\rangle$ are convolved by addition and renormalised to produce a probability density function, $f(N_{\mathrm{int}})$. The function $f(N_{\mathrm{int}})$ can then be used to find the likelihood of a given event having a certain number of interactions. Mathematically, this technique corresponds to

$$f(N_{\mathrm{int}}) = \frac{\sum_{\langle\mu\rangle} \left\{ f(\langle\mu\rangle) \times \frac{\langle\mu\rangle^{N_{\mathrm{int}}} e^{-\langle\mu\rangle}}{N_{\mathrm{int}}!} \right\}}{\sum_{\langle\mu\rangle} f(\langle\mu\rangle)}. \tag{9.4}$$

It is possible to generate $f(N_{\mathrm{int}})$ in both observed data and MC, where $\langle\mu\rangle_{\mathrm{LB,BCID}}$ is used in the case of data. The corresponding distributions are shown in Figure 9.2 for the `Egamma` data stream, using an integrated luminosity of 1.9 fb^{-1}. It is also possible to use these distributions to reweight the MC samples so that their N_{int} distributions match the data estimate, as the exact value of N_{int} is known in MC. The weights obtained from this method are shown in Figure 9.2.

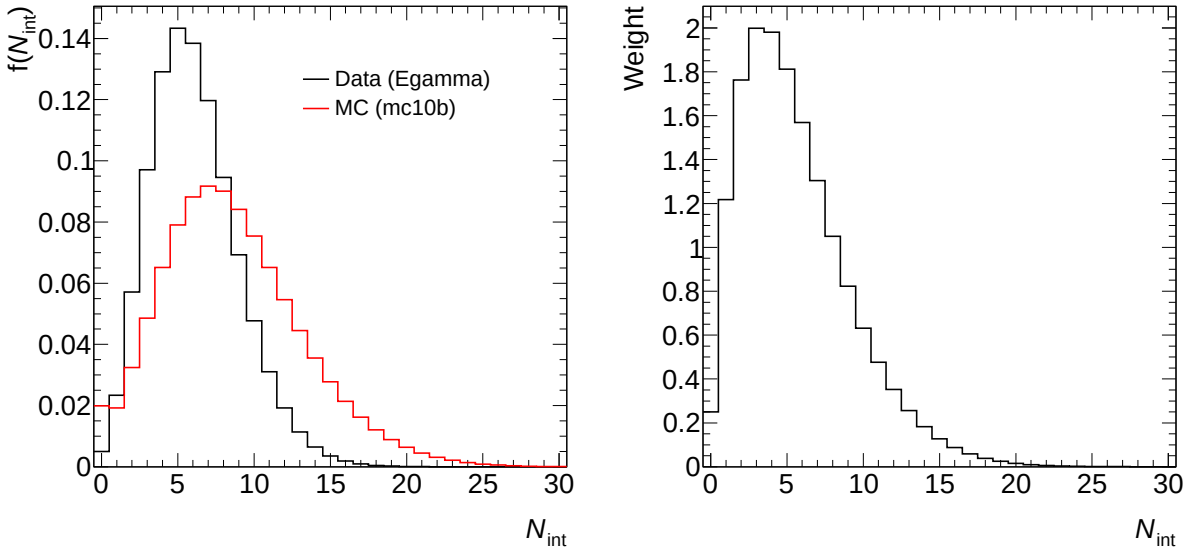

Figure 9.2: The estimated number of interactions in data and MC using an integrated luminosity of 1.9 fb^{-1} (left) and the associated weights (right).

9.6 Effects of pileup reweighting on analyses

The reweighting procedures described in Sections 9.4.1 and 9.5 may affect physics analyses that use MC as each method produces different sets of weights as can be seen in Table 9.2 and Figure 9.2. As a test case, the impact of the choice of reweighting procedure on the 1.04 fb^{-1} SUSY search with one lepton plus jets and missing transverse momentum [104] was studied. In this analysis, a W+jets control region (WR) and a $t\bar{t}$ control region (TR) were used to estimate the dominant background contributions. These backgrounds were then extrapolated into loose (L) and tight (T) signal regions.

This study only considers the effect on the regions that require three jets, although four jet regions were also used in the main analysis. The control and signal regions are defined in Table 9.3. In the case of the WR and TR, the two regions are separated such that the WR vetos any b-tagged jets while the TR requires at least one b-tagged jet. An additional control region is used in this analysis that will be defined as the W+jets plus $t\bar{t}$ control region (WR+TR), in which no b-jet selection is applied. The object definitions and event selection used in this analysis are documented in [104].

Cut	Signal Regions		Control Regions	
	3jL	**3jT**	**WR**	**TR**
Number of Leptons	Exactly 1			
Lepton p_{T} [GeV]	$> 25(20)$ for electrons (muons)			
Veto lepton p_{T} [GeV]	$> 20(10)$ for electrons (muons)			
Number of jets	≥ 3			
Leading jet p_{T} [GeV]	60	80	60	
Subsequent jets p_{T} [GeV]	25	25	25	
Number of b-tagged jets	-		Exactly 0	≥ 1
$\Delta\phi(\vec{p}_{\mathrm{T}}^{\,\mathrm{jet}}, \vec{p}_{\mathrm{T}}^{\,\mathrm{miss}})$	$[> 0.2$ (mod.$\pi)]$ for all 3 jets			
m_{T} [GeV]	> 100		$40 < m_{\mathrm{T}} < 80$	
$E_{\mathrm{T}}^{\mathrm{miss}}$ [GeV]	> 125	> 240	$30 < E_{\mathrm{T}}^{\mathrm{miss}} < 80$	
$E_{\mathrm{T}}^{\mathrm{miss}}/m_{\mathrm{eff}}$	> 0.25	> 0.15	-	
m_{eff} [GeV]	> 500	> 600	> 500	

Table 9.3: Control region and signal region definitions for the SUSY search with 1 lepton, jets and $E_{\mathrm{T}}^{\mathrm{miss}}$.

9.6.1 Expected event counts

The expected number of events in each control and signal region for the different reweighting procedures are shown for the electron channel in Table 9.4 and for the muon channel in Table 9.5.

Region	Expected Electron Channel Events		
	$\langle\mu\rangle_{\mathrm{LB,BCID}}$ **Weights**	$\langle\mu\rangle_{\mathrm{LB}}$ **Weights**	N_{int} **Weights**
3jWR	$664.65 \pm 2.05\%$	$665.22 \pm 1.98\%$	$673.60 \pm 1.69\%$
3jTR	$194.99 \pm 2.91\%$	$194.73 \pm 2.78\%$	$192.13 \pm 2.13\%$
3jL	$87.22 \pm 4.39\%$	$86.79 \pm 4.22\%$	$84.47 \pm 3.56\%$
3jT	$11.77 \pm 13.89\%$	$11.46 \pm 13.46\%$	$10.34 \pm 11.01\%$

Table 9.4: Expected numbers of events and the associated statistical uncertainty in the various three jet control and signal regions in the electron channel for each of the pileup reweighting schemes.

The central values of the expected numbers of events in the different control and signal regions show only a few percent variation between the different pileup reweighting procedures in the control regions, with the N_{int} method giving the largest difference. The effect of the choice of reweighting procedure is more pronounced in the signal regions, but the statistical

Region	Expected Muon Channel Events		
	$\langle\mu\rangle_{\mathrm{LB,BCID}}$ Weights	$\langle\mu\rangle_{\mathrm{LB}}$ Weights	N_{int} Weights
3jWR	$549.58 \pm 3.09\%$	$548.64 \pm 2.97\%$	$543.36 \pm 2.14\%$
3jTR	$139.74 \pm 3.89\%$	$139.87 \pm 3.75\%$	$141.09 \pm 2.90\%$
3jL	$66.58 \pm 4.83\%$	$67.57 \pm 4.66\%$	$71.09 \pm 3.93\%$
3jT	$8.36 \pm 13.95\%$	$8.57 \pm 13.57\%$	$8.97 \pm 11.71\%$

Table 9.5: Expected numbers of events and the associated statistical uncertainty in the various three jet control and signal regions in the muon channel for each of the pileup reweighting schemes.

uncertainty on the expected number of background events is large, so it is not possible to draw any clear conclusions. However, the relative uncertainties are very similar for the $\langle\mu\rangle_{\mathrm{LB,BCID}}$ and $\langle\mu\rangle_{\mathrm{LB}}$ methods but rather smaller for the N_{int} method. Therefore, the N_{int} method may be beneficial for studies that suffer from low numbers of MC events. However, the $\langle\mu\rangle_{\mathrm{LB}}$ and N_{int} procedures only take into account in-time pileup as they contain no information linking different BCIDs. This does not seem to be a large effect, as evident from the small variations in the expected event counts between the different methods.

It should be noted that further corrections are required to account for out-of-time pileup effects on the calorimeter response. This is included in the calculation of the jet energy scale, for example, and is not studied in detail here.

9.7 Pileup effects on acceptance

The choice of reweighting procedure is not the only way that pileup can effect the expectations of such an analysis. Pileup will tend to increase the number of jets in an event. For analyses that require jet selections this may cause an event to pass these cuts that would have failed if no pileup was present. The result of this is that the acceptance in certain kinematic regions may depend on $\langle\mu\rangle$. In the case of new physics searches, any pileup contamination may be detrimental, as additional events may enter the analysis. If this results in extra events being accepted into the control regions, then the backgrounds may be over estimated and new physics signals masked. If, on the other hand, extra events are accepted

into the signal regions, false positive signals may be produced which are in fact due to pileup rather than a real new physics process.

The effects of pileup on the acceptance can be studied by considering the distribution of vertex multiplicity[2] (N_{vtx}). If this distribution is measured using a broad selection and then compared to a tighter selection, with additional cuts added, any modification in the shape of the N_{vtx} distribution may suggest that the acceptance is affected by pileup. Indeed the ratio of the N_{vtx} distribution in the tight region to that in the loose region can be thought of as the acceptance of the analysis as a function of N_{vtx}. Ideally, an analysis should not be sensitive to the number of vertices in a given event, as generally analyses are only concerned with one high p_{T} process per event. Therefore, if the acceptance is not flat as a function of N_{vtx} then vertices that are of no interest to the analysis will have an affect on the event selection. These acceptance distribtions are shown for the WR and TR with the three jet selection applied in Figure 9.3. The normalisation for the acceptance is taken from the WR+TR without a jet selection applied.

Clearly, from these distributions, pileup has an effect on the acceptance of the one lepton SUSY search. However, the effect is no so evident in the TR as for the WR. The lack of N_{vtx} dependence on the TR acceptance is likely to be because $t\bar{t}$ events produce multiple jets in the high p_{T} process of interest. Therefore, any additional pileup jets may affect the overall jet multiplicity but will not cause extra events to pass the selection. There is some evidence for a downward slope in acceptance, which may be due to additional pileup jets overlapping with the lepton and causing the event to fail the lepton isolation criteria. However, the acceptance in the TR is still rather consistent with being flat, so this is not likely to be a large effect.

In the case of the WR, on the other hand, the acceptance depends strongly on the value of N_{vtx}. The cross section for W production in association with n jets is much higher than the cross section for W production with $n+1$ jets. Therefore, it may be the case that events with, for example, W production with two associated jets in the high p_{T} process are accepted

[2]In this analysis, the vertex multiplicity is defined as the number of vertices that have at least two associated tracks.

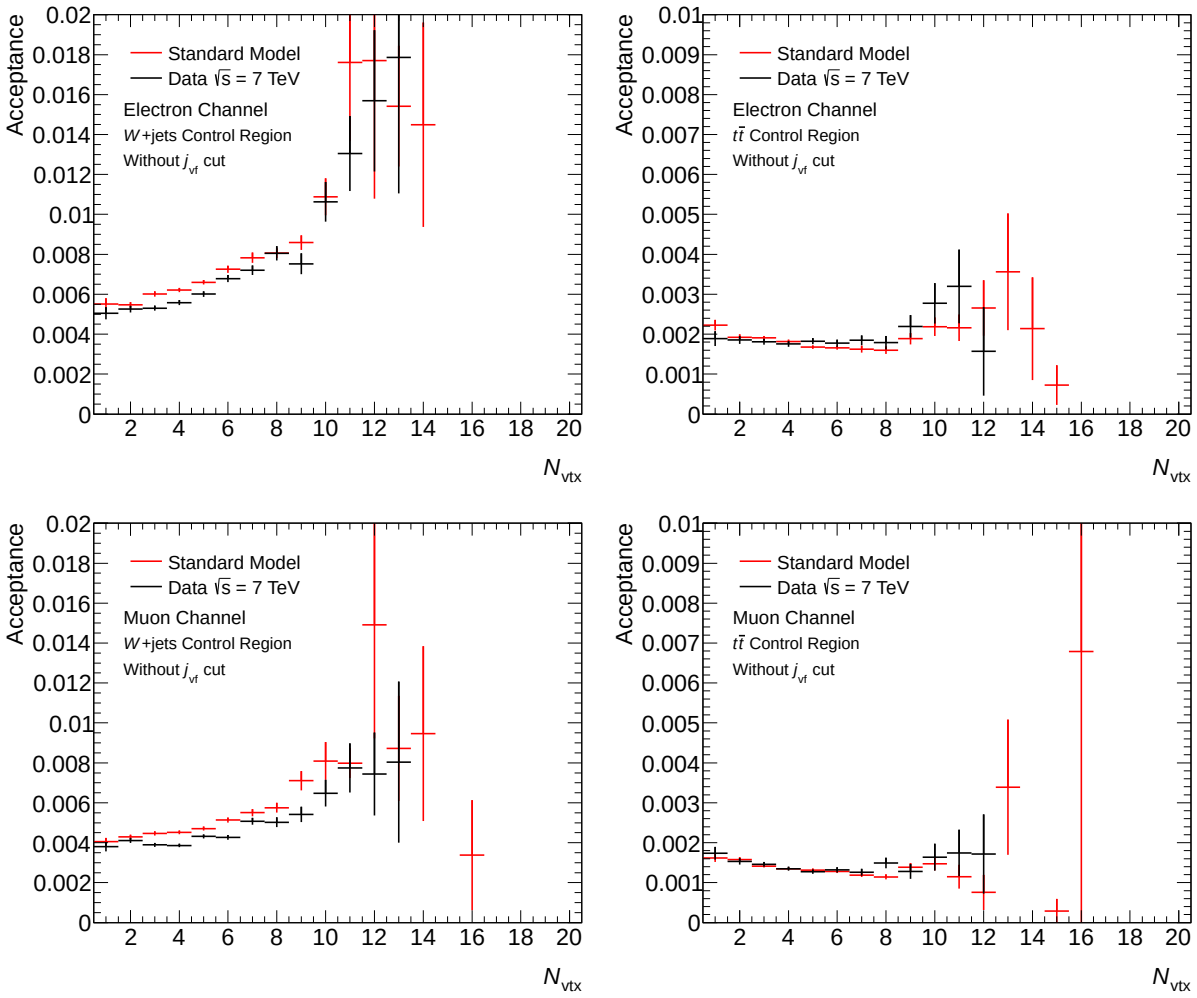

Figure 9.3: The acceptance as a function of N_{vtx} in the WR (left) and TR (right) for the electron (top) and muon (bottom) channels with a three jet selection. The normalisation is obtained from the WR+TR without a jet selection applied.

due to one of the pileup jets passing the necessary cuts.

Note that the high p_{T} process alone is equivalent to the $N_{\text{vtx}} = 1$ bin and so selections that are not affected by pileup should have the acceptance of the high p_{T} process in all bins.

9.8 Controlling pileup

Events entering the analysis by accepting pileup jets is clearly not favourable. To remove these pileup jets, we can consider a variable that compares the transverse momentum of tracks that are associated with a jet and the highest sum p_{T} vertex (the primary vertex)

with the total transverse momentum of tracks associated with the jet. This variable is called the jet vertex fraction, j_{vf}, and is defined for a particular jet as

$$j_{\mathrm{vf}}^{\mathrm{jet}} = \frac{\sum_{i \in \mathrm{tracks}} p_{\mathrm{T}}^{i}(\mathrm{jet}\ \&\&\ \mathrm{primary\ vertex})}{\sum_{i \in \mathrm{tracks}} p_{\mathrm{T}}^{i}(\mathrm{jet})}. \tag{9.5}$$

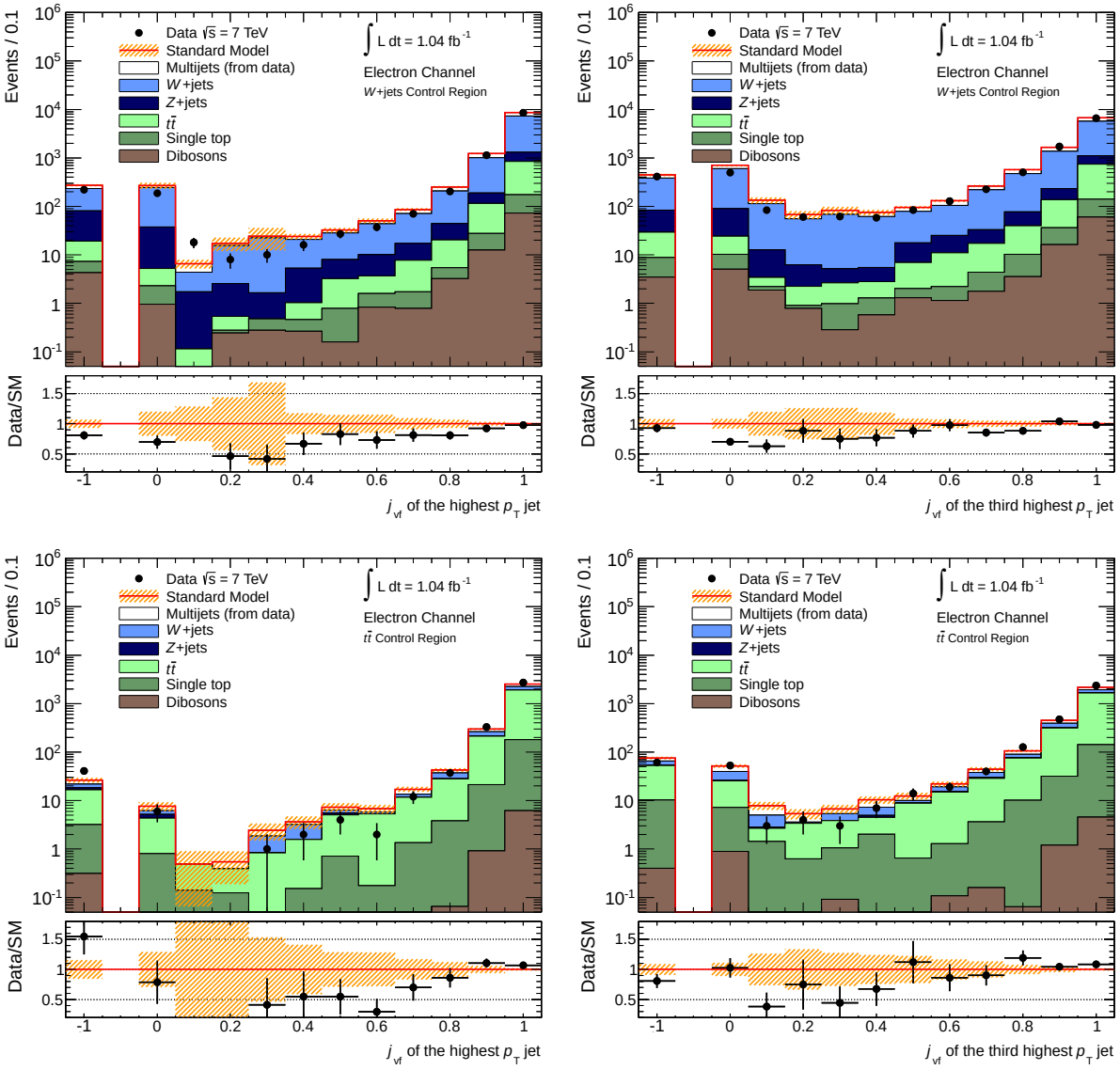

Figure 9.4: Highest (left) and third highest (right) p_{T} jet j_{vf} distributions in the WR (top) and TR (bottom) for the electron channel. The hashed band shows the uncertainty on the background estimate due to MC statistics.

Figure 9.4 gives example distributions of j_{vf}. Clearly this variable is peaked at one for jets that are fully associated with the primary vertex. It then falls to lower values as jets

start to contain contributions from tracks that are associated with other vertices. There is another peak at 0 from jets that have no association with the primary vertex at all. It is therefore likely that jets with j_{vf} values of one are associated with the high p_{T} process of interest, while jets with j_{vf} values of zero are pileup jets. The jets with values of j_{vf} between zero and one have an ambiguous nature and may or may not be due to pileup. However, it is more likely that jets with lower j_{vf} values are due to pileup, or at least contain significant contamination from pileup tracks, than those with higher values. The j_{vf} distribution reaches approximately the same height in the zero and 0.75 bins and so the pileup contribution for $j_{\mathrm{vf}} > 0.75$ is likely to be low.

There is an additional peak at negative one. This is from jets that have no tracks associated with them and so the j_{vf} cannot be evaluated. This includes, by definition, all jets that fall outside the acceptance of the inner tracker, having $|\eta| > 2.5$. The 1.04 fb^{-1} one lepton SUSY search included jets in the range $|\eta| < 2.8$. Therefore, to keep jets that fall outside of the acceptance of the tracker in the analysis, the cut applied to remove jets from pileup is $|j_{\mathrm{vf}}| > 0.75$.

This $|j_{\mathrm{vf}}| > 0.75$ cut is only applied to the jets after the overlap criteria, described in Section 4.4, have been satisfied and the event cleaning has been performed. Jets with $|j_{\mathrm{vf}}| > 0.75$ are termed 'signal' jets and are used to satisfy the jet counting selection and for the calculation of kinematic variables.

As can be seen in Figure 9.4, the MC over predicts the j_{vf} by up to 40% for values close to zero when compared to the observed data. Therefore, the MC can be expected to contain more pileup jets than the data. However, the agreement is generally much better for values of j_{vf} close to one, which is the j_{vf} value assigned to most jets that enter the event selection. The m_{eff} and $E_{\mathrm{T}}^{\mathrm{miss}}$ distributions are shown, before and after the j_{vf} cut is applied, for events passing the three jet selection in Figure 9.5 to check any potential effects of the mis-modelling of the j_{vf} distribution at low values. The differences between the m_{eff} and $E_{\mathrm{T}}^{\mathrm{miss}}$ distributions before and after the j_{vf} cut is applied are minimal and so it seems to be a viable method by which the pileup contribution to the analysis may be controlled.

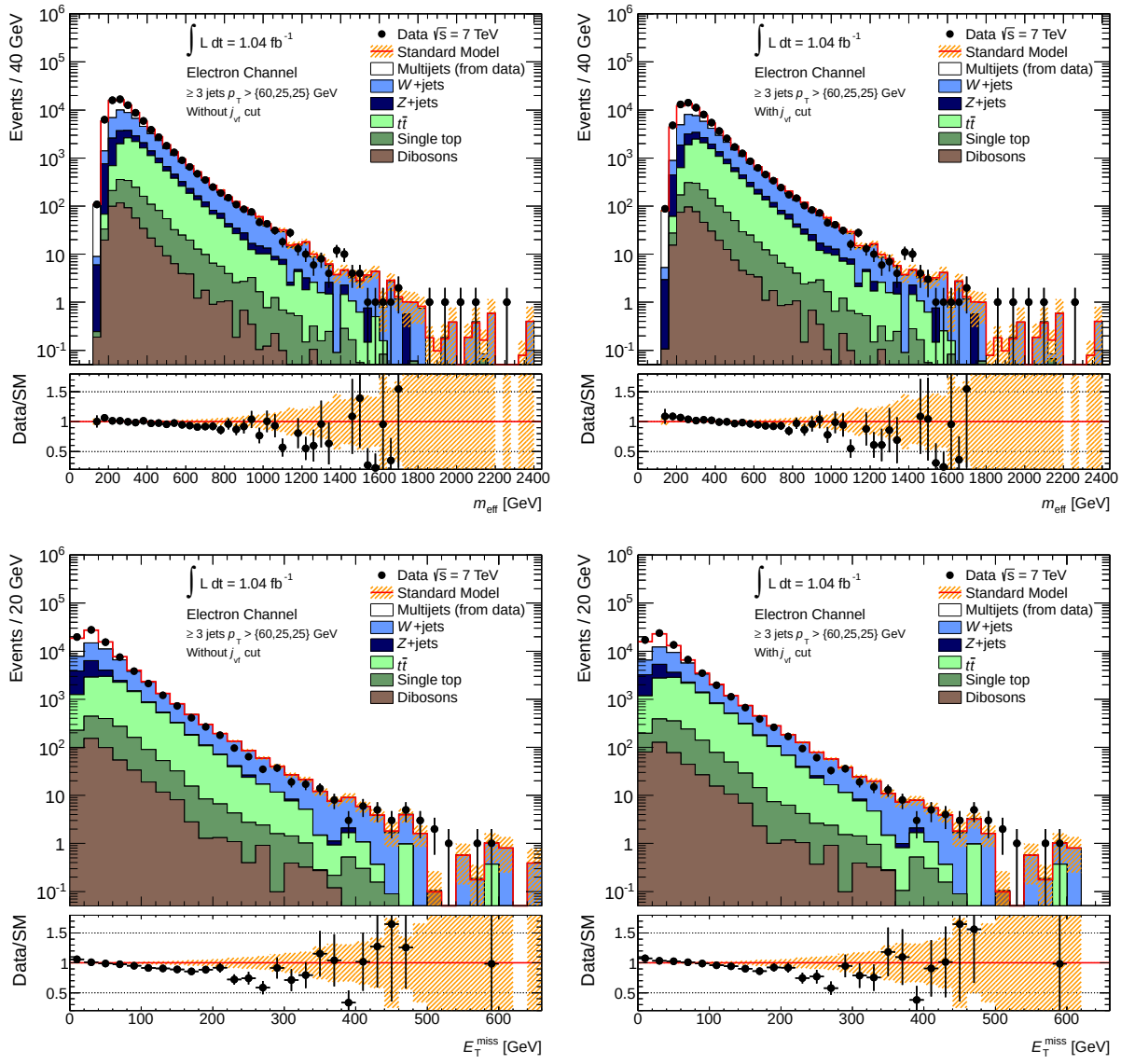

Figure 9.5: m_{eff} (top) and $E_{\text{T}}^{\text{miss}}$ (bottom) distributions without (left) and with (right) the j_{vf} cut applied in the electron channel with a 3 jet selection.

9.8.1 Acceptance with a vertex fraction cut applied

The acceptance of the WR and TR is re-assessed with the $|j_{\text{vf}}| > 0.75$ cut applied in Figure 9.6. Again, the normalisation is taken from the combined WR+TR without jet cuts. These distributions are significantly flatter than those in Figure 9.3. This indicates that, indeed, the effect of pileup on the event selection in these kinematic regions is well controlled by only including jets with $|j_{\text{vf}}| > 0.75$. In addition to this control on the variation of the acceptance, it is also important to note that the acceptance remains at about 0.4% in the WR before and after the $|j_{\text{vf}}| > 0.75$ cut is applied. The TR still shows some evidence for

a downward trend in acceptance as N_{vtx} increases. However, the shape of the acceptance in the TR as a function of N_{vtx} is similar both with and without the j_{vf} cut applied. This may indicate that there is some residual pileup effect that is not removed by the j_{vf} cut, for example jets overlapping with the lepton.

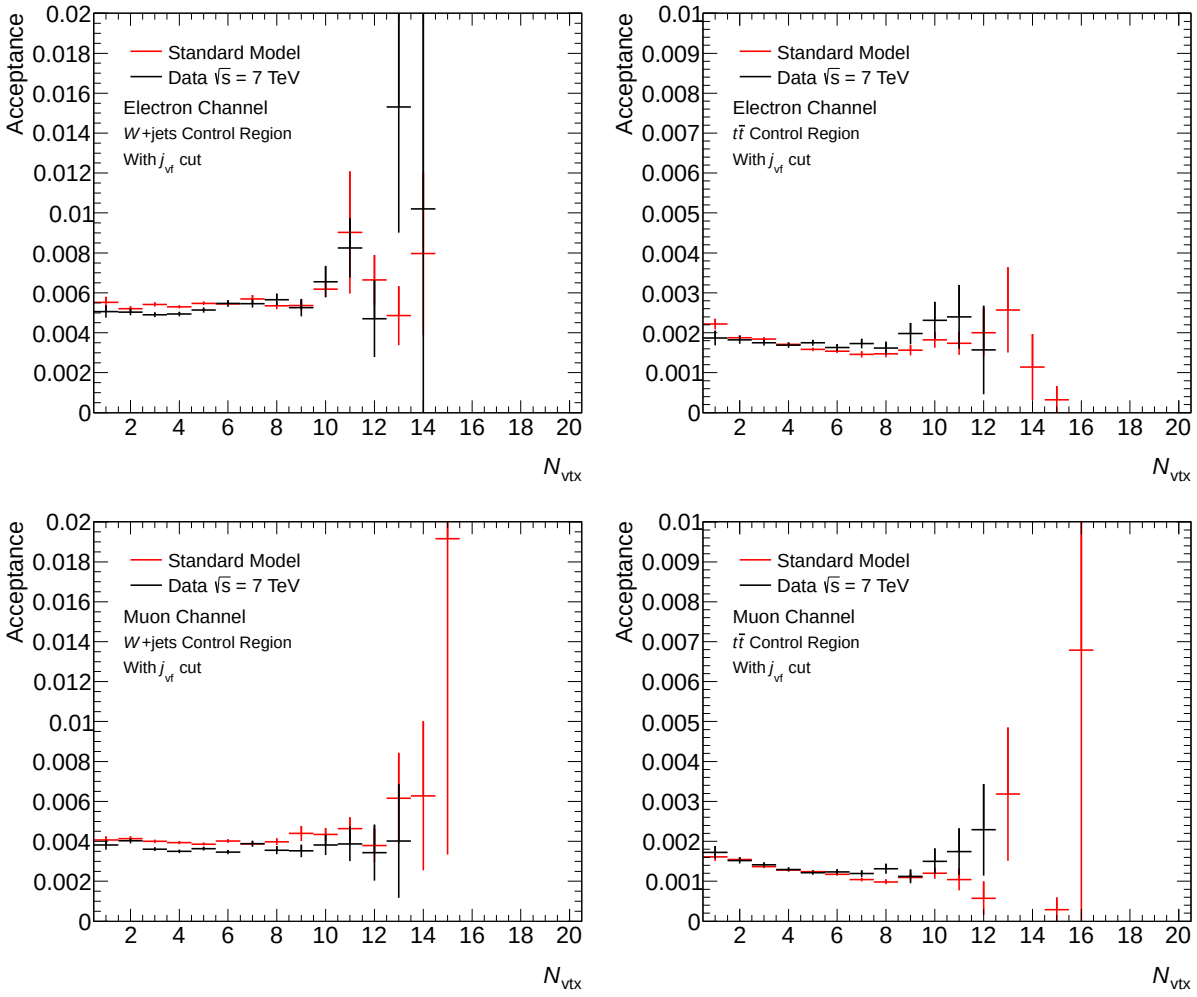

Figure 9.6: The acceptance as a function of N_{vtx} in the WR (left) and TR (right) for the electron (top) and muon (bottom) channels with a three jet selection and the application of a $|j_{\text{vf}}| > 0.75$ cut on the selected jets.The normalisation is obtained from the WR+TR without a jet selection applied.

Chapter 10

Monitoring the SCT Tx optical links

10.1 The SCT data acquisition system

Each sub-detector of ATLAS has its own DAQ system, which is used to communicate with the detector. This can be either controlled by the central ATLAS DAQ, for example during data-taking, or each sub-detector can have independent control over its own DAQ system, so that system tests and calibrations can be performed. This Chapter is concerned with the communication of the SCT DAQ system between crates located away from the detector and the on-detector components. The SCT DAQ is described in detail in [140].

The SCT, which was introduced in Section 3.4.1, forms the intermediate layer of the ATLAS ID and is used to track the trajectory of particles before they reach the calorimeter. There are 4088 on-detector modules, each with 768 strips on each side. This results in over six million read-out channels. The SCT is made up of four barrel layers and 18 end-cap discs (nine on each side of the detector). It provides measurements of charged particles in the range $|\eta| < 2.5$.

Being located within 610 mm of the beam pipe means that the SCT must survive in a harsh radiation environment, while being able to read out physics data efficiently. Over its 10 year operational lifetime, the SCT can expect to receive an ionising dose of 100 kGy Si and a

non-ionising dose of 2×10^{14} 1 MeV neutrons/cm^2 equivalent. This requires the selection of specific radiation-hard semiconductor components. Furthermore, the SCT resides in a strong magnetic field, and any components selected to communicate with the detector must be able to handle fast signals, provide low electrical noise and have a minimal material budget. For these reasons, among others, optical electronics devices are used to transmit information to and from the SCT.

10.1.1 Components of the SCT DAQ

A schematic of the SCT DAQ system is shown in Figure 10.1.

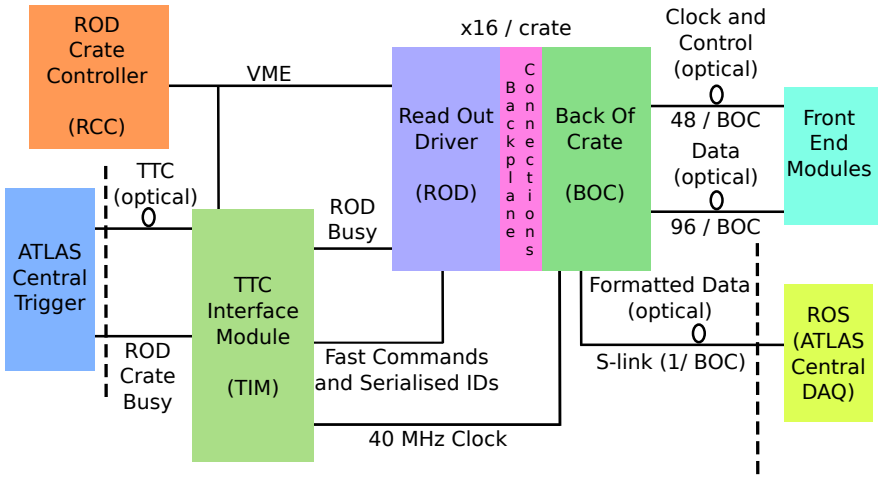

Figure 10.1: Block diagram of the SCT DAQ hardware showing connections between the main components. Based on [140].

These various components can be grouped into three main sections, which form a crate. The SCT DAQ consists of eight crates in total. The components of a single crate are listed below:

1. The 16 read-out driver (ROD) cards control the on-detector module configuration, trigger propagation and data formatting. They also provide the means by which the detector can be monitored and calibrated. Field programmable gate arrays (FPGAs) are used to perform time critical operations - specifically formatting, building, and routing the event data. An additional FPGA controls the ROD setup, module configuration and trigger distribution. The FPGAs themselves are configured by digital

signal processors (DSPs), each ROD having one "master" (MDSP) and four "slaves" (SDSPs). Once configured, the FPGAs handle the data independently.

2. The 16 back of crate (BOC) cards provide the communication path between the off-detector hardware and the detector modules. They distribute the trigger, clock and control to the on-detector modules via an optical transmission path (Tx) and also receive data from the on-detector modules via an optical reception path (Rx). The BOCs are also used to send event data, received from the on-detector modules, to the ROD for formatting and then transmits this formatted data onward to the ATLAS central DAQ.
3. Timing, trigger and control (TTC) interface modules (TIMs) interface the clock and trigger signals from the ATLAS central TTC system with the RODs and associated BOCs. This provides synchronisation with the ATLAS 40 MHz clock which, in turn, is synchronised with the LHC 40 MHz clock. However, the phase of the LHC clock may have shifted by the time it reaches the SCT and so the readout must be tuned to maximise efficiency. The TIMs also allow the ATLAS central DAQ to control the triggers used and to configure the system, for example by setting up the detector to measure physics information. If a ROD becomes busy and unable to process information at the necessary rate, the TIM will request that the central DAQ stops sending triggers to that ROD.

10.1.2 Data transmission

Information is sent to and from the on-detector modules using optical links, these are generally termed Tx and Rx links, respectively. A summary of the optical system is given in Figure 10.2.

For the Tx, which this Chapter focuses on, the electronic data from the TTC is converted to optical light by driving an array of 12 vertical cavity surface emission lasers (VCSELs). Each VCSEL is coupled to an optical fibre, down which the signal travels. The light is converted back into an electrical signal by one *p-i-n* (PIN) diode per on-detector module

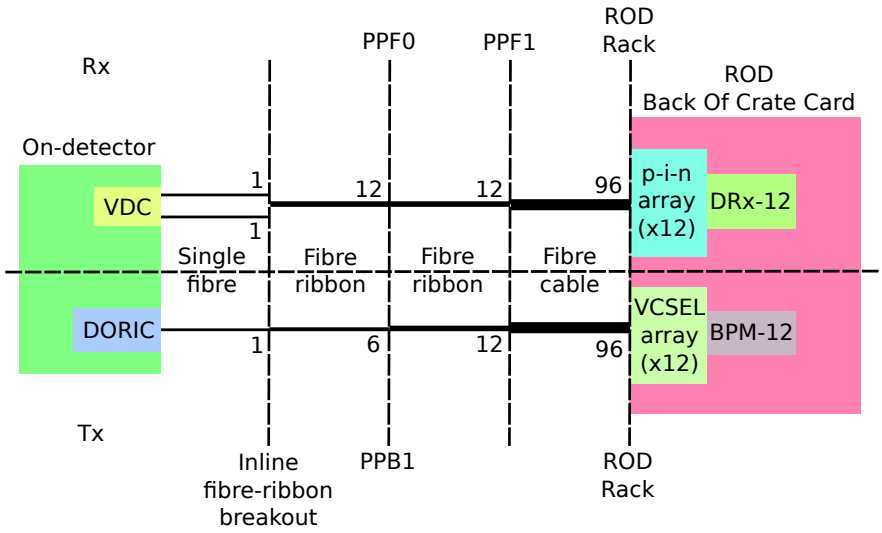

Figure 10.2: Schematic of the ATLAS SCT optical links system architecture. The top half corresponds to the Rx pathway while the bottom corresponds to the Tx pathway. Based on [141].

and separated into the 40 MHz clock and the 40 Mbit/s control data stream. If a link fails it is possible to re-route the data between adjacent modules, so that the system can still operate in the limit of few optical failures. This redundancy has limitations from the SCT geometry and cannot operate if adjacent links fail. If a link cannot be recovered it is possible to replace the corresponding VCSEL array in the BOC, when access to the counting room is allowed.

The Rx system consists of two VCSELs per module, each usually corresponding to one side of the on-detector module. The light is passed down an optical fibre, and received by an array of 12 PIN diodes on a given BOC card. The electrical signal produced by these diodes is interpreted and sent to the ROD for formatting. A redundancy system also exists for the Rx such that in the case of one link failing on a module the data from both sides can be read out of the working link.

10.2 Motivation for monitoring the optical system

It is clear that a functional optical communication system is vital to the operation of the SCT. However, numerous link failures were identified soon after installation. These corresponded

to, for example, fibre breaks during assembly and electrostatic discharge (ESD) damage to the VCSELs during production. The effects of ESD damage may not be immediate. For this reason, and to check that there are no other long term effects that may be dangerous to the system, it is wise to monitor any changes in the system over time.

It is possible to monitor both the Rx and Tx systems, however this study will only show the case of the Tx system. This is because it turns out that the Tx failure rates are much higher than the Rx and it is possible to replace failed Tx VCSEL arrays.

10.3 Monitoring the SCT Tx system

The monitoring of the Tx system is based on measurements of the current produced by the PIN diode (I_{PIN}) for each Tx link. These values can be accessed from the detector control system (DCS) database, which is regularly updated. This section will begin by describing the methods used to access the I_{PIN} values and the general form of the I_{PIN} distribution. These I_{PIN} distributions will be used to give a convenient definition of a failed link. The global evolution of the system, individual channels and the failure rates will then be studied. Statistical analysis of the failure rates will be used to predict the mean time to failure (MTTF) that would be expected for any given link. Finally a search for correlations between environmental conditions and the failures will be undertaken.

Studies are shown for the period September 18$^{\mathrm{th}}$ 2009 to October 14$^{\mathrm{th}}$ 2010 as the VCSEL array replacement rate over this time is low. Further studies would be required to separate old and new arrays for more recent scans. However, there is enough information in scans over this period to draw some interesting conclusions.

10.3.1 Extracting the PIN currents

The I_{PIN} values are accessed daily from the DCS database. As the values are updated throughout the day, it is necessary to chose how to extract the I_{PIN} in the most meaningful

way. The maximum I_{PIN} for the day is used in order to prevent any false errors being picked up by the system being temporary turned off.

Before any further analysis, the I_{PIN} must be corrected for the base-line current across the diode. This is measured by a reference scan, performed in September 2009, with the diodes powered but without light incident on them. These reference values, known as pedestal currents (I_{ped}), are subtracted from the measured I_{PIN}. This allows a threshold cut to be used to define failures. Without the I_{ped} subtraction, failed links could be misidentified as functional. The distributions of I_{ped}, I_{PIN} and $I_{\mathrm{ped}} - I_{\mathrm{PIN}}$ are shown in Figure 10.3 for the scan taken on October 13$^{\mathrm{th}}$ 2010.

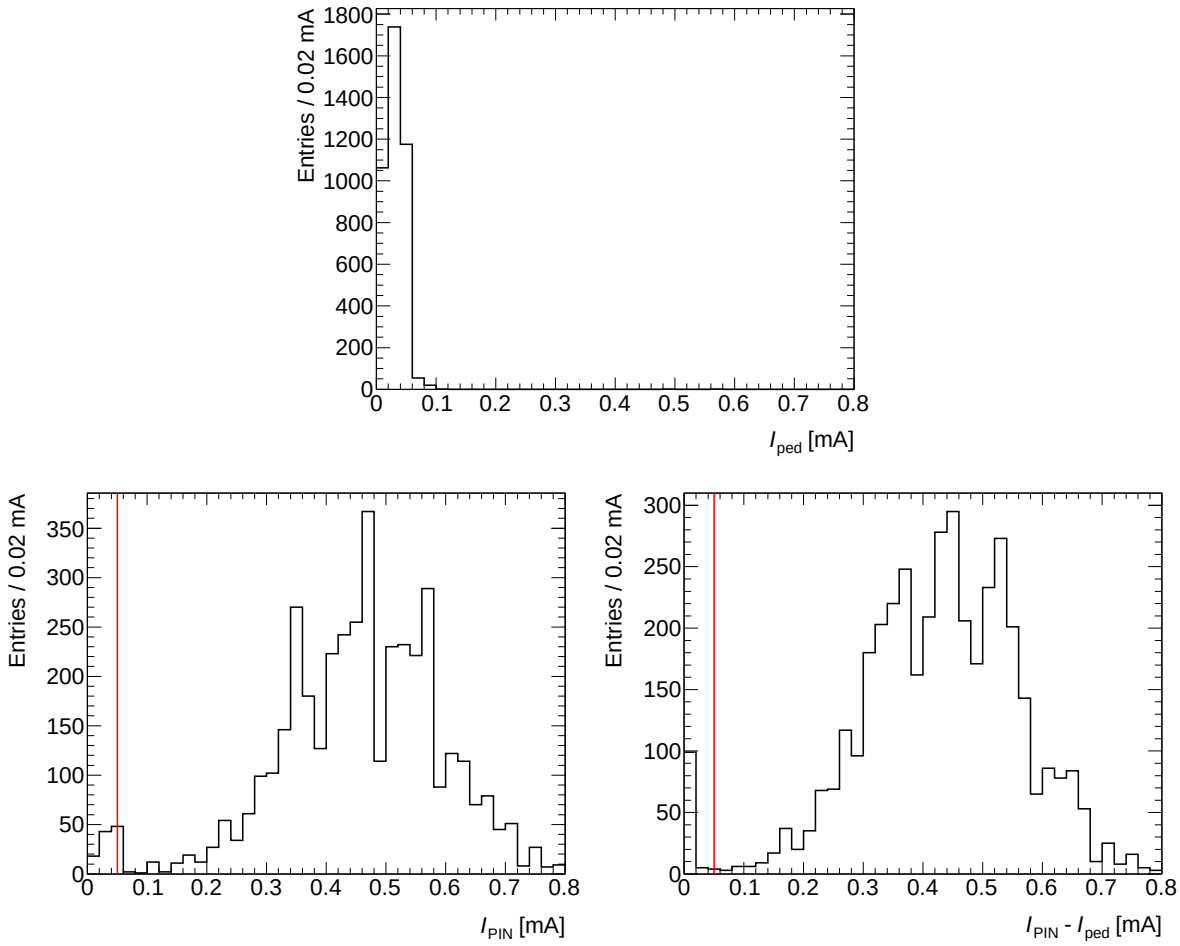

Figure 10.3: The I_{ped}, I_{PIN} and $I_{\mathrm{PIN}} - I_{\mathrm{ped}}$ distributions for the scan taken on October 13$^{\mathrm{th}}$ 2010. Points to the left of the red line, in the range $I_{\mathrm{PIN}} - I_{\mathrm{ped}} < 0.05$ mA, would be defined as potential failures.

10.3.2 Defining a failure

This distribution of $I_{\mathrm{PIN}} - I_{\mathrm{ped}}$ in Figure 10.3 shows a clear peak around zero, which can be expected to contain failed links. Using the daily structure of $I_{\mathrm{PIN}} - I_{\mathrm{ped}}$, a well placed cut can be used to define a population of links with $I_{\mathrm{PIN}} < 0.05$ mA as failed links. This covers all of the peak population close to zero and some of the associated tail, to avoid false-negative conclusions. Any true failures will be consistently in this population. Therefore, if a link drops into this population but leaves the population at some later time, then that link may have low light levels and fluctuate into the failure populations but otherwise be a working link. If the link remains in the failure population, then a strong case can be put forward that a consistently failed link is actually terminal.

10.3.3 Global evolution

Now that it is possible to monitor the daily $I_{\mathrm{PIN}} - I_{\mathrm{ped}}$ distribution, comparisons can be made between distributions over many days. This will eventually provide a system for the long term monitoring of the optical links. One interesting distribution to consider is the evolution of the mean $I_{\mathrm{PIN}} - I_{\mathrm{ped}}$ ($\langle I_{\mathrm{PIN}} - I_{\mathrm{ped}} \rangle$) over time. This shows the overall performance of the system and can be used to monitor any global changes such as the SCT being turned off or any power surges. An example of a long term $\langle I_{\mathrm{PIN}} - I_{\mathrm{ped}} \rangle$ monitoring plot can be seen in Figure 10.4.

At early dates, up until the start of 2010, the $\langle I_{\mathrm{PIN}} - I_{\mathrm{ped}} \rangle$ rises from 0.33 mA to 0.42 mA. This is likely to be related to darkening of high order transverse modes of the VCSELs. As the total power output is constant, then the darkening of these modes results in more power being available for lower order modes, which have better coupling to the optical fibre, hence the light received by the PIN diode gets brighter over time.

The clear gap between 2009 and 2010 corresponds to the winter shutdown, over which the entire SCT system was turned off. There are also shorter periods where the DAQ system was off and the $\langle I_{\mathrm{PIN}} - I_{\mathrm{ped}} \rangle$ drops to zero.

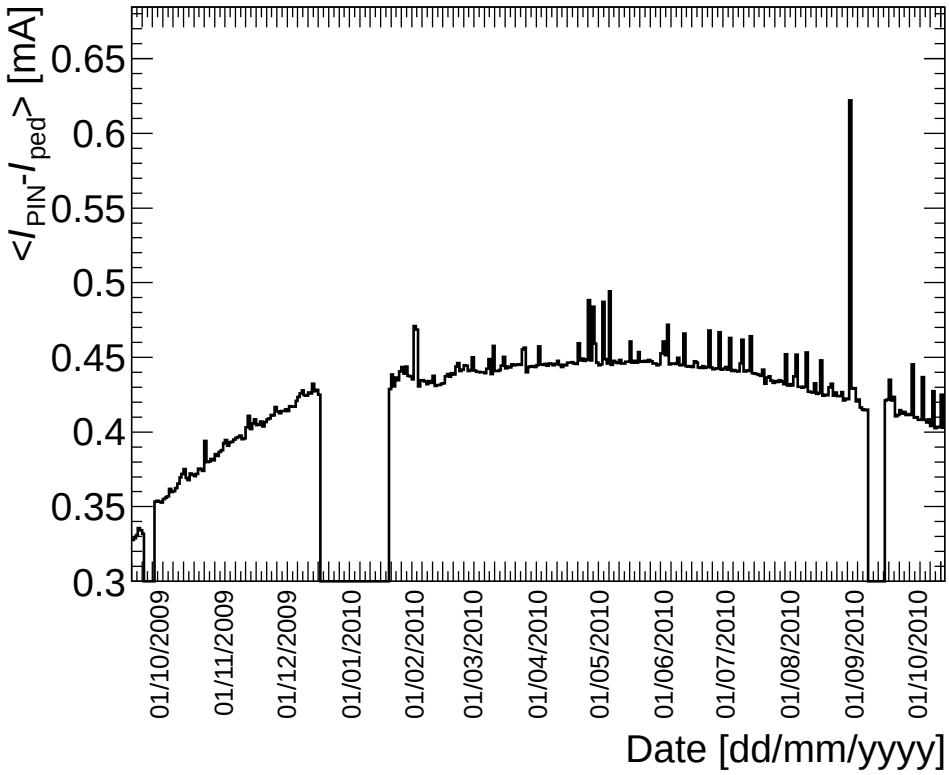

Figure 10.4: The long term $\langle I_{\mathrm{PIN}} - I_{\mathrm{ped}} \rangle$ between September 18$^{\mathrm{th}}$ 2009 and October 14$^{\mathrm{th}}$ 2010.

Small spikes exist throughout the distribution, corresponding to days when calibration scans were performed. During such scans the optimal settings for the DAQ system are investigated, involving tuning the driving current of the VSCELs to optimise gain and noise. It is therefore probable that the intensity of the light sent down the fibre is temporarily increased. This is not a problem for the monitoring system as any failed channels will remain with an $I_{\mathrm{PIN}} - I_{\mathrm{ped}}$ value close to zero despite these scans. There is one large spike in September 2010 that corresponds to a power surge in ATLAS.

The final feature of note is the gradual decrease during 2010. It is likely that the increasing number of dead channels in the system contributes to this, in the case where a significant number of failures are present. If the $I_{\mathrm{PIN}} - I_{\mathrm{ped}}$ drops close to zero for enough links then the $\langle I_{\mathrm{PIN}} - I_{\mathrm{ped}} \rangle$ could be significantly decreased. This is exacerbated when VCSEL arrays are replaced, as the whole set of 12 new VCSELs will tend to be installed with low I_{PIN} values, before going through the brightening phase.

10.3.4 Evolution of individual channels

As well as monitoring the system as a whole, it is interesting to look at the evolution of particular links. Any features that occur in the global distributions can be verified against these individual channel distributions. Example distributions without a failure can be seen in Figure 10.5, while distributions that contain a failure are shown in Figure 10.6.

It is clear from these plots that categorising optical links is not an easy task. Taking the distributions without failures, in Figure 10.5 as an example, some links are rather stable, such as 20220170200240. Other links, such as 20220270300177 and 20220330200009 show evidence for brightening but not darkening, while 20220130000654 and 20220240100538 go through phases of both brightening and darkening. It should also be noted that, while all of the links in Figure 10.5 show no signs of failure themselves, they can be affected by VCSEL array replacements. For example 20220270300078 shows a sudden drop in I_{PIN} in late July, which is likely to correspond to a replacement. As many models go through brightening phases, it is likely that a replacement VCSEL will tend to have lower I_{PIN} values than the original VCSEL.

The brightening phase could explain the global rise in $\langle I_{\mathrm{PIN}} - I_{\mathrm{ped}} \rangle$ for early times in Figure 10.4. Similarly, the darkening phase seen by some modules and the fact that replacements tend to have lower I_{PIN} could explain, at least in part, the decrease in global $\langle I_{\mathrm{PIN}} - I_{\mathrm{ped}} \rangle$ at later times.

The most interesting potential categorisation would be to find modules that show signs of pre-failure. In certain failure scenarios, a pre-failure darkening may be expected, for example. However, from Figure 10.6, there are no clear signs that may be used to predict the failure of a given link. Some links, like 20220380200091 and 20220270300055 brighten and then go through a stable phase before suddenly failing. Other links, such as 20220330200680 and 202202810100025 do show some darkening, but not in a consistent manner that could be used to predict the failure, particularly when compared to links with no failures in Figure 10.5. Finally, some links that fail show erratic behaviour, as is the case for 20220990291319 and

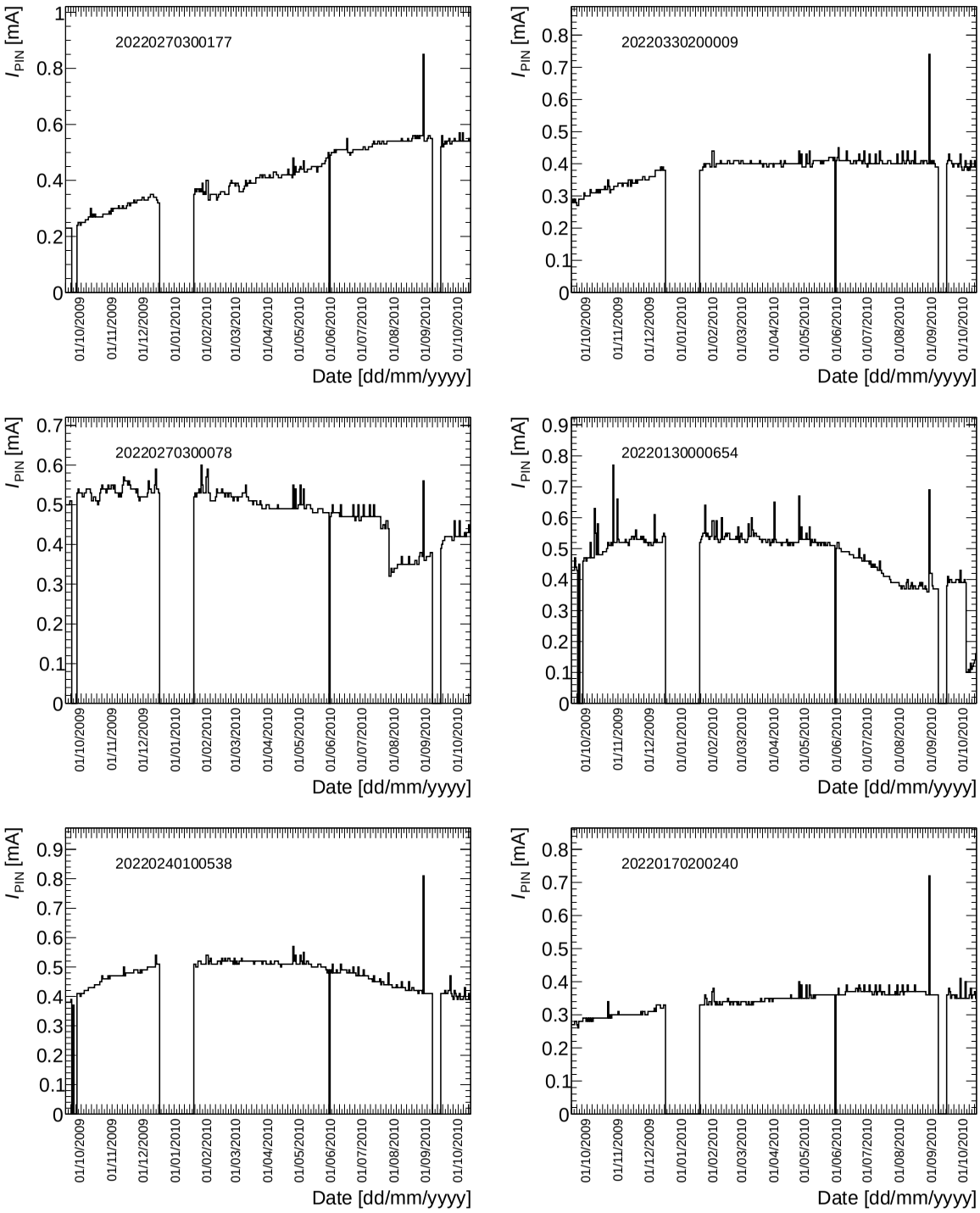

Figure 10.5: The I_{PIN} evolution over time of a randomly selected set of six channels without failures between September 18$^{\mathrm{th}}$ 2009 and October 14$^{\mathrm{th}}$ 2010. The relevant serial number of the on-detector modules are indicated.

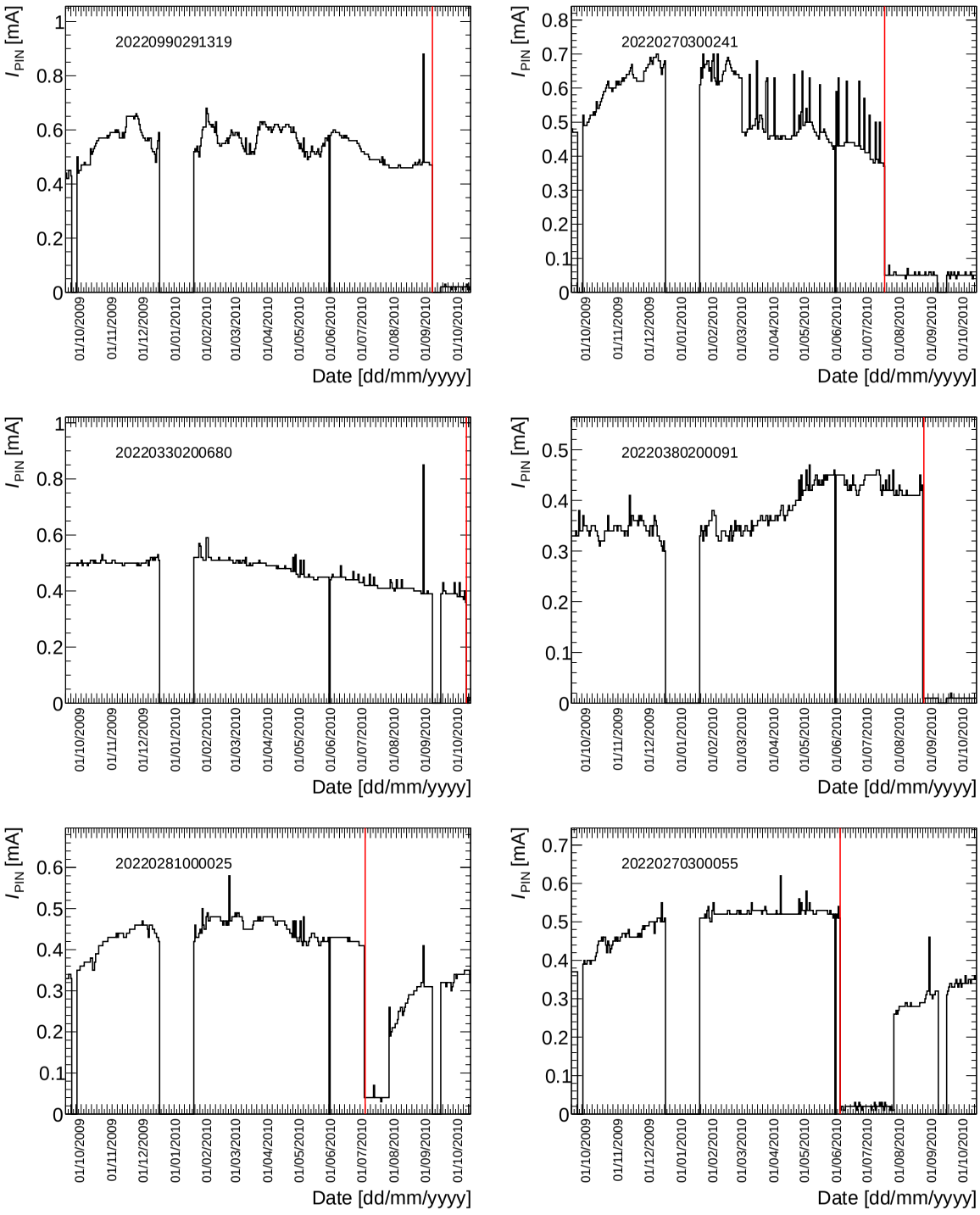

Figure 10.6: The I_{PIN} evolution over time of a randomly selected set of six channels with failures between September 18$^{\mathrm{th}}$ 2009 and October 14$^{\mathrm{th}}$ 2010. The relevant serial number of the on-detector modules are also indicated and the red line indicates the time at which the failure was registered.

20220270300241, but it is unclear if this can be associated with the failure of a particular link.

10.3.5 Failure rates

The monitoring of the rate at which optical links fail is clearly an important factor in the long term maintenance of the system. It is possible to use the threshold failure definition to find the number of failed links on each day. These daily failures can be combined into a rate monitoring method, either by looking at the number of failures per some period of time or by the cumulative number of failures. The failure rate per week is shown in Figure 10.7.

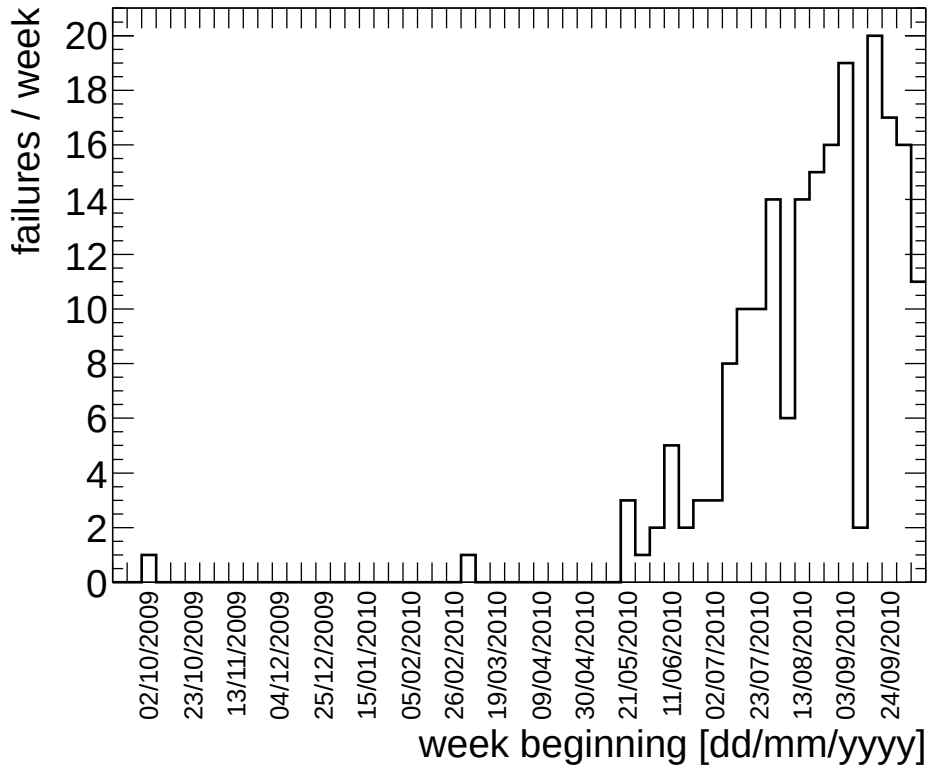

Figure 10.7: The optical link failure rate per week between September 18$^{\text{th}}$ 2009 and October 14$^{\text{th}}$ 2010.

From the evolution of the failure rate it is clear that the SCT Tx system has gone through two different phases over this period of time. Throughout 2009 and early 2010 the system was quite stable, with very few failures. However, from May 2010 the failure rate began to increase at a considerable rate. Over the course of the following three months the failure

rate peaked at 20 links per week. This is clearly not a sustainable rate for a system of 4088 links that is expected to be in operation for the most part of 10 years. Fortunately the redundancy system can operate to reduce the stress from these failures in the short term. In addition to this, a long term phase of replacement of arrays, in which links that could no longer use the redundancy were present, was established. However, this is an expensive process and relies on enough replacement arrays being available. Therefore, it is of interest to know how the failure rates are expected to evolve.

The long term evolution of the failure rates can be monitored by the cumulative number of deaths observed in the system. This is only trivially valid for periods where the number of replacements are small, as introducing new modules will affect the observed shape of this distribution and so change the predicted lifetime of the modules. The period discussed in this Chapter is chosen for that particular reason and so replacement rate is sufficiently small for replacements to be a negligible effect. In the future it must be monitored by splitting the failures into individual streams according to the type of array installed.

Predicting the long term failure rate requires implementing some model that can be used to describe the failure process. The cumulative number of failures of the system is considered over time and is represented by a log-normal distribution. The log-normal distribution is a common choice for analysing VCSEL lifetime data, for example [142], as it has emprically been seen to give a good description of the data in such studies. This assumes that the total number of failures is sufficiently large to constrain the input log-normal distribution. The log-normal pdf is related to the normal distribution by a transform of variables onto logarithmic coordinates and is given by

$$f(x|\mu,\sigma) = \frac{1}{x\sigma\sqrt{2\pi}} e^{-\frac{(\ln(x)-\mu)^2}{2\sigma^2}}; \quad x > 0, \tag{10.1}$$

where μ is known as the location parameter and σ is the scale parameter. These are related to the mean and standard deviation, here referred to as m and s for ease of notation, by

$$m = e^{\mu+\sigma^2/2}; \tag{10.2}$$

$$s = \sqrt{(e^{\sigma^2}-1)e^{2\mu+\sigma^2}}. \tag{10.3}$$

The parameters of the log-normal model describing the individual link failures can be extracted by fitting the model to the observed cumulative distribution of failures. This requires knowing the cumulative distribution of failures expected if the probability of each link failure is described by a log-normal distribution. The log-normal cumulative distribution is given by

$$F(x|\mu,\sigma) = \frac{N}{2}\mathrm{erfc}\left[-\frac{\ln(x)-\mu}{\sigma\sqrt{2}}\right], \tag{10.4}$$

where N is the number of links in the SCT and erfc defines the complementary error function

$$\mathrm{erfc}[x] = \frac{2}{\sqrt{\pi}}\int_x^\infty e^{-t^2}\mathrm{d}t. \tag{10.5}$$

The observed cumulative distribution and the result of the fit are shown in Figure 10.8. This also gives the projected cumulative distribution of the Tx link failures in the case where the redundancy works for all failures and no replacements are required. Note that these assumptions mean that, in reality, the failure rate will deviate from this prediction when new VCSEL arrays are introduced into the system. In any case, it is interesting to find how long a given module can be expected to be used before it will fail. To remove the discontinuities from shut down periods the cumulative distribution only includes measurements from days where the SCT was active.

The fit result corresponds to a MTTF for a given module of approximately 650 active days, with a standard deviation of 164 days. These values indicate that a large proportion of the links will need to be replaced within two years of active running. The SCT is expected

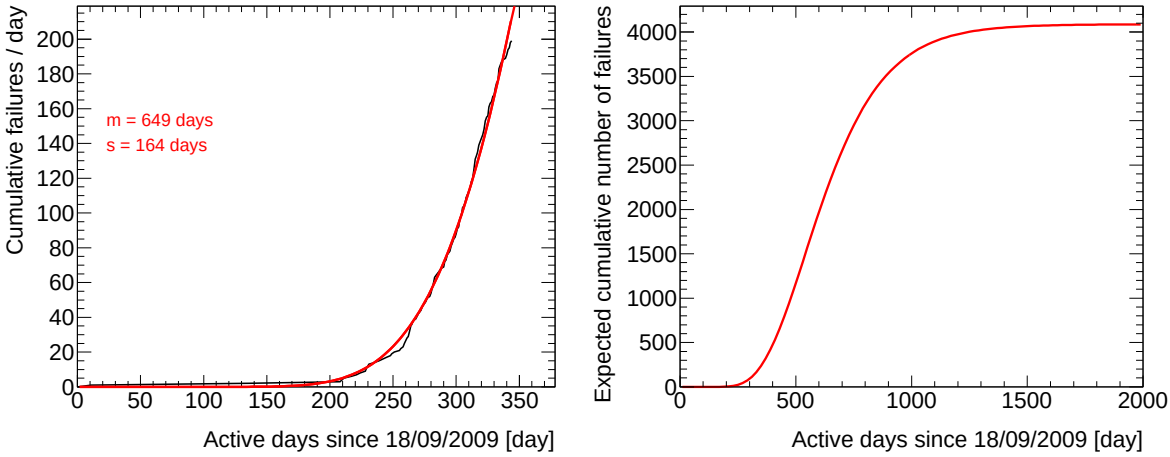

Figure 10.8: The cumulative link failures between September 18th 2009 and October 14th 2010 (left) and the projection of the fit for 2000 days of active running (right).

to run for up to 10 years, with occasional periods of shut down during that time. Therefore, it is clear that preparations should be made for a large scale replacement of the off-detector VCSEL arrays. Note that each array consists of 12 links and so the current population of VCSELs will be rapidly depleted.

In order to make well informed decisions relating to the production of replacement VCSELs it was important to know if there were any clear causes of the failures. This was investigated by searching for correlations between the environment and the failure rates of the links.

10.3.6 Locations of the failures

One potential source of correlations between link failures is the locations in which they have been installed. Any positive correlations between location and failure may point towards an environmental cause. It is also of interest to consider the batches in which the VCSELs were produced. A correlation in batch between failures may indicate that the cause of the failures originates in their production. Due to the SCT geometry, different numbers of VCSELs can be active on a given array. Correlations between the number of active channels on an array may give indications towards problems in the operation of the VCSELs that may contribute towards the failures.

A set of different hypothesis tests were performed in order to search for these correlations. These hypothesis tests looked for correlations due to on-detector location, off-detector crate location, production batch and number of active channels on the array. Quantitative evaluation of the correlations were performed by defining a null hypothesis of flat channel failure probability. This hypothesis was tested using a χ^2 method, which involves predicting the χ^2 pdf corresponding to the difference between the hypothesised model and the observed distribution of failures. The χ^2 value for a given histogram involves calculating the sum of deviations over bins

$$\chi^2 = \sum_{\text{i}\in\text{bins}} \left(\frac{n_i - \nu_i}{\sigma_i} \right)^2, \tag{10.6}$$

where the index i gives the location of the bin, n_i is the observed number of failures in that bin, ν_i is the predicted number of failures in that bin and σ_i is the error on the prediction in that bin. The value of ν_i is determined by the number of channels in a given location scaled by the fraction of the total number of powered links that have failed in the system. The error on this is assumed to be Poisson distributed, such that $\sigma_i = \sqrt{\nu_i}$. The p-value is extracted for each hypothesis according to the χ^2 distribution expected for the number of degrees of freedom of that particular hypothesis.

The observed failure rates and corresponding predictions for each of these tests are given in Figure 10.9.

None of the tested distributions have large p-values, and so the even failure rate hypothesis is rejected. This means that the failures are not evenly distributed throughout the system and as such it is likely that there is some affect that depends on location that contributes to the failure rates. These results imply that the evolution of failure rates, predicted in Figure 10.8, samples failures from more than one population of links. These different populations will have different failure rates and so have different mean failure times. Also, it appears that there may be some underlying cause to the failures. However, it is hard to say conclusively that any particular scenario contributes exclusively to the link failures. Each distribution shows

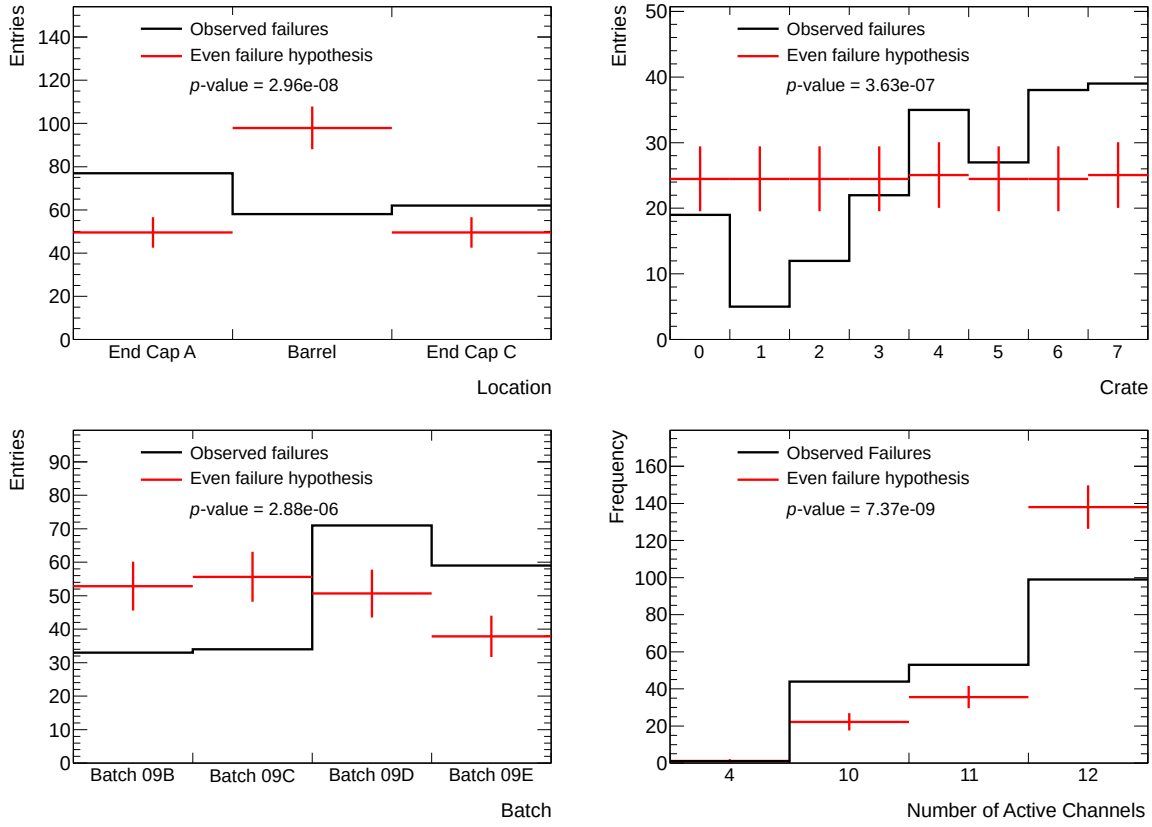

Figure 10.9: Failure rates as functions of on-detector location (top-left), off-detector crate location (top-right), production batch (bottom-left) and number of active channels on the array (bottom left). The rates are measured between September 18$^{\text{th}}$ 2009 and October 14$^{\text{th}}$ 2010.

a small p-value, and many distributions are correlated by eg. the mapping of off-detector crates to on-detector modules. An important hint, which can be investigated further, is that the end-cap crates (4, 5, 6 and 7) tend to have experienced more failures than predicted, while the barrel crates (0, 1, 2 and 3) have experienced fewer than expected. Measuring other quantities that change according to crate location may result in a positive correlation.

10.3.7 Humidity effects

One example of an environmental condition that may vary from crate to crate is the humidity. To investigate if this is a potential contributing factor to the failure rates, hand-held humidity probes were used to measure the relative amount of moisture in the air at each crate. The results from these measurements taken close to the VCSEL arrays can be seen in Figure 10.10.

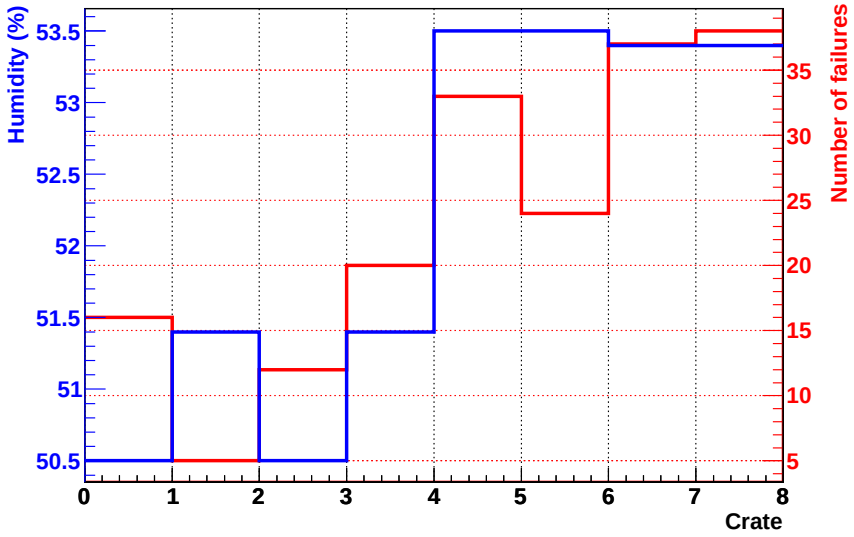

Figure 10.10: The optical link failure rate per crate with the measured humidity at the back of the crate for October 6th 2010.

This indicates that crates that have higher failure rates also have higher humidity, by two to three per cent. Humidity damage may cause dark lines to form due to depletion of the Ga in the GaAs layers within the VCSELs. These can grow and may cause the VCSEL to fail [143]. As a result of this apparent correlation between humidity and failure rate, new productions of VCSELs that were installed from the Summer of 2011 have humidity protection.

Part IV

Conclusions

Chapter 11

Conclusions

11.1 Conclusions of the search for supersymmetry

The SUSY search presented in this thesis showed that it is possible to gain better precision in a SUSY search by building the statistical model using binned kinematic shape information in a set of control and signal regions. This statistical model was used to constrain nuisance parameters and extract the signal strength for either particular theoretical models or in a model-independent sense. The control regions were selected in such a way that the dominant processes were either W+jets or $t\bar{t}$, which allowed these backgrounds to be estimated in a partially data-driven manner. The results of these background estimates were then used to constrain the expected number of events in the signal regions.

Limits were set at the 95% confidence level by using a profile log-likelihood ratio test statistic and the CL_s metric. Two grids of signal points were considered.

In the MSUGRA case, regions of the slice in parameter space ($\tan\beta = 10,\ A_0 = 0,\ \mu > 0$) considered with $m_{\tilde{q}} = m_{\tilde{g}} < 1200$ GeV were found to be excluded. For the grid as a whole, squark masses below 1100 GeV and gluino masses below 800 GeV are excluded.

For the Simplified SUSY Model, gluino masses below 900 GeV are excluded for LSP masses below 250 GeV. Low cross sections, down to 20 fb, are excluded in the bulk of the

grid while large cross sections, above 100 pb, are required to exclude points where the LSP mass is close to the gluino mass.

Model-independent limits were also set. These found that any theoretical model with an observable cross section of $\langle \epsilon\sigma \rangle > 1$ fb is excluded at the 95% confidence level in the tight signal regions, with explicit $m_{\text{eff}}^{\text{inc}}$ cuts.

11.1.1 Context of results

Various results from ATLAS and CMS were released for their full 2011 datasets. The results from the official ATLAS one lepton analysis [101], in which the author participated, as well as those presented in this thesis, improved dramatically on the results of mid-2011 [107]. Of course a large reason for this improvement is the increased size of the dataset, but it is also interesting to compare the improvement with respect to the other SUSY analyses.

The analysis presented in this thesis excludes comparable, but slightly lower, values of $m_{1/2}$ with respect to the ATLAS analyses with no leptons with many jets [144] and no leptons with moderate jet selections [145] at high m_0 in the MSUGRA grid. However, the analysis in this thesis excludes higher values of $m_{1/2}$ at low m_0 when compared to the no lepton with multiple jets search. The analysis with no leptons and moderate jet selections excludes larger values of $m_{1/2}$ than the analysis presented in this thesis.

The CMS collaboration released three SUSY searches with one lepton and jets in the final state for their full 2011 dataset: a neural network based analysis [146]; a template based analysis [147]; and an analysis that uses the lepton spectrum and lepton projection methods [148]. The analysis presented in this thesis performs similarly or better than all of the CMS analyses at values of $m_0 < 1600$ GeV for both expected and observed limits on $m_{1/2}$. At values of m_0 above 1600 GeV, the analysis presented here excludes higher values of $m_{1/2}$ than all of the individual CMS analyses with one lepton and jets in the final state.

Squark and gluino masses at around 1 TeV are being probed by SUSY searches at the LHC. This makes it particularly hard to create a natural SUSY model as a minimal ex-

tension to the SM while fulfilling the role of the Higgs in EWSB. So called 'naturalness' arguments insist that if the amount of fine-tuning of the SUSY parameters is required to be low, then SUSY can be expected to exist only in particular regions of parameter space, see for example [149]. Taking the most likely values of the Higgs mass into account, the favoured LSP has a small higgsino component and the squarks are heavy. This corresponds to MSUGRA points with $m_0 > 2000$ GeV and $m_{1/2} > 250$ GeV. Current experimental limits from the LHC enter into this region but do not cover all points. However, DM searches using underground experiments to measure the DM-nucleon cross section also exclude points in this favoured region. This means that the favoured parameter space for SUSY has already been squeezed, though anticipated increases in the luminosity and energy of the LHC are required to probe much of the remaining phenomenologically interesting space.

11.1.2 Potential extensions

The analysis presented in this thesis considered high p_{T} electrons and muons. This was mostly driven by requirements of using a leptonic trigger. However, high p_{T} requirements on objects mean that the analysis loses efficiency for scenarios where the mass differences of SUSY particles in the cascades are small. For this reason, the Simplified SUSY Model results presented here are much more sensitive to the bulk of parameter space than to the diagonal with $m_{\mathrm{LSP}} \sim m_{\tilde{g}}$. One possible way of increasing sensitivity towards the diagonal is to include low p_{T} lepton acceptance by, for example, using a $E_{\mathrm{T}}^{\mathrm{miss}}$ trigger. Additional control and signal regions can be added to the simultaneous fit in this analysis to broaden sensitivity. A low p_{T} lepton study was included in [101] and was indeed found to have increased sensitivity towards the diagonal.

Another extension would be to include additional leptonic regions. For example, if two leptons are included then a control region can be formed for the Z+jets background estimate and the p_{T}^{Z} spectrum can be measured. The inclusion of binned information from the p_{T}^{Z} spectrum could remove the requirement of the p_{T}^{W} reweighting scheme that was used in this analysis. This would also allow further regions of signal parameter space to be explored by

increasing sensitivity to theoretical models with neutralinos in the cascade.

In generating the analysis for this thesis, and for the official single lepton ATLAS SUSY search, a tool for generating and analysing generic binned statistical models was created. This means that future ATLAS analyses will be able to easily implement the shape-based analysis that this thesis has demonstrated.

11.2 Conclusions of the pileup study

A study was presented that investigated the effects of pileup on the 1.04 fb^{-1} ATLAS SUSY search with one lepton. Two aspects of these effects were looked into. The first effect resulted from the need to reweight the number of interactions in the MC samples to the distribution of the number of interactions observed in data. The direct effect of the additional interactions on the selections involved in the analysis was also studied.

It was shown that pre-simulation of the number of interactions requires a reweighting function to be applied to the MC samples after the final observed dataset has been produced. This reweighting function has a large number of zero weights, which means that a large proportion of MC events are thrown away - increasing the statistical uncertainty from the MC samples. The N_{int} reweighting scheme was introduced as a means of estimating the actual number of events in each event by convoluting a set of Poisson distributions with mean values given by the $\langle\mu\rangle_{\text{LB,BCID}}$ in each bin. The N_{int} scheme showed the lowest statistical uncertainty, with only a small effect on the central value of the expected number of events.

The direct impact of pileup on the analysis was assessed by considering how the acceptance changed with the number of vertices in the W+jets an $t\bar{t}$ control regions. It was shown that the original jet definition resulted in an increasing acceptance with number of vertices in the W+jets control region, while the $t\bar{t}$ control region was rather flat. The increasing acceptance in the W+jets control region was attributed to additional events passing the jet selection as jets from pileup were being counted. The jet vertex fraction was introduced to assign jets to be from pileup if less than 75% of their track p_{T} was from the highest sum p_{T}

vertex. By applying this jet vertex fraction cut to the jets in the final stage of the analysis it was shown that the rise in acceptance in the W+jets control region could be controlled.

11.3 Conclusions of the optical links monitoring

In order for ATLAS to produce high quality results it is necessary to maintain good performance for all of the component detectors. This involves monitoring the performance of the ability of these detectors to communicate information to and from the detector. In the case of the SCT this communication is performed by converting electrical signals into light, sending the light down a fibre, and then converting the light back to an electrical signal.

The results of the monitoring of this system were presented, based on a search for failures of these links. It was shown that a population of failed links could be found by counting links that fell below a threshold of $I_{\mathrm{PIN}} - I_{\mathrm{ped}} < 0.05$ mA. This threshold was used to identify failed links and the time that they failed. By accumulating information about these failures over time it was then possible to investigate the evolution of these failures. The future failure rate was predicted by performing a fit to a log-normal distribution and the mean time to failure was found to be about 650 days for a given link. This meant that a large number of links would have to be replaced in the relatively short term, compared to the expected lifetime of the SCT.

An investigation was then performed to search for correlations between the failures and their environment. Initially a statistical test was performed against a hypothesis of equal failure likelihood across all links in the system. This was found to be an unlikely scenario for the failures, which was interpreted as there being some environmental dependence of the failure rates. By measuring the humidity in different regions of the off-detector components of the SCT, a reasonable correlation between distribution of failures and the humidity was observed. Therefore, future productions of the lasers that send light to the on-detector modules will be made with humidity protection.

Part V

Appendices

Appendix A

Statistical techniques

A.1 Performing the fit

Having constructed the desired statistical model, for example as described in Chapter 7, the initial fit is then performed within `RooFit` [150]. This fit maximises the likelihood corresponding to the probability constructed in Equation (7.7). The likelihood has the same functional form as Equation (7.7), but rather than asking 'If I fix the statistical model parameters to certain values, at what rate in a set of experiments will I measure this particular histogram' we ask 'If I observe this particular histogram, what are the set of statistcal model parameters that are most likely to reproduce my result'. This is equivalent to the transformation $\mathcal{P}(n_{cb}, a|\phi, \alpha) \rightarrow \mathcal{L}(\phi, \alpha|n_{cb}, a)$. The total number of events in the statistical model are also allowed to vary according to the relevant Poisson distribution during the fitting process.

The statistical model can have a large number of parameters, but we are essentially only interested in one - the signal strength μ, which is defined as the parameter of interest. All of the other parameters are necessary to build the statistical model but their result is not what we are interested in when the fit has been performed - all parameters apart from μ are defined as nuisance parameters, which will be denoted θ. In this formulation, the likelihood becomes $\mathcal{L}(\mu, \theta|n_{cb}, a)$, or to write this with the measured parameters implicitly fixed, $\mathcal{L}(\mu, \theta)$.

The best-fit values for the statistical model parameters are obtained by maximising this likelihood function, or rather minimising the negative logarithm of the likelihood. This is done in such a way as to handle correlations between the model parameters and propagate the uncertainties through the fit. The resulting best fit parameters are known as maximum likelihood estimators, and are denoted $\hat{\mu}$ and $\hat{\theta}$. It is possible to extract the fitted yields of the different SM processes, and the errors on these values, in order to test the performance of this method in various regions of phase space.

A.2 The profile log-likelihood ratio test statistic

We now wish to evaluate the agreement between the observed data and various constructions of our statistical model. This involves evaluating what is known as a test statistic for the fit to observed data and then finding the pdf that this quantity would be expected to follow for a large number of experiments. Therefore, the test statistic pdf will allow us to evaluate the probability that a future experiment will observe a value of the test statistic that is less consistent with the model via a random process, rather than the model being false. If the resulting probability from this test is low then it is likely that the model that has been tested is incorrect. This is known as hypothesis testing and will be discussed further in the next Section.

The test statistic used in this analysis is known as the profile log-likelihood ratio. This is derived from the profile likelihood ratio,

$$\lambda(\mu) = \frac{L\left(\mu, \hat{\hat{\theta}}\left(\mu\right)\right)}{L\left(\hat{\mu}, \hat{\theta}\right)}, \tag{A.1}$$

where $\hat{\hat{\theta}}(\mu)$ is the set of maximum likelihood estimators for any value of μ, called conditional maximum likelihood estimators. The value of $\hat{\mu}$ is forced to be positive within the statistical model, so that only physical regions are tested. Note that the profile likelihood ratio is unity when the tested signal strength, μ, is the same as the best fit to μ as a free parameter, while

the ratio tends to zero if the tested value of μ is far from the best fit with free μ.

The profile log-likelihood, q_μ, follows:

$$q_\mu = \begin{cases} -2\ln\lambda(\mu) & \hat{\mu} \leq \mu; \\ 0 & \hat{\mu} > \mu, \end{cases} \tag{A.2}$$

where the negative two is used here so that one unit of $\sqrt{q_\mu}$ corresponds to a one standard deviation shift of μ away from $\hat{\mu}$. The property of the profile log-likelihood representing one unit of standard deviation follows from the Wald approximation [151] for a single parameter of interest

$$-2\ln\lambda(\mu) = \frac{(\mu-\hat{\mu})^2}{\sigma^2} + \mathcal{O}\left(1/\sqrt{N}\right). \tag{A.3}$$

Note that this approximation is only valid in the limit of large N, where N is the number of observed events in the statistical model.

In attempting to exclude particular theoretical models, the requirement of $\hat{\mu} \leq \mu$ is made so that particular signal values are only tested if the tested signal strength must be reduced to be consistent with the statistical model. For this reason, the test statistic is referred to as being 'one-sided'.

Having determined the form of the test statistic, we must find how our model would expect that test statistic to be distributed for a set of independent future measurements. Let us define the distribution of this test statistic as $f(q_\mu|\mu', \hat{\hat{\theta}}(\mu'))$. Note that this requires defining the assumed signal strength, μ', which is unity when testing a nominal theoretical model, zero when testing the background-only hypothesis, or can float to investigate model-independent cross sections. The value of μ is now the distinct hypothesised signal strength that is being tested. The form of this distribution can either be found numerically by using MC toy experiments or, in the limit of large numbers of observed events, by using analytical solutions.

A.2.1 Finding the test statistic distribution using toy Monte Carlo

The most general way to produce $f(q_\mu|\mu', \hat{\hat{\theta}}(\mu'))$ is to generate a large ($\mathcal{O}(1000)$) set of pseudo-experiments, known as toy MC. Each of these pseudo-experiments represents a possible future experiment, given a fixed value of the assumed signal strength. The values of $\hat{\hat{\theta}}(\mu')$ are be taken from a fit to the observed data, with the fixed signal strength μ'. The auxiliary measurements, a, for each pseudo-experiment are drawn from the resulting pdf for each parameter, $\hat{\hat{\theta}}(\mu')$. Each pseudo-experiment is treated as the observed data were in the previous Section in order to generate a set of q_μ values from which $f(q_\mu|\mu', \hat{\hat{\theta}}(\mu'))$ is built.

A.2.2 The asymptotic approximation

In the limit of a large observed dataset, it is possible to find an approximate form for $f(q_\mu|\mu', \hat{\hat{\theta}}(\mu'))$ analytically. This makes use of both the Wald approximation, Equation (A.3) and the results of Wilks [152], which say that the profile log-likelihood ratio has the form of a χ^2 distribution with one degree of freedom. Therefore, $f(q_\mu|\mu', \hat{\hat{\theta}}(\mu'))$ is independent of the nuisance parameters and takes the form described in [153],

$$f(q_\mu|\mu') = \Phi\left(\frac{\mu'-\mu}{\sigma}\right)\delta(q_\mu) + \frac{1}{2\sqrt{2\pi q_\mu}}\exp\left[-\frac{1}{2}\left(\sqrt{q_\mu} - \frac{\mu-\mu'}{\sigma}\right)^2\right], \tag{A.4}$$

where Φ corresponds to the Gaussian cumulative distribution.

In order to use this equation the variance of $\hat{\mu}$, denoted σ, must be evaluated. This is done by calculating the profile likelihood ratio for the dataset that returns the true parameter values, known as the Asimov dataset. Essentially this corresponds to a set of histograms with one event in each bin that is weighted to correspond to the exact value of the input model in that bin. The variance on $\hat{\mu}$ is extracted from this dataset by evaluating the covariance matrix numerically according to [153].

We are actually interested in the cumulative distributions that are derived from these

probability distributions. The rate at which a series of future experiments would be expected to observe values of the test statistic that are less compatible with the model corresponds to the integral of the test statistic distribution from the observed value of q_μ to infinity in the direction away from the mean of the distribution. This is known as a one-sided hypothesis test, which will be discussed in more detail in the next Section. Suffice it to say that the probability that a future experiment will agree less well with the current observation is the value of the cumulative distribution subtracted from one. The cumulative distribution corresponding to the pdf in Equation (A.4) is

$$F(q_\mu|\mu') = \Phi\left(\sqrt{q_\mu} - \frac{\mu - \mu'}{\sigma}\right). \tag{A.5}$$

A.3 Testing specific hypotheses

Now that the test statistic distribution has been determined, we can come to the second question posed in Section 7.1. This is done by performing a hypothesis test. The signal strength parameter is set to some non-zero value and the integral of the test statistic distribution from the observed value to either infinity or negative infinity is calculated. The choice of the side of the distribution to integrate over is defined such that the final integral is less than a half. This corresponds to the probability that a future experiment will make an observation that agrees less well with the model than the current observation, and is known as a p-value. Therefore, a low p-value means that the chance of a future experiment measuring worse agreement with the model is low and so either the model is not true or the current experiment was just very unlucky.

Let us now define a hypothesis, where the specific signal model is assumed to be true, so $\mu = 1$. We shall refer to the p-value result of the test on this hypothesis as $p_{\mathrm{s+b}}$ as this tests the signal plus background hypothesis. The result of the hypothesis test is then

$$p_{s+b} = \int_{q_{1,\mathrm{obs}}}^{\infty} f\left(q_1|\mu' = 1, \hat{\hat{\theta}}(1, \mathrm{obs})\right) \mathrm{d}q_1. \tag{A.6}$$

If a particular model has a p-value less than 0.05 it is said to be excluded at the 95% confidence level. This means that there is less than a one in twenty chance that the model will be found by any future experiment.

The $p_{\mathrm{s+b}}$ metric for evaluating a particular hypothesis works well for signal models where large numbers of events are expected, if that model is true. However, consider the case where only only a very small fraction of the total expected events are from signal. As we are considering a 95% confidence level exclusion, downward statistical fluctuations in the data will mean that every one in twenty points tested with this property will be excluded, despite having no experimental sensitivity.

To prevent such cases of false exclusion, we can consider penalising model points for which the experimental sensitivities are low. First we define a measure that the observation is consistent with the background-only hypothesis, given that we observe a particular $q_{1,\mathrm{obs}}$ value

$$p_b = 1 - \int_{q_{1,\mathrm{obs}}}^{\infty} f(q_1|\mu' = 0, \hat{\hat{\theta}}(0, \mathrm{obs}))\mathrm{d}q_1. \tag{A.7}$$

The hypothesis test defined in Equation (A.6) can then be modified by a comparison between the probability that the signal plus background hypothesis is valid and the probability that the background-only hypothesis is not valid. This results in

$$\mathrm{CL}_s = \frac{p_{s+b}}{1 - p_b}. \tag{A.8}$$

The results of this analysis are presented according to this CL_s value, rather than p_{s+b} to ensure that it is protected from potential false exclusions. However, it should be noted that CL_s is not a true p-value, but will always give conservative results compared to p_{s+b} as

$1 - p_b < 1$.

Note that the above equations correspond to cumulative distributions. Therefore, in the asymptotic limit we can write $p_{s+b} = 1 - F\left(q_1|\mu' = 1\right)$ and $1 - p_b = 1 - F\left(q_1|\mu' = 0\right)$. These correspond to important simplifications of Equation (A.5)

$$p_{s+b} = 1 - F\left(q_1|\mu' = 1\right) = 1 - \Phi\left(\sqrt{q_1}\right), \tag{A.9}$$

and

$$1 - p_b = 1 - F\left(q_1|\mu' = 0\right) = 1 - \Phi\left(\sqrt{q_1} - \frac{1}{\sigma}\right) = \Phi\left(\frac{1}{\sigma} - \sqrt{q_1}\right). \tag{A.10}$$

Using the Wald approximation, and noting that the Asimov dataset gives $\hat{\mu} = \mu'$, it is possible to determine an estimate of σ in terms of the test statistic q_μ. Setting $\hat{\mu} = \mu'$ in Equation (A.3), with $q_\mu = -2\ln(\lambda)$ we have

$$q_{A,\mu} = \frac{(\mu - \mu')^2}{\sigma_A^2}, \tag{A.11}$$

where the subscript, A, shows that the Asimov dataset has been used. For the case where a background-only sample is assumed, this gives

$$\sigma_{A,\mu}^2 = \frac{\mu^2}{q_{\mu,A}}. \tag{A.12}$$

Setting the hypothesis $\mu = 1$ in this allows the denominator of CL_s to be simplified even further to

$$1 - p_b = \Phi\left(\sqrt{q_{1,A}} - \sqrt{q_1}\right), \tag{A.13}$$

so that, in the asymptotic limit, CL_s can be written as

$$\mathrm{CL}_s \simeq \frac{1 - \Phi\left(\sqrt{q_1}\right)}{\Phi\left(\sqrt{q_{1,A}} - \sqrt{q_1}\right)}. \tag{A.14}$$

A.3.1 Testing grids of signal points

In physics analyses that sample from large parameter spaces, such as SUSY, it is common to quantify the sensitivity of a particular analysis by sampling a grid of points corresponding to a 2D slice through that parameter space. Examples of such grids were introduced in Section 5.3. The hypothesis testing procedure is then repeated for all of the points on the grid and, in the case of this analysis, the CL_s value for each point is obtained. These points are then grouped if they have $\mathrm{CL}_s < 0.05$. A line is then drawn around all of the points that are excluded at the 95% confidence level according to CL_s to represent the boundary between excluded regions of phase space and regions of phase space to which the analysis does not have sufficient sensitivity for exclusion.

A.4 Setting model-independent upper limits

Finally we can address the third question posed in Section 7.1. As well as testing the analysis against specific models, it is also of interest to determine what other values of μ' are still allowed by the analysis, assuming that data are consistent with the background-only hypothesis. This can be done using a technique called hypothesis test inversion. Rather than testing a single specific value of the signal strength, for example $\mu = 1$ as in the previous Section, it is possible to scan across values of μ and perform a hypothesis test at each point. Now, instead of asking the question 'What is the chance that a future experiment will observe a value of q_μ that is less consistent with the model when compared to our current observation?', we ask 'What range of values of μ are unlikely to be observed by a future experiment?'. The procedure is similar to the hypothesis testing, but a set of CL_s values are produced. It is then possible to interpolate between these values, provided the set is large enough, and find the point at which the CL_s value for μ crosses the 0.05 line. All values of

μ that are greater than that found by the line-crossing are then said to be excluded.

A.5 Finding the median exclusion and error bands

Having either determined the observed exclusion range for a specific model or the observed model-independent excluded values of μ, it is then appropriate to compare these to the exclusion expected from the background-only model. As was the case for finding the test statistic distribution, it is possible to extract the expected exclusion either from MC toys, or from analytical approximations.

A.5.1 Expected limits from toys

When generating the expected limits from toys, a set of pseudo-experiments are produced according to the background-only hypothesis, with $\mu = 0$ and $\hat{\hat{\theta}}(0, \text{obs})$. Let us call this new dataset $\{\text{data}'\}$. The procedures for hypothesis testing and limit setting are then repeated on $\{\text{data}'\}$, by replacing the observed dataset with these pseudo-experiments.

First, the values of $\hat{\hat{\theta}}(\mu, \text{data}')$ are found. These conditional maximum likelihood estimators are then used to form the test statistic distributions $f\left(q_\mu|\mu, \hat{\hat{\theta}}(\mu, \text{data}')\right)$. The CL_s results for each data$'$ are then extracted and histogrammed. The median of this histogram gives the median expected limit for that particular test, while the CL_s values that give the thresholds for integrals giving one-sided 1σ and 2σ deviations give the CL_s values at 1σ and 2σ, respectively.

For the case of hypothesis tests over grids of theoretical model points, the median expected 95% confidence level band is defined as containing all of the points for which the median expected CL_s value is less than 0.05. Usually the 95% confidence level 1σ bands are also shown. These correspond to the points where the 1σ CL_s threshold on the respective side of the distribution is less than 0.05.

The model independent upper limits are treated in a similar way. The 95% confidence

level median expected limit in this case is the value of μ for which the median expected CL_s value is less than 0.05. Also, the 1σ uncertainty on this expected limit is given by the value of μ for which the 1σ CL_s threshold on the relevant side of the distribution is less than 0.05.

A.5.2 Expected limits using asymptotic approximations

In cases where the asymptotic approximation is used, the median expected 95% confidence level limit and its error bands can be estimated analytically. This is performed using the Asimov dataset, which, as mentioned before, is the dataset that gives the best representation of the model in hand. Replacing the observed data with the Asimov dataset in Equation (A.14) gives

$$\mathrm{CL}_s^{\mathrm{exp}} \sim \frac{1-\Phi\left(\sqrt{q_{\mu,A}}\right)}{\Phi\left(\sqrt{q_{\mu,A}}-\sqrt{q_{\mu,A}}\right)} = 2\left(1-\Phi\left(\sqrt{q_{\mu,A}}\right)\right), \tag{A.15}$$

where $\Phi(0) = 0.5$ has been used.

The expected $n\sigma$ fluctuations are found by noting that the Wald approximation suggests that a unit shift in $\sqrt{q_\mu}$ corresponds to a shift of σ from the nominal value of μ. Therefore, we can shift the value of $\sqrt{q_\mu}$ by n and then replace the observed test statistic with that found by the Asimov dataset. In this way the expected uncertainty bands can be found by

$$\mathrm{CL}_s^{\mathrm{exp}+n} \sim \frac{1-\Phi\left(\sqrt{q_{\mu,A}}+n\right)}{\Phi\left(-n\right)}. \tag{A.16}$$

Appendix B

Fit results

B.1 Background-only fit result

The result of the background-only fit is shown below and the corresponding correlation matrix is given in Figure B.1. These results are discussed in Section 8.1.

```
RooFitResult: minimized FCN value: -203247, estimated distance to minimum: 0.00104409
              covariance matrix quality: Full, accurate covariance matrix
              Status : MIGRAD=0 HESSE=0

  Floating Parameter    FinalValue +/-  Error
--------------------  --------------------------
            alpha_BT    2.4615e-01 +/-  6.97e-01
           alpha_EER    1.0859e-04 +/-  9.91e-01
           alpha_EES   -2.3763e-03 +/-  9.93e-01
  alpha_KtScaleTTbar    3.5910e-01 +/-  6.69e-01
  alpha_KtScaleWjets    6.5999e-02 +/-  6.29e-01
           alpha_LE    3.8683e-03 +/-  9.92e-01
           alpha_MC    2.2215e-02 +/-  9.44e-01
          alpha_MID   -1.3405e-03 +/-  9.92e-01
          alpha_MMS    4.0567e-03 +/-  9.91e-01
           alpha_MP    3.5709e-03 +/-  9.84e-01
   alpha_PtMinTTbarC   -1.8822e-01 +/-  9.49e-01
   alpha_PtMinWjetsC    2.5358e-02 +/-  8.24e-01
alpha_QCDNorm_TR_nJet    1.1084e-01 +/-  8.49e-01
alpha_QCDNorm_WR_nJet   -5.5061e-02 +/-  7.81e-01
            alpha_TE    2.8065e-02 +/-  5.25e-01
            alpha_WP    1.9047e-02 +/-  1.03e+00
      gamma_JT_bin_0    1.0439e+00 +/-  6.59e-02
      gamma_JT_bin_1    1.0160e+00 +/-  7.26e-02
      gamma_JT_bin_2    9.6195e-01 +/-  6.86e-02
```

```
        gamma_JT_bin_3    9.5805e-01 +/-  8.12e-02
        gamma_JT_bin_4    8.5036e-01 +/-  9.77e-02
        gamma_JT_bin_5    8.9481e-01 +/-  1.42e-01
        gamma_JT_bin_6    1.0974e+00 +/-  2.30e-01
        gamma_JW_bin_0    9.9309e-01 +/-  1.25e-01
        gamma_JW_bin_1    9.8123e-01 +/-  1.01e-01
        gamma_JW_bin_2    1.0027e+00 +/-  8.84e-02
        gamma_JW_bin_3    9.6587e-01 +/-  9.32e-02
        gamma_JW_bin_4    9.8607e-01 +/-  1.18e-01
        gamma_JW_bin_5    9.7519e-01 +/-  1.70e-01
        gamma_JW_bin_6    1.1283e+00 +/-  2.16e-01
gamma_stat_TR_nJet_bin_0    1.0007e+00 +/-  1.09e-02
gamma_stat_TR_nJet_bin_1    1.0002e+00 +/-  1.11e-02
gamma_stat_TR_nJet_bin_2    9.9992e-01 +/-  6.87e-03
gamma_stat_TR_nJet_bin_3    9.9991e-01 +/-  8.69e-03
gamma_stat_TR_nJet_bin_4    9.9958e-01 +/-  1.47e-02
gamma_stat_TR_nJet_bin_5    9.9900e-01 +/-  2.83e-02
gamma_stat_TR_nJet_bin_6    1.0021e+00 +/-  5.08e-02
gamma_stat_WR_nJet_bin_0    9.9998e-01 +/-  7.20e-03
gamma_stat_WR_nJet_bin_1    9.9994e-01 +/-  8.22e-03
gamma_stat_WR_nJet_bin_2    1.0000e+00 +/-  1.05e-02
gamma_stat_WR_nJet_bin_3    9.9984e-01 +/-  1.36e-02
gamma_stat_WR_nJet_bin_4    9.9969e-01 +/-  3.00e-02
gamma_stat_WR_nJet_bin_5    9.9974e-01 +/-  3.60e-02
gamma_stat_WR_nJet_bin_6    1.0074e+00 +/-  6.65e-02
             mu_TTbar    9.1917e-01 +/-  1.05e-01
             mu_Wjets    9.2631e-01 +/-  1.84e-01
```

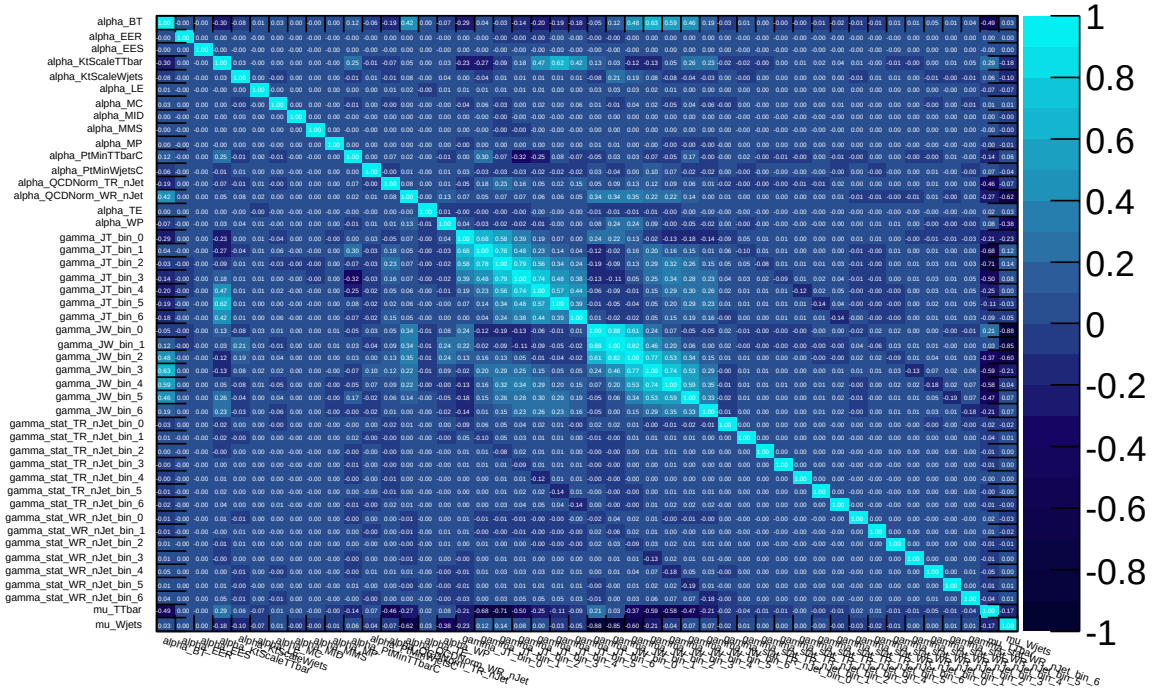

Figure B.1: Correlation matrix for the background-only fit.

B.2 Model-independent limit fit results

The results of the model-independent limit fits with the h1l3jT and h1l4jT selections are shown below and the corresponding correlation matrices are given in Figures B.2 and B.3. These results are discussed in Section 8.2.

```
RooFitResult: minimized FCN value: -190829, estimated distance to minimum: 0.00659437
              covariance matrix quality: Full, accurate covariance matrix
              Status : MIGRAD=0 HESSE=0

  Floating Parameter    FinalValue +/-  Error
--------------------  --------------------------
            alpha_BT    2.5446e-01 +/-  7.03e-01
           alpha_EER    1.1453e-05 +/-  9.88e-01
           alpha_EES    9.5699e-05 +/-  9.95e-01
  alpha_KtScaleTTbar    3.9130e-01 +/-  6.66e-01
  alpha_KtScaleWjets    9.7145e-02 +/-  9.57e-01
            alpha_LE    3.6261e-03 +/-  9.92e-01
            alpha_MC    1.0111e-02 +/-  1.00e+00
           alpha_MID   -8.5997e-04 +/-  9.93e-01
           alpha_MMS    4.7803e-03 +/-  1.01e+00
            alpha_MP   -1.4339e-02 +/-  1.04e+00
  alpha_PtMinTTbar3T   -4.1176e-02 +/-  9.98e-01
   alpha_PtMinTTbarC   -1.6874e-01 +/-  9.48e-01
  alpha_PtMinWjets3T   -1.1593e-01 +/-  9.99e-01
   alpha_PtMinWjetsC    5.0948e-02 +/-  8.48e-01
alpha_QCDNorm_TR_nJet    1.5196e-01 +/-  8.50e-01
alpha_QCDNorm_WR_nJet    3.3165e-02 +/-  7.79e-01
alpha_QCDNorm_h1l3jT_cuts   -1.1867e-01 +/-  9.85e-01
            alpha_TE    6.7338e-02 +/-  6.94e-01
            alpha_WP   -1.2831e-01 +/-  1.04e+00
     gamma_J3T_bin_0    9.2702e-01 +/-  2.29e-01
      gamma_JT_bin_0    1.0451e+00 +/-  6.58e-02
      gamma_JT_bin_1    1.0175e+00 +/-  7.27e-02
      gamma_JT_bin_2    9.6396e-01 +/-  6.84e-02
      gamma_JT_bin_3    9.6090e-01 +/-  8.09e-02
      gamma_JT_bin_4    8.5400e-01 +/-  9.76e-02
      gamma_JT_bin_5    9.0103e-01 +/-  1.43e-01
      gamma_JT_bin_6    1.1056e+00 +/-  2.31e-01
      gamma_JW_bin_0    9.9861e-01 +/-  1.23e-01
      gamma_JW_bin_1    9.8315e-01 +/-  1.01e-01
      gamma_JW_bin_2    1.0031e+00 +/-  8.89e-02
      gamma_JW_bin_3    9.6600e-01 +/-  9.33e-02
      gamma_JW_bin_4    9.8783e-01 +/-  1.18e-01
      gamma_JW_bin_5    9.7918e-01 +/-  1.71e-01
      gamma_JW_bin_6    1.1292e+00 +/-  2.17e-01
gamma_stat_TR_nJet_bin_0    1.0007e+00 +/-  1.09e-02
gamma_stat_TR_nJet_bin_1    1.0002e+00 +/-  1.11e-02
gamma_stat_TR_nJet_bin_2    9.9996e-01 +/-  6.87e-03
gamma_stat_TR_nJet_bin_3    9.9996e-01 +/-  8.69e-03
gamma_stat_TR_nJet_bin_4    9.9964e-01 +/-  1.47e-02
gamma_stat_TR_nJet_bin_5    9.9918e-01 +/-  2.83e-02
```

```
gamma_stat_TR_nJet_bin_6     1.0026e+00 +/-  5.08e-02
gamma_stat_WR_nJet_bin_0     1.0000e+00 +/-  7.20e-03
gamma_stat_WR_nJet_bin_1     9.9998e-01 +/-  8.22e-03
gamma_stat_WR_nJet_bin_2     1.0001e+00 +/-  1.05e-02
gamma_stat_WR_nJet_bin_3     9.9991e-01 +/-  1.36e-02
gamma_stat_WR_nJet_bin_4     9.9984e-01 +/-  3.00e-02
gamma_stat_WR_nJet_bin_5     9.9998e-01 +/-  3.60e-02
gamma_stat_WR_nJet_bin_6     1.0079e+00 +/-  6.65e-02
gamma_stat_h1l3jT_cuts_bin_0    9.4090e-01 +/-  2.01e-01
             mu_TTbar    9.1488e-01 +/-  1.05e-01
             mu_Wjets    9.1881e-01 +/-  1.81e-01
            mu_h1l3jT    1.5065e-08 +/-  1.64e+00
```

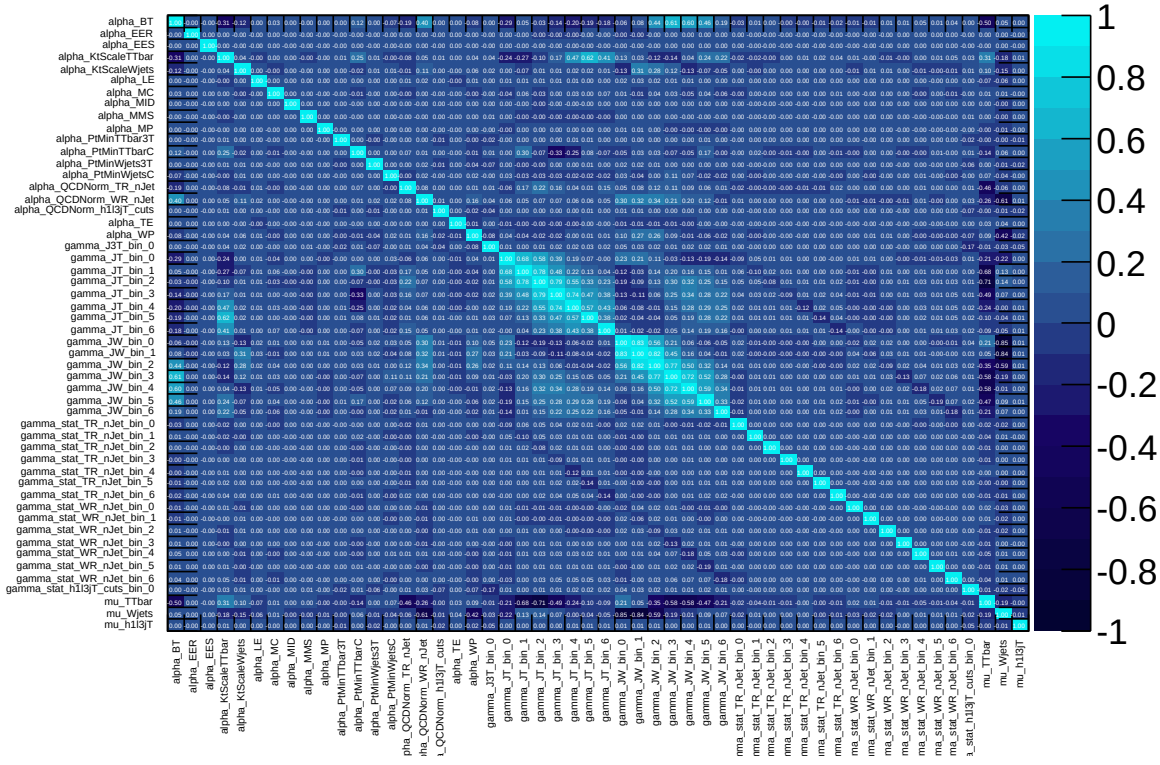

Figure B.2: Correlation matrix for the model-independent limit fit with the h1l3jT selection.

```
RooFitResult: minimized FCN value: -190830, estimated distance to minimum: 0.000380879
              covariance matrix quality: Full, accurate covariance matrix
              Status : MIGRAD=0 HESSE=0

  Floating Parameter    FinalValue +/-  Error
--------------------  --------------------------
            alpha_BT    2.4021e-01 +/-  6.99e-01
           alpha_EER    2.9898e-04 +/-  9.89e-01
           alpha_EES    3.0615e-04 +/-  9.99e-01
  alpha_KtScaleTTbar    3.9772e-01 +/-  6.61e-01
  alpha_KtScaleWjets    7.2748e-02 +/-  7.98e-01
            alpha_LE    2.4498e-03 +/-  9.92e-01
            alpha_MC    1.5738e-02 +/-  9.11e-01
           alpha_MID   -1.0779e-03 +/-  9.92e-01
           alpha_MMS   -3.9024e-04 +/-  9.92e-01
            alpha_MP   -1.2086e-03 +/-  9.86e-01
  alpha_PtMinTTbar4T   -6.4591e-02 +/-  9.87e-01
   alpha_PtMinTTbarC   -1.7184e-01 +/-  9.47e-01
  alpha_PtMinWjets4T   -9.7636e-03 +/-  9.94e-01
   alpha_PtMinWjetsC    2.0784e-02 +/-  8.23e-01
alpha_QCDNorm_TR_nJet    1.2610e-01 +/-  8.50e-01
alpha_QCDNorm_WR_nJet   -1.4293e-02 +/-  7.77e-01
alpha_QCDNorm_h1l4jT_cuts   -3.6581e-02 +/-  9.88e-01
            alpha_TE    2.3278e-02 +/-  4.88e-01
            alpha_WP    2.0755e-02 +/-  1.03e+00
     gamma_J4T_bin_0    9.4566e-01 +/-  2.60e-01
      gamma_JT_bin_0    1.0444e+00 +/-  6.58e-02
      gamma_JT_bin_1    1.0167e+00 +/-  7.25e-02
      gamma_JT_bin_2    9.6351e-01 +/-  6.82e-02
      gamma_JT_bin_3    9.6077e-01 +/-  8.07e-02
      gamma_JT_bin_4    8.5436e-01 +/-  9.72e-02
      gamma_JT_bin_5    9.0149e-01 +/-  1.42e-01
      gamma_JT_bin_6    1.1052e+00 +/-  2.30e-01
      gamma_JW_bin_0    9.9551e-01 +/-  1.23e-01
      gamma_JW_bin_1    9.8272e-01 +/-  9.99e-02
      gamma_JW_bin_2    1.0033e+00 +/-  8.77e-02
      gamma_JW_bin_3    9.6594e-01 +/-  9.28e-02
      gamma_JW_bin_4    9.8754e-01 +/-  1.17e-01
      gamma_JW_bin_5    9.7898e-01 +/-  1.70e-01
      gamma_JW_bin_6    1.1311e+00 +/-  2.16e-01
gamma_stat_TR_nJet_bin_0    1.0007e+00 +/-  1.09e-02
gamma_stat_TR_nJet_bin_1    1.0002e+00 +/-  1.11e-02
gamma_stat_TR_nJet_bin_2    9.9992e-01 +/-  6.87e-03
gamma_stat_TR_nJet_bin_3    9.9992e-01 +/-  8.69e-03
gamma_stat_TR_nJet_bin_4    9.9957e-01 +/-  1.47e-02
gamma_stat_TR_nJet_bin_5    9.9909e-01 +/-  2.83e-02
gamma_stat_TR_nJet_bin_6    1.0023e+00 +/-  5.08e-02
gamma_stat_WR_nJet_bin_0    9.9998e-01 +/-  7.19e-03
gamma_stat_WR_nJet_bin_1    9.9993e-01 +/-  8.21e-03
gamma_stat_WR_nJet_bin_2    1.0000e+00 +/-  1.05e-02
gamma_stat_WR_nJet_bin_3    9.9984e-01 +/-  1.36e-02
gamma_stat_WR_nJet_bin_4    9.9968e-01 +/-  3.00e-02
gamma_stat_WR_nJet_bin_5    9.9979e-01 +/-  3.60e-02
gamma_stat_WR_nJet_bin_6    1.0078e+00 +/-  6.65e-02
gamma_stat_h1l4jT_cuts_bin_0    9.8783e-01 +/-  1.40e-01
            mu_TTbar    9.1765e-01 +/-  1.05e-01
            mu_Wjets    9.1952e-01 +/-  1.80e-01
           mu_h1l4jT    7.5731e-09 +/-  4.36e+00
```

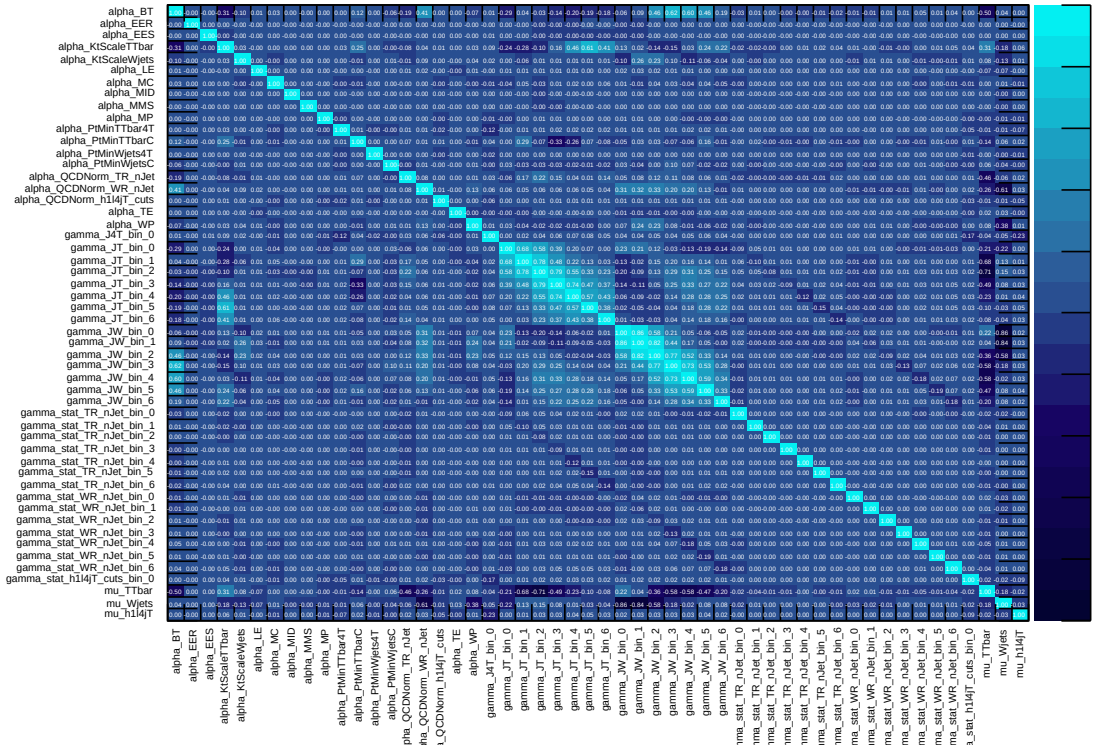

Figure B.3: Correlation matrix for the model-independent limit fit with the h1l4jT selection.

B.3 Exclusion fit result

An example exclusion fit result for the MSUGRA theoretical model point with $m_0 = 580$ GeV and $m_{1/2} = 240$ GeV is shown below and the corresponding correlation matrix is given in Figure B.4. These results are discussed in Section 8.3.

```
RooFitResult: minimized FCN value: -181623, estimated distance to minimum: 0.00679677
              covariance matrix quality: Full, accurate covariance matrix
              Status : MIGRAD=0 HESSE=0

  Floating Parameter    FinalValue +/-  Error
--------------------  --------------------------
                Lumi    9.9998e-01 +/-  3.90e-02
           alpha_BT    2.2737e-01 +/-  6.93e-01
          alpha_EER    3.8757e-05 +/-  1.00e+00
          alpha_EES    9.4243e-03 +/-  1.02e+00
  alpha_KtScaleTTbar    5.0391e-01 +/-  6.20e-01
  alpha_KtScaleWjets    6.7077e-02 +/-  7.42e-01
           alpha_LE    8.5663e-04 +/-  9.92e-01
           alpha_MC   -5.9905e-03 +/-  9.54e-01
          alpha_MID   -6.4042e-04 +/-  9.94e-01
          alpha_MMS   -7.6948e-03 +/-  9.82e-01
           alpha_MP   -3.5517e-03 +/-  1.02e+00
   alpha_PtMinTTbar3   -8.1134e-02 +/-  9.66e-01
   alpha_PtMinTTbar4   -8.2784e-02 +/-  9.76e-01
   alpha_PtMinTTbarC   -1.4722e-01 +/-  9.39e-01
   alpha_PtMinWjets3   -1.2979e-01 +/-  9.36e-01
   alpha_PtMinWjets4   -1.0446e-02 +/-  9.94e-01
   alpha_PtMinWjetsC    4.6094e-02 +/-  8.48e-01
alpha_QCDNorm_TR_nJet    1.6994e-01 +/-  8.47e-01
alpha_QCDNorm_WR_nJet    1.0636e-01 +/-  7.59e-01
alpha_QCDNorm_h1l3j_meffInc   -4.0334e-01 +/-  1.01e+00
alpha_QCDNorm_h1l4j_meffInc   -1.4825e-01 +/-  9.55e-01
           alpha_TE    6.6355e-02 +/-  6.98e-01
           alpha_WP   -1.3458e-01 +/-  9.10e-01
          alpha_XSS   -3.2719e-09 +/-  9.94e-01
      gamma_J3_bin_0    8.4248e-01 +/-  2.94e-01
      gamma_J3_bin_1    1.0038e+00 +/-  7.44e-02
      gamma_J3_bin_2    9.9652e-01 +/-  7.54e-02
      gamma_J3_bin_3    1.0488e+00 +/-  2.03e-01
      gamma_J3_bin_4    9.8156e-01 +/-  1.32e-01
      gamma_J3_bin_5    9.6255e-01 +/-  3.24e-01
      gamma_J4_bin_0    9.5453e-01 +/-  4.05e-01
      gamma_J4_bin_1    1.0207e+00 +/-  1.65e-01
      gamma_J4_bin_2    1.0000e+00 +/-  1.11e-02
      gamma_J4_bin_3    9.3845e-01 +/-  2.50e-01
      gamma_JT_bin_0    1.0456e+00 +/-  6.53e-02
      gamma_JT_bin_1    1.0179e+00 +/-  7.21e-02
      gamma_JT_bin_2    9.6761e-01 +/-  6.73e-02
      gamma_JT_bin_3    9.6877e-01 +/-  7.90e-02
      gamma_JT_bin_4    8.6706e-01 +/-  9.49e-02
      gamma_JT_bin_5    9.2247e-01 +/-  1.38e-01
```

```
      gamma_JT_bin_6    1.1371e+00 +/-  2.44e-01
      gamma_JW_bin_0    1.0033e+00 +/-  1.19e-01
      gamma_JW_bin_1    9.8284e-01 +/-  9.76e-02
      gamma_JW_bin_2    1.0011e+00 +/-  8.56e-02
      gamma_JW_bin_3    9.6433e-01 +/-  9.03e-02
      gamma_JW_bin_4    9.9188e-01 +/-  1.13e-01
      gamma_JW_bin_5    9.8899e-01 +/-  1.64e-01
      gamma_JW_bin_6    1.1174e+00 +/-  1.99e-01
gamma_stat_TR_nJet_bin_0    1.0007e+00 +/-  1.09e-02
gamma_stat_TR_nJet_bin_1    1.0002e+00 +/-  1.11e-02
gamma_stat_TR_nJet_bin_2    9.9996e-01 +/-  6.88e-03
gamma_stat_TR_nJet_bin_3    9.9997e-01 +/-  8.71e-03
gamma_stat_TR_nJet_bin_4    9.9961e-01 +/-  1.55e-02
gamma_stat_TR_nJet_bin_5    9.9903e-01 +/-  3.10e-02
gamma_stat_TR_nJet_bin_6    1.0042e+00 +/-  6.61e-02
gamma_stat_WR_nJet_bin_0    1.0000e+00 +/-  7.20e-03
gamma_stat_WR_nJet_bin_1    9.9998e-01 +/-  8.22e-03
gamma_stat_WR_nJet_bin_2    1.0001e+00 +/-  1.05e-02
gamma_stat_WR_nJet_bin_3    9.9990e-01 +/-  1.37e-02
gamma_stat_WR_nJet_bin_4    9.9989e-01 +/-  3.02e-02
gamma_stat_WR_nJet_bin_5    1.0000e+00 +/-  4.07e-02
gamma_stat_WR_nJet_bin_6    1.0160e+00 +/-  8.44e-02
gamma_stat_h1l3j_meffInc_bin_0    9.4288e-01 +/-  1.88e-01
gamma_stat_h1l3j_meffInc_bin_1    1.0042e+00 +/-  7.66e-02
gamma_stat_h1l3j_meffInc_bin_2    9.9584e-01 +/-  8.26e-02
gamma_stat_h1l3j_meffInc_bin_3    1.0162e+00 +/-  1.30e-01
gamma_stat_h1l3j_meffInc_bin_4    9.4587e-01 +/-  2.06e-01
gamma_stat_h1l3j_meffInc_bin_5    9.8608e-01 +/-  2.24e-01
gamma_stat_h1l4j_meffInc_bin_0    9.7187e-01 +/-  3.47e-01
gamma_stat_h1l4j_meffInc_bin_1    1.0243e+00 +/-  1.77e-01
gamma_stat_h1l4j_meffInc_bin_2    9.9161e-01 +/-  1.77e-01
gamma_stat_h1l4j_meffInc_bin_3    9.7944e-01 +/-  1.43e-01
             mu_SIG    1.7209e-08 +/-  2.61e-02
           mu_TTbar    9.1313e-01 +/-  1.02e-01
           mu_Wjets    9.0765e-01 +/-  1.77e-01
```

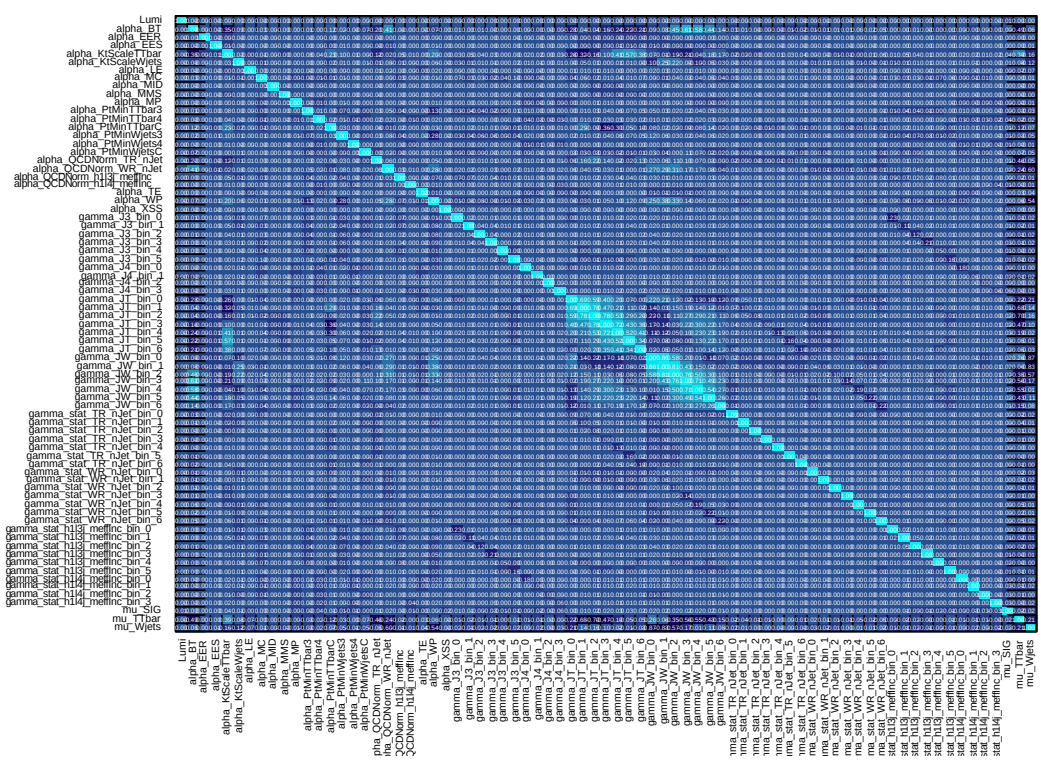

Figure B.4: Correlation matrix for the exclusion fit for the MUSGRA theoretical model point with $m_0 = 580$ GeV and $m_{1/2} = 240$ GeV.

Appendix C

Signal region systematics

The systematics in the signal regions before and after the background-only fit to the control regions has been performed is shown in Tables C.1 and C.2 respectively. Note that only the systematics that have an effect greater than one per cent in any region are shown. The uncertainties that relate to the signal regions only (the jet energy scale and statistical uncertainties) are calculated from the input variables without fitting as relative uncertainties. As the total expected number of background events changes after the fit has been performed (relative to the expected yields before the fit) the absolute values of these uncertainties must also change, while the relative values of the uncertainties remain constant.

Signal channel	**h1l3j**	**h1l4j**	**h1l3jT**	**h1l4jT**
Expected number of events	102.21	8.21	5.52	8.10
Total statistical ($\sqrt{N_{\text{obs}}}$)	±9.06	±2.45	±1.73	±2.45
Total background systematic	±21.81	±2.01	±2.04	±2.87
W+jets yield	±0.04	±0.00	±0.00	±0.00
$t\bar{t}$ yield	±0.05	±0.01	±0.00	±0.01
Jet energy scale bin 0	±1.89	±0.81	±1.27	±2.42
Jet energy scale bin 1	±4.73	±0.74	—	—
Jet energy scale bin 2	±10.86	±0.32	—	—
Jet energy scale bin 3	±1.43	±0.54	—	—
Jet energy scale bin 4	±0.29	—	—	—
Jet energy scale bin 5	±1.14	—	—	—
MC and multijets statistics bin 0	±1.35	±0.51	±1.23	±1.19
MC and multijets statistics bin 1	±3.03	±0.72	—	—
MC and multijets statistics bin 2	±3.11	±0.32	—	—
MC and multijets statistics bin 3	±1.74	±0.75	—	—
MC and multijets statistics bin 4	±0.77	—	—	—
MC and multijets statistics bin 5	±0.98	—	—	—
Multijets systematic	±3.11	±0.34	±0.36	±0.30
p_{T}^{W} reweighting	±13.75	±0.04	±0.76	±0.04
W+jets k_{T} scale	±0.44	±0.20	±0.06	±0.20
$t\bar{t}$ k_{T} scale	±0.67	±0.01	±0.07	±0.01
W+jets $p_{\text{T}}^{\text{min}}$	±8.30	±0.13	±0.51	±0.13
$t\bar{t}$ $p_{\text{T}}^{\text{min}}$	±5.71	±0.89	±0.20	±0.89

Table C.1: Breakdown of the dominant systematic uncertainties on background estimates in the various signal regions. Note that the individual uncertainties can be correlated, and do not necessarily add up quadratically to the total background uncertainty.

Signal channel	**h1l3j**	**h1l4j**	**h1l3jT**	**h1l4jT**
Expected number of events	91.68	7.25	5.06	7.14
Total statistical ($\sqrt{N_{\text{obs}}}$)	±9.06	±2.45	±1.73	±2.45
Total background systematic	±20.46	±1.87	±1.89	±2.59
W+jets yield	±8.09	±0.30	±0.50	±0.30
$t\bar{t}$ yield	±4.60	±0.54	±0.16	±0.54
Jet energy scale bin 0	±1.69	±0.71	±1.16	±2.13
Jet energy scale bin 1	±4.23	±0.66	—	—
Jet energy scale bin 2	±9.73	±0.28	—	—
Jet energy scale bin 3	±1.29	±0.47	—	—
Jet energy scale bin 4	±0.27	—	—	—
Jet energy scale bin 5	±1.04	—	—	—
MC and multijets statistics bin 0	±1.22	±0.45	±1.13	±1.05
MC and multijets statistics bin 1	±2.72	±0.64	—	—
MC and multijets statistics bin 2	±2.79	±0.28	—	—
MC and multijets statistics bin 3	±1.57	±0.67	—	—
MC and multijets statistics bin 4	±0.72	—	—	—
MC and multijets statistics bin 5	±0.89	—	—	—
Multijets systematic	±3.11	±0.34	±0.36	±0.30
p_{T}^{W} reweighting	±13.16	±0.02	±0.73	±0.04
W+jets k_{T} scale	±0.22	±0.11	±0.04	±0.11
$t\bar{t}$ k_{T} scale	±3.68	±0.37	±0.14	±0.37
W+jets $p_{\text{T}}^{\text{min}}$	±7.73	±0.12	±0.48	±0.12
$t\bar{t}$ $p_{\text{T}}^{\text{min}}$	±4.83	±0.76	±0.17	±0.76

Table C.2: Breakdown of the dominant systematic uncertainties on background estimates in the various signal regions. Note that the individual uncertainties can be correlated, and do not necessarily add up quadratically to the total background uncertainty.

Glossary of abbreviations

BC Bunch crossing

BCID Bunch crossing identifier

BOC Back of crate

CSC Cathode Strip Chamber

DAQ Data acquisition

DCS Detector control system

DM Dark matter

DSP Digital signal processor

ECal Electromagnetic calorimeter

EF Event filter (trigger)

EMEC Electromagnetic end-cap (calorimeter)

ESD Electrostatic discharge

EWSB Electroweak symmetry breaking

FCal Forward calorimeter

FPGA Field programmable gate array

GRL Good runs list

GUT Grand Unified Theory

HCal Hadronic calorimeter

HEC Hadronic end-cap (calorimeter)

HT High threshold (TRT hit)

ID Inner detector

ISR Initial state radiation

L1 Level one (trigger)

L2 Level two (trigger)

LAr Liquid argon

LB Luminosity block

LEP Large Electron-Positron collider

LHC Large Hadron Collider

Linac Linear accelerator

LT Low threshold (TRT hit)

MC Monte Carlo (simulation)

MDSP Master digital signal processor

MDT Monitored Drift Tube

MS Muon spectrometer

MSSM Minimally Supersymmetric Standard Model

MSUGRA Minimal Super-Gravity

MTTF Mean time to failure

PDF Parton distribution function

pdf Probability distribution function

PIN *p-i-n* (diode)

PS Proton Synchrotron

QCD Quantum Chromodynamics

ROD Read-out driver

RoI Region of interest

RPC Resistive Plate Chamber

Rx Reception path

SCT Semiconductor Tracker

SDSP Slave digital signal processor

SPS Super Proton Synchrotron

SM Standard Model (of particle physics)

SUSY Supersymmetry or supersymmetric

TDAQ Trigger and data acquisition system

TIM TTC interface module

TileCal Tile calorimeter

TGC Thin Gap Chamber

TR $t\bar{t}$ control region

TRT Transition Radiation Tracker

TTC Trigger, timing and control

Tx Transmission path

VCSEL Vertical cavity surface emitting laser

WLCG Worldwide LHC Computing Grid

WR W+jets control region

List of figures

List of tables

Bibliography

[1] S. Glashow, "Partial Symmetries of Weak Interactions", *Nucl.Phys.* **22** (1961) 579–588.

[2] S. Weinberg, "A Model of Leptons", *Phys.Rev.Lett.* **19** (1967) 1264–1266.

[3] F. Englert and R. Brout, "Broken Symmetry and the Mass of Gauge Vector Mesons", *Phys.Rev.Lett.* **13** (1964) 321–323.

[4] P. W. Higgs, "Broken Symmetries and the Masses of Gauge Bosons", *Phys.Rev.Lett.* **13** (1964) 508–509.

[5] G. Guralnik, C. Hagen, and T. Kibble, "Global Conservation Laws and Massless Particles", *Phys.Rev.Lett.* **13** (1964) 585–587.

[6] C. T. Hill and E. H. Simmons, "Strong dynamics and electroweak symmetry breaking", *Phys.Rept.* **381** (2003) 235–402, arXiv:hep-ph/0203079 [hep-ph].

[7] **WMAP** Collaboration, E. Komatsu *et al.*, "Seven-Year Wilkinson Microwave Anisotropy Probe (WMAP) Observations: Cosmological Interpretation", *Astrophys.J.Suppl.* **192** (2011) 18, arXiv:1001.4538 [astro-ph.CO].

[8] M. Markevitch, A. Gonzalez, D. Clowe, A. Vikhlinin, L. David, *et al.*, "Direct constraints on the dark matter self-interaction cross-section from the merging galaxy cluster 1E0657-56", *Astrophys.J.* **606** (2004) 819–824, arXiv:astro-ph/0309303 [astro-ph].

[9] N. Arkani-Hamed, S. Dimopoulos, and G. Dvali, "The Hierarchy problem and new dimensions at a millimeter", *Phys.Lett.* **B429** (1998) 263–272, arXiv:hep-ph/9803315 [hep-ph].

[10] L. Randall and R. Sundrum, "A Large mass hierarchy from a small extra dimension", *Phys.Rev.Lett.* **83** (1999) 3370–3373, arXiv:hep-ph/9905221 [hep-ph].

[11] J. Wess and B. Zumino, "A Lagrangian Model Invariant Under Supergauge Transformations", *Phys.Lett.* **B49** (1974) 52.

[12] **UA1** Collaboration, G. Arnison *et al.*, "Experimental Observation of Isolated Large Transverse Energy Electrons with Associated Missing Energy at $\sqrt{s} = 540$ GeV", *Phys.Lett.* **B122** (1983) 103–116.

[13] **UA2** Collaboration, M. Banner *et al.*, "Observation of Single Isolated Electrons of High Transverse Momentum in Events with Missing Transverse Energy at the CERN $\bar{p}p$ Collider", *Phys.Lett.* **B122** (1983) 476–485.

[14] **UA1** Collaboration, G. Arnison *et al.*, "Experimental Observation of Lepton Pairs of Invariant Mass Around 95 GeV/c^2 at the CERN SPS Collider", *Phys.Lett.* **B126** (1983) 398–410.

[15] **UA2** Collaboration, P. Bagnaia *et al.*, "Evidence for $Z^0 \to e^+e^-$ at the CERN $\bar{p}p$ Collider", *Phys.Lett.* **B129** (1983) 130–140.

[16] **CDF** Collaboration, F. Abe *et al.*, "Observation of top quark production in $\bar{p}p$ collisions", *Phys.Rev.Lett.* **74** (1995) 2626–2631, `arXiv:hep-ex/9503002 [hep-ex]`.

[17] **D0** Collaboration, S. Abachi *et al.*, "Search for high mass top quark production in $p\bar{p}$ collisions at $\sqrt{s} = 1.8$ TeV", *Phys.Rev.Lett.* **74** (1995) 2422–2426, `arXiv:hep-ex/9411001 [hep-ex]`.

[18] **ATLAS** Collaboration, "An update to the combined search for the Standard Model Higgs boson with the ATLAS detector at the LHC using up to 4.9 fb^{-1} of pp collision data at $\sqrt{s} = 7$ TeV", Tech. Rep. ATLAS-CONF-2012-019, CERN, Mar, 2012.

[19] **CMS** Collaboration, S. Chatrchyan *et al.*, "Combined results of searches for the standard model Higgs boson in pp collisions at $\sqrt{s} = 7$ TeV", *Phys.Lett.* **B710** (2012) 26–48, `arXiv:1202.1488 [hep-ex]`.

[20] **ATLAS** Collaboration, "ATLAS Supersymmetry (SUSY) searches", `https://twiki.cern.ch/twiki/bin/view/AtlasPublic/SupersymmetryPublicResults`, 2012.

[21] **CMS** Collaboration, "CMS Supersymmetry Physics Results", `https://twiki.cern.ch/twiki/bin/view/CMSPublic/PhysicsResultsSUS`, 2012.

[22] **CMS** and **LHCb** Collaborations, "Search for the rare decay $B_s^0 \to \mu^+\mu^-$ at the LHC with the CMS and LHCb experiments", Tech. Rep. CMS-PAS-BPH-11-019, LHCb-CONF-2011-047, CERN-LHCb-CONF-2011-047, CERN, 2011.

[23] **CDF** Collaboration, T. Aaltonen *et al.*, "Search for $B_s \to \mu^+\mu^-$ and $B_d \to \mu^+\mu^-$ Decays with CDF II", *Phys.Rev.Lett.* **107** (2011) 239903, `arXiv:1107.2304 [hep-ex]`.

[24] F. Mayet, "Dark Matter Portal", `http://lpsc.in2p3.fr/mayet/dm.php`, 2012.

[25] E. Noether, "Invariante Variationsprobleme", *Nachr.D.König.Gesellsch.D.Wiss. Zu Göttingen, Math-phys* (1918) 235–257.

[26] **Particle Data Group** Collaboration, K. Nakamura *et al.*, "Review of particle physics", *J.Phys.* **G37** (2010) 075021.

[27] S. Weinberg, "Implications of Dynamical Symmetry Breaking", *Phys.Rev.* **D13** (1976) 974–996.

[28] E. Gildener, "Gauge Symmetry Hierarchies", *Phys.Rev.* **D14** (1976) 1667.

[29] S. Weinberg, "Implications of Dynamical Symmetry Breaking: An Addendum", *Phys.Rev.* **D19** (1979) 1277–1280.

[30] L. Susskind, "Dynamics of Spontaneous Symmetry Breaking in the Weinberg- Salam Theory", *Phys.Rev.* **D20** (1979) 2619–2625.

[31] G. t' Hooft and M. Veltman, "Regularization and renormalization of gauge fields", *Nucl.Phys.* **B44** (1972) 189–213.

[32] G. H. and S. L. Glashow, "Unity of all elementary particle forces", *Phys.Rev.Lett.* **32** (1974) 438–441.

[33] **WMAP** Collaboration, D. Larson, J. Dunkley, G. Hinshaw, E. Komatsu, M. Nolta, *et al.*, "Seven-Year Wilkinson Microwave Anisotropy Probe (WMAP) Observations: Power Spectra and WMAP-Derived Parameters", *Astrophys.J.Suppl.* **192** (2011) 16, `arXiv:1001.4635 [astro-ph.CO]`.

[34] F. Zwicky, "Die Rotverschiebung von extragalaktischen Nebeln", *Helv.Phys.Acta* **6** (1933) 110.

[35] H. Miyazawa, "Baryon Number Changing Currents", *Prog.Theor.Phys.* **36 (6)** (1966) 1266–1276.

[36] P. Ramond, "Dual Theory for Free Fermions", *Phys.Rev.* **D3** (1971) 2415–2418.

[37] Y. A. Golfand and E. P. Likhtman, "Extension of the Algebra of Poincare Group Generators and Violation of p Invariance", *JETP Lett.* **13** (1971) 323–326.

[38] A. Neveu and J. H. Schwarz, "Factorizable dual model of pions", *Nucl.Phys.* **B31** (1971) 86–112.

[39] A. Neveu and J. H. Schwarz, "Quark Model of Dual Pions", *Phys.Rev.* **D4** (1971) 1109–1111.

[40] J. Gervais and B. Sakita, "Field theory interpretation of supergauges in dual models", *Nucl.Phys.* **B34** (1971) 632–639.

[41] D. V. Volkov and V. P. Akulov, "Is the Neutrino a Goldstone Particle?", *Phys.Lett.* **B46** (1973) 109–110.

[42] J. Wess and B. Zumino, "Supergauge Transformations in Four-Dimensions", *Nucl.Phys.* **B70** (1974) 39–50.

[43] P. Fayet, "Supersymmetry and Weak, Electromagnetic and Strong Interactions", *Phys.Lett.* **B64** (1976) 159.

[44] P. Fayet, "Spontaneously Broken Supersymmetric Theories of Weak, Electromagnetic and Strong Interactions", *Phys.Lett.* **B69** (1977) 489.

[45] G. R. Farrar and P. Fayet, "Phenomenology of the Production, Decay, and Detection of New Hadronic States Associated with Supersymmetry", *Phys.Lett.* **B76** (1978) 575–579.

[46] P. Fayet, "Relations Between the Masses of the Superpartners of Leptons and Quarks, the Goldstino Couplings and the Neutral Currents", *Phys.Lett.* **B84** (1979) 416.

[47] S. Dimopoulos and H. Georgi, "Softly Broken Supersymmetry and SU(5)", *Nucl.Phys.* **B193** (1981) 150.

[48] E. Witten, "Dynamical Breaking of Supersymmetry", *Nucl.Phys.* **B188** (1981) 513.

[49] M. Dine, W. Fischler, and M. Srednicki, "Supersymmetric Technicolor", *Nucl.Phys.* **B189** (1981) 575–593.

[50] S. Dimopoulos and S. Raby, "Supercolor", *Nucl.Phys.* **B192** (1981) 353.

[51] N. Sakai, "Naturalness in Supersymmetric Guts", *Zeit.Phys.* **C11** (1981) 153.

[52] R. Kaul and P. Majumdar, "Cancellation of Quadratically Divergent Mass Corrections in Globally Supersummetric Spontaneously Broken Gauge Theories", *Nucl.Phys.* **B199** (1982) 36.

[53] C. Giunti, C. W. Kim, and U. Lee, "Running coupling constants and grand unification models", *Mod.Phys.Lett.* **A6** (1991) 1745–1755.

[54] J. Ellis, S. Kelley, and D. Nanopoulos, "Probing the desert using gauge coupling unification", *Phys.Lett.* **B260** (1991) 131–137.

[55] U. Amaldi, W. de Boer, and H. Furstenau, "Comparison of grand unified theories with electroweak and strong coupling constants measured at LEP", *Phys.Lett.* **B260** (1991) 447–455.

[56] P. Langacker and M.-X. Luo, "Implications of precision electroweak experiments for M_t, ρ_0, $\sin^2\theta_W$ and grand unification", *Phys.Rev.* **D44** (1991) 817–822.

[57] H. Goldberg, "Constraint on the photino mass from cosmology", *Phys.Rev.Lett.* **50** (1983) 1419.

[58] J. Ellis, J. Hagelin, D. Nanopoulos, K. Olive, and M. Srednicki, "Supersymmetric relics from the big bang", *Nucl.Phys.* **B238** (1984) 453–476.

[59] D. J. Gross and F. Wilczek, "Asymptotically free gauge theories", *Phys.Rev.* **D8** (1973) 3633–3652.

[60] H. D. Politzer, "Reliable perturbative results for strong interactions?", *Phys.Rev.Lett.* **30** (1973) 1346–1349.

[61] J. Pumplin, D. Stump, J. Huston, H. Lai, P. M. Nadolsky, *et al.*, "New generation of parton distributions with uncertainties from global QCD analysis", *JHEP* **0207** (2002) 012, arXiv:hep-ph/0201195 [hep-ph].

[62] A. Martin, W. Stirling, R. Thorne, and G. Watt, "Parton distributions for the LHC", *Eur.Phys.J.* **C63** (2009) 189–285, arXiv:0901.0002 [hep-ph].

[63] **H1 and ZEUS** Collaboration, F. D. Aaron *et al.*, "Combined Measurement and QCD Analysis of the Inclusive ep Scattering Cross Sections at HERA", *JHEP* **01** (2010) 109, arXiv:0911.0884 [hep-ex].

[64] O. S. Brüning, P. Collier, P. Lebrun, S. Myers, R. Ostojic, J. Poole, and P. Proudlock, *LHC Design Report*. CERN, 2004.

[65] *LEP design report*. CERN, 1984. Copies shelved as reports in LEP, PS and SPS libraries.

[66] M. Bajko *et al.*, "Report of the Task Force on the Incident of 19th September 2008 at the LHC", Tech. Rep. LHC-PROJECT-Report-1168. CERN-LHC-PROJECT-Report-1168, CERN, Mar, 2009.

[67] **ALICE** Collaboration, K. Aamodt *et al.*, "The ALICE experiment at the CERN LHC", *JINST* **3** (2008) S08002.

[68] **ATLAS** Collaboration, G. Aad *et al.*, "The ATLAS Experiment at the CERN Large Hadron Collider", *JINST* **3** (2008) S08003.

[69] **CMS** Collaboration, S. Chatrchyan *et al.*, "The CMS experiment at the CERN LHC", *JINST* **3** (2008) S08004.

[70] **LHCb** Collaboration, J. Alves, A. Augusto *et al.*, "The LHCb Detector at the LHC", *JINST* **3** (2008) S08005.

[71] **LHCf** Collaboration, O. Adriani *et al.*, *LHCf experiment: Technical Design Report*. Technical Design Report LHCf. CERN, 2006.

[72] **MoEDAL** Collaboration, J. Pinfold *et al.*, "Technical design report of the moedal experiment", Tech. Rep. CERN-LHCC-2009-006. MoEDAL-TDR-001, CERN, Jun, 2009.

[73] **TOTEM** Collaboration, V. Berardi *et al.*, *Total cross-section, elastic scattering and diffraction dissociation at the Large Hadron Collider at CERN: TOTEM Technical Design Report*. Technical Design Report TOTEM. CERN, 2004.

[74] C. Lefèvre, "The CERN accelerator complex. Complexe des accélérateurs du CERN", Dec, 2008.

[75] **ATLAS** Collaboration, *ATLAS inner detector: Technical Design Report, 1*. Technical Design Report ATLAS. CERN, 1997.

[76] **ATLAS** Collaboration, *ATLAS inner detector: Technical Design Report, 2*. Technical Design Report ATLAS. CERN, 1997.

[77] **ATLAS** Collaboration, N. Wermes and G. Hallewel, *ATLAS pixel detector: Technical Design Report*. Technical Design Report ATLAS. CERN, 1998.

[78] **ATLAS** Collaboration, *ATLAS liquid-argon calorimeter: Technical Design Report*. Technical Design Report ATLAS. CERN, 1996.

[79] **ATLAS** Collaboration, *ATLAS tile calorimeter: Technical Design Report*. Technical Design Report ATLAS. CERN, 1996.

[80] **ATLAS** Collaboration, *ATLAS muon spectrometer: Technical Design Report*. Technical Design Report ATLAS. CERN, 1997.

[81] **ATLAS** Collaboration, G. Aad *et al.*, "Expected Performance of the ATLAS Experiment - Detector, Trigger and Physics", `arXiv:0901.0512 [hep-ex]`.

[82] W. Lampl, S. Laplace, D. Lelas, P. Loch, H. Ma, *et al.*, "Calorimeter clustering algorithms: Description and performance", Tech. Rep. ATL-LARG-PUB-2008-002, ATL-COM-LARG-2008-003, CERN, 2008.

[83] M. Cacciari, G. P. Salam, and G. Soyez, "The Anti-k_{T} jet clustering algorithm", *JHEP* **0804** (2008) 063, `arXiv:0802.1189 [hep-ph]`.

[84] C. Eck *et al.*, *LHC computing Grid: Technical Design Report. Version 1.06 (20 Jun 2005)*. Technical Design Report LCG. CERN, 2005.

[85] M. L. Mangano, M. Moretti, F. Piccinini, R. Pittau, and A. D. Polosa, "ALPGEN, a generator for hard multiparton processes in hadronic collisions", *JHEP* **0307** (2003) 001, `arXiv:hep-ph/0206293 [hep-ph]`.

[86] M. Aliev, H. Lacker, U. Langenfeld, S. Moch, P. Uwer, *et al.*, "HATHOR: HAdronic Top and Heavy quarks crOss section calculatoR", *Comput.Phys.Commun.* **182** (2011) 1034–1046, `arXiv:1007.1327 [hep-ph]`.

[87] K. Melnikov and F. Petriello, "Electroweak gauge boson production at hadron colliders through $\mathcal{O}(\alpha_s^2)$", *Phys.Rev.* **D74** (2006) 114017, `arXiv:hep-ph/0609070 [hep-ph]`.

[88] S. Frixione and B. R. Webber, "Matching NLO QCD computations and parton shower simulations", *JHEP* **0206** (2002) 029, `arXiv:hep-ph/0204244 [hep-ph]`.

[89] G. Corcella, I. Knowles, G. Marchesini, S. Moretti, K. Odagiri, *et al.*, "HERWIG 6: An Event generator for hadron emission reactions with interfering gluons (including supersymmetric processes)", *JHEP* **0101** (2001) 010, `arXiv:hep-ph/0011363 [hep-ph]`.

[90] J. M. Campbell, R. Ellis, and D. L. Rainwater, "Next-to-leading order QCD predictions for W + 2 jet and Z + 2 jet production at the CERN LHC", *Phys.Rev.* **D68** (2003) 094021, `arXiv:hep-ph/0308195 [hep-ph]`.

[91] J. Pumplin, D. Stump, J. Huston, H. Lai, P. M. Nadolsky, *et al.*, "New generation of parton distributions with uncertainties from global QCD analysis", *JHEP* **0207** (2002) 012, arXiv:hep-ph/0201195 [hep-ph].

[92] H.-L. Lai, M. Guzzi, J. Huston, Z. Li, P. M. Nadolsky, *et al.*, "New parton distributions for collider physics", *Phys.Rev.* **D82** (2010) 074024, arXiv:1007.2241 [hep-ph].

[93] A. Sherstnev and R. Thorne, "Different PDF approximations useful for LO Monte Carlo generators", arXiv:0807.2132 [hep-ph].

[94] J. Alwall, S. Hoche, F. Krauss, N. Lavesson, L. Lonnblad, *et al.*, "Comparative study of various algorithms for the merging of parton showers and matrix elements in hadronic collisions", *Eur.Phys.J.* **C53** (2008) 473–500, arXiv:0706.2569 [hep-ph].

[95] J. Butterworth, J. R. Forshaw, and M. Seymour, "Multiparton interactions in photoproduction at HERA", *Z.Phys.* **C72** (1996) 637–646, arXiv:hep-ph/9601371 [hep-ph].

[96] "New ATLAS event generator tunes to 2010 data", Tech. Rep. ATL-PHYS-PUB-2011-008, CERN, Apr, 2011.

[97] **GEANT4** Collaboration, S. Agostinelli *et al.*, "GEANT4: A Simulation toolkit", *Nucl.Instrum.Meth.* **A506** (2003) 250–303.

[98] T. Sjöstrand, P. Edén, C. Friberg, L. Lönnblad, G. Miu, *et al.*, "High-energy physics event generation with PYTHIA 6.1", *Comput.Phys.Commun.* **135** (2001) 238–259, arXiv:hep-ph/0010017.

[99] **ATLAS** Collaboration, "Egamma Trigger Public Results", 2012. https://twiki.cern.ch/twiki/bin/view/AtlasPublic/EgammaTriggerPublicResults.

[100] **ATLAS** Collaboration, "Muon Trigger Public Results", 2012. https://twiki.cern.ch/twiki/bin/view/AtlasPublic/MuonTriggerPublicResults.

[101] **ATLAS** Collaboration, "Further search for supersymmetry at $\sqrt{s} = 7$ TeV in final states with jets, missing transverse momentum and one isolated lepton", Tech. Rep. ATLAS-CONF-2012-041, CERN, Mar, 2012.

[102] **ATLAS** Collaboration, S. Asai *et al.*, "Search for Supersymmetry with jets and missing transverse momentum and one or more leptons at $\sqrt{s} = 7$ TeV", Tech. Rep. ATL-PHYS-INT-2012-025, CERN, 2012.

[103] **ATLAS** Collaboration, "SUSYTools-00-00-55", SVN package, 2012. svn+ssh://svn.cern.ch/reps/atlasoff/PhysicsAnalysis/SUSYPhys/SUSYTools/tags/SUSYTools-00-00-55.

[104] **ATLAS** Collaboration, S. Asai *et al.*, "Search for Supersymmetry with jets and missing transverse momentum and one lepton at $\sqrt{s} = 7$ TeV", Tech. Rep. ATL-COM-PHYS-2011-848, CERN, 2011.

[105] **ATLAS** Collaboration, G. Aad *et al.*, "Jet energy measurement with the ATLAS detector in proton-proton collisions at $\sqrt{s} = 7$ TeV", arXiv:1112.6426 [hep-ex].

[106] **ATLAS** Collaboration, "JetUncertainties-00-03-05-01", SVN package, 2012. svn+ssh://svn.cern.ch/reps/atlasoff/Reconstruction/Jet/JetUncertainties/tags/JetUncertainties-00-03-05-01.

[107] **ATLAS** Collaboration, G. Aad *et al.*, "Search for supersymmetry in final states with jets, missing transverse momentum and one isolated lepton in $\sqrt{s} = 7$ TeV pp collisions using 1 fb^{-1} of ATLAS data", *Phys.Rev.* **D85** (2012) 012006, arXiv:1109.6606 [hep-ex].

[108] **ATLAS** Collaboration, G. Aad *et al.*, "Electron performance measurements with the ATLAS detector using the 2010 LHC proton-proton collision data", *Eur.Phys.J.* **C72** (2012) 1909, arXiv:1110.3174 [hep-ex].

[109] **ATLAS** Collaboration, "egammaAnalysisUtils-00-02-72", SVN package, 2012. svn+ssh://svn.cern.ch/reps/atlasoff/Reconstruction/egamma/egammaAnalysis/egammaAnalysisUtils/tags/egammaAnalysisUtils-00-02-72.

[110] **ATLAS** Collaboration, "Muon Performance Public Plots", 2012. https://twiki.cern.ch/twiki/bin/view/AtlasPublic/MuonPerformancePublicPlots.

[111] **ATLAS** Collaboration, "MuonMomentumCorrections-00-04-01", SVN package, 2012. svn+ssh://svn.cern.ch/reps/atlasoff/PhysicsAnalysis/MuonID/MuonIDAnalysis/MuonMomentumCorrections/tags/MuonMomentumCorrections-00-04-01.

[112] **ATLAS** Collaboration, "MissingETUtility-00-02-13", SVN package, 2012. svn+ssh://svn.cern.ch/reps/atlasoff/Reconstruction/MissingETUtility/tags/MissingETUtility-00-02-13.

[113] **ATLAS** Collaboration, "MuonEfficiencyCorrections-01-00-10", SVN package, 2012. svn+ssh://svn.cern.ch/reps/atlasoff/PhysicsAnalysis/MuonID/MuonIDAnalysis/MuonEfficiencyCorrections/tags/MuonEfficiencyCorrections-01-00-10.

[114] **ATLAS** Collaboration, "Calibrating the b-Tag Efficiency and Mistag Rate in 35 pb^{-1} of Data with the ATLAS Detector", Tech. Rep. ATLAS-CONF-2011-089, CERN, Jun, 2011.

[115] **ATLAS** Collaboration, "CalibrationDataInterface-00-00-11", SVN package, 2012. svn+ssh://svn.cern.ch/reps/atlasoff/PhysicsAnalysis/JetTagging/JetTagPerformanceCalibration/CalibrationDataInterface/tags/CalibrationDataInterface-00-00-11.

[116] T. Gleisberg, S. Hoeche, F. Krauss, M. Schonherr, S. Schumann, *et al.*, "Event generation with SHERPA 1.1", *JHEP* **0902** (2009) 007, arXiv:0811.4622 [hep-ph].

[117] W. Beenakker, S. Brensing, M. Krä"mer, A. Kulesza, E. Laenen, L. Motyka, and I. Niessen, "Squark and gluino hadroproduction", *Int. J. Mod. Phys.* **A26** (2011) 2637–2664.

[118] W. Beenakker, R. Hopker, M. Spira, and P. Zerwas, "Squark and gluino production at hadron colliders", *Nucl.Phys.* **B492** (1997) 51–103, arXiv:hep-ph/9610490 [hep-ph].

[119] P. M. Nadolsky *et al.*, "Implications of CTEQ global analysis for collider observables", *Phys.Rev.* **D78** (2008) 013004, arXiv:0802.0007 [hep-ph].

[120] A. Martin, W. Stirling, R. Thorne, and G. Watt, "Parton distributions for the LHC", *Eur.Phys.J.* **C63** (2009) 189–285, arXiv:0901.0002 [hep-ph].

[121] H.-L. Lai *et al.*, "Uncertainty induced by QCD coupling in the CTEQ global analysis of parton distributions", *Phys.Rev.* **D82** (2010) 054021, arXiv:1004.4624 [hep-ph].

[122] **ATLAS** Collaboration, G. Aad *et al.*, "The ATLAS Simulation Infrastructure", *Eur.Phys.J.* **C70** (2010) 823–874, arXiv:1005.4568 [physics.ins-det].

[123] E. Richter-Was, D. Froidevaux, and L. Poggioli, "ATLFAST 2.0 a fast simulation package for ATLAS", Tech. Rep. ATL-PHYS-98-131, CERN, Nov, 1998.

[124] F. E. Paige, S. D. Protopopescu, H. Baer, and X. Tata, "ISAJET 7.69: A Monte Carlo event generator for p p, anti-p p, and e+ e- reactions", arXiv:hep-ph/0312045.

[125] M. Bahr *et al.*, "Herwig++ Physics and Manual", *Eur.Phys.J.* **C58** (2008) 639–707, arXiv:0803.0883 [hep-ph].

[126] A. Sherstnev and R. S. Thorne, "Parton Distributions for LO Generators", *Eur.Phys.J.* **C55** (2008) 553–575, arXiv:0711.2473 [hep-ph].

[127] J. Alwall, M. Herquet, F. Maltoni, O. Mattelaer, and T. Stelzer, "MadGraph 5 : Going Beyond", *JHEP* **1106** (2011) 128, arXiv:1106.0522 [hep-ph].

[128] **ATLAS** Collaboration, "FakeLeptBkg-00-00-06", SVN package, 2012. svn+ssh://svn.cern.ch/reps/atlasoff/PhysicsAnalysis/SUSYPhys/FakeLeptBkg/tags/FakeLeptBkg-00-00-06.

[129] K. Cranmer, "HistFactory User Guide (ROOT 5.32)", 2012. https://twiki.cern.ch/twiki/pub/RooStats/WebHome/HistFactoryLikelihood.pdf.

[130] **ATLAS** Collaboration, "HistFitter (previously known as SusyFitter)", 2012. https://twiki.cern.ch/twiki/bin/viewauth/AtlasProtected/SusyFitter.

[131] L. Moneta, K. Belasco, K. S. Cranmer, S. Kreiss, A. Lazzaro, *et al.*, "The RooStats Project", *PoS* **ACAT2010** (2010) 057, arXiv:1009.1003 [physics.data-an].

[132] R. Brun and F. Rademakers, "ROOT: An object oriented data analysis framework", *Nucl.Instrum.Meth.* **A389** (1997) 81–86.

[133] M. Battaglia, A. De Roeck, J. R. Ellis, F. Gianotti, K. T. Matchev, *et al.*, "Proposed post-LEP benchmarks for supersymmetry", *Eur.Phys.J.* **C22** (2001) 535–561, arXiv:hep-ph/0106204 [hep-ph].

[134] **LEP** Collaboration, "Combined LEP Chargino Results, up to 208 GeV for large m_0", http://lepsusy.web.cern.ch/lepsusy/www/inos_moriond01/charginos_pub.html, 2001.

[135] **ATLAS** Collaboration, G. Aad *et al.*, "Luminosity Determination in pp Collisions at $\sqrt{s} = 7$ TeV Using the ATLAS Detector at the LHC", *Eur.Phys.J.* **C71** (2011) 1630, arXiv:hep-ex/1101.2185.

[136] S. van der Meer, "Calibration of the effective beam height in the ISR", Tech. Rep. CERN-ISR-PO-68-31., CERN, 1968.

[137] **ATLAS** Collaboration, G. Aad *et al.*, "Measurement of the Inelastic Proton-Proton Cross-Section at $\sqrt{s} = 7$ TeV with the ATLAS Detector", *Nature Commun.* **2** (2011) 463, arXiv:1104.0326 [hep-ex].

[138] **ATLAS** Collaboration, "Luminosity Public Results", https://twiki.cern.ch/twiki/bin/view/AtlasPublic/LuminosityPublicResults, 2012.

[139] **ATLAS** Collaboration, "ATLAS Run Query", http://atlas-runquery.cern.ch, 2012.

[140] A. Abdesselam, T. Barber, A. Barr, P. Bell, J. Bernabeu, *et al.*, "The Data acquisition and calibration system for the ATLAS semiconductor tracker", *JINST* **3** (2008) P01003.

[141] A. Abdesselam, P. Allport, R. Apsimon, C. Band, A. Barr, *et al.*, "The optical links of the ATLAS SemiConductor tracker", *JINST* **2** (2007) P09003.

[142] Finsar, "10Gb Oxide Isolated VCSEL Reliability Report", https://lbtwiki.cern.ch/pub/ST/VCSELs/VCSELReliabilityReport.pdf, 2007.

[143] **ATLAS** Collaboration, A. Weidberg, "VCSEL reliability in ATLAS and development of robust arrays", *JINST* **7** (2012) C01098.

[144] **ATLAS** Collaboration, G. Aad *et al.*, "Hunt for new phenomena using large jet multiplicities and missing transverse momentum with ATLAS in 4.7 fb^{-1} of $\sqrt{s} = 7$ TeV proton-proton collisions", arXiv:1206.1760 [hep-ex].

[145] **ATLAS** Collaboration, "Search for squarks and gluinos using final states with jets and missing transverse momentum with the ATLAS detector in $\sqrt{s} = 7$ TeV proton-proton collisions", Tech. Rep. ATLAS-CONF-2012-033, CERN, Mar, 2012.

[146] **CMS** Collaboration, "Search for supersymmetry in events with a single lepton and jets using a neural network", Tech. Rep. CMS-PAS-SUS-11-026, 2012.

[147] **CMS** Collaboration, "Search for supersymmetry in events with a single lepton and jets using templates", Tech. Rep. CMS-PAS-SUS-11-027, CERN, 2012.

[148] **CMS** Collaboration, "Search for new physics with single-leptons at the LHC", Tech. Rep. CMS-PAS-SUS-12-010, CERN, 2012.

[149] S. Cassel, D. Ghilencea, S. Kraml, A. Lessa, and G. Ross, "Fine-tuning implications for complementary dark matter and LHC SUSY searches", *JHEP* **1105** (2011) 120, arXiv:1101.4664 [hep-ph].

[150] W. Verkerke and D. P. Kirkby, "The RooFit toolkit for data modeling", *eConf* **C0303241** (2003) MOLT007, arXiv:physics/0306116 [physics].

[151] A. Wald, "Tests of Statistical Hypotheses Concerning Several Parameters When the Number of Observations is Large", *T.Am.Math.Soc.* **54** no. 3, (1943) pp. 426–482. http://www.jstor.org/stable/1990256.

[152] S. S. Wilks, "The Large-Sample Distribution of the Likelihood Ratio for Testing Composite Hypotheses", *Ann.Math.Stat.* **9** no. 1, (1938) pp. 60–62. http://www.jstor.org/stable/2957648.

[153] G. Cowan, K. Cranmer, E. Gross, and O. Vitells, "Asymptotic formulae for likelihood-based tests of new physics", *Eur.Phys.J.* **C71** (2011) 1554, arXiv:1007.1727 [physics.data-an].